

**Revealing key modes in photoprocesses  
using *Ab Initio* molecular dynamics**

Dissertation zur Erlangung des Doktorgrades  
an der Fakultät für Mathematik, Informatik und  
Naturwissenschaften

Fachbereich Physik der Universität Hamburg

vorgelegt von

Raison Dsouza

(Hamburg 2019)

|  |  |
|--|--|
| Gutachter der Dissertation:  | Prof. Dr. Martin Eckstein<br>Prof. Dr. R.J. Dwayne Miller                      |
| Zusammensetzung der Prüfungskommission:                                  | Prof. Dr. Daniela Pfannkuche<br>Prof. Dr. Arwen Pearson<br>Prof. Dr. Nils Huse |
| Datum der Disputation:   | 12.09.2019   |
| Vorsitzender des Fach-Promotionsausschusses                              | Prof. Dr. Michael Potthoff   |
| Leiter des Fachbereiches Physik  | Prof. Dr. Wolfgang Hansen  |
| Dekan der Fakultät für Mathematik,<br>Informatik und Naturwissenschaften | Prof. Dr. Heinrich Graener   |

*Dedicated to my parents*

The underlying physical laws necessary for the mathematical theory of a large part of physics and the whole of chemistry are thus completely known, and the difficulty is only that the exact application of these laws leads to equations much too complicated to be soluble. It therefore becomes desirable that approximate practical methods of applying quantum mechanics should be developed, which can lead to an explanation of the main features of complex atomic systems without too much computation.

---

*P.A.M Dirac*  
*Proc. R. Soc. Lond. A , Volume 123,*  
*1929*

## **Eidesstattliche Versicherung / Declaration on oath**

Hiermit versichere ich an Eides statt, die vorliegende Dissertationsschrift selbst verfasst und keine anderen als die angegebenen Hilfsmittel und Quellen benutzt zu haben.

Die eingereichte schriftliche Fassung entspricht der auf dem elektronischen Speichermedium.

Die Dissertation wurde in der vorgelegten oder einer ähnlichen Form nicht schon einmal in einem früheren Promotionsverfahren angenommen oder als ungenügend beurteilt.

Hamburg, den xx.xx.20xx

---

Unterschrift der Doktorandin / des Doktoranden



# Acknowledgements

My doctoral work has been quite a wonderful experience and many people have played a pivotal role in helping to make it a successful one.

I would like to thank my supervisor Prof. Dr. R. J. Dwayne Miller for giving me this opportunity to work in the field of Computational Chemistry and Time-Resolved spectroscopy, for his help and guidance throughout this journey. I am grateful to Prof. Dr. Martin Eckstein, for his constant support and encouragement during this time and for providing helpful tips.

An important part of this thesis originated from our collaboration and discussion with the group of Prof. Peter Weber at Brown University, whose time-resolved photo-electron spectroscopy studies into the excited-state dynamics of aliphatic amines inspired me to implement and apply the Born-Oppenheimer Molecular dynamics simulation method with ADC(2) to model the dynamics.

I also would thank a great friend and mentor, Dr. Michał Kochman (currently in Linköping, Sweden), who on many occasions shared with me his vast knowledge of ab-initio methods, and furthermore helped me in the course of the project on the photophysics of *N*-methylmorpholine.

I am also thankful to Dr. Arunangshu Debnath from the Theory department of the MPSD for his insightful comments and discussions throughout my Ph.D. Dr. Xinxin Cheng played a pivotal role in the discussion and interpretation of the experimental TRPES spectra. Dr. Zheng Li for his valuable advice concerning excited-state calculations and for his continuing work to keep my Ph.D. project on track. I'd like to thank Dr. Stuart Hayes and Dr. Heinrich Schwoerer for their valuable discussions and feedback on the Spironaphopyran experiment and electron diffraction studies.

I am indebted to the Gesellschaft für Wissenschaftliche Datenverarbeitung mbH Göttingen (GWDG) computing facility. I am also grateful to the physics department, University of Hamburg and the International Max Planck Research School (IMPRS-UFAST) for the scholarship which supported me financially throughout my Ph.D. course. I'd like to thank my friends and colleagues at the MPSD for the continual support during this Ph.D. course.

I'm grateful to Dr. Neda and Dr. Julia for easing the administrative burden at all stages of my PhD. I thank Dr. Sasha Epp and Dr. Caroline Arnold for the helpful tips in the translation of the summary into German. I thank the I.T. department, Björn and Dennis for all the technical support.

At this point, I'd like to thank some of my close friends, Kevin, Fabian, Ben, Lindsey, Simon, Caroline for their amazing company. Also my best-friends back home, Anola and Elton

for always being there.

My final acknowledgments are to my girlfriend Smrithika Subramani who has always been caring about me and encouraging me during this phase of my life.

# Summary

The Born-Oppenheimer (BO) approximation represents one of the milestones achieved in the development of molecular physics. The resulting concept of an *adiabatic* potential energy surface (PES) is fundamental to our understanding of photoprocesses and reaction dynamics. The dynamics of the nuclei on a single BO potential-energy surface is a good rationalization of dynamics occurring in chemical processes.

In many situations, the motion of nuclei on the PES of a single adiabatic state provides a realistic description of molecular dynamics. However, under certain conditions, the BO approximation breaks down, and picture of a single PES is not valid any longer. This typically happens in the course of photoinduced reactions, charge transfer processes, and molecular collision and fragmentation processes. The time-evolution of the system must then be described in terms of a number of PESs which are nonadiabatically coupled to one another. Nonadiabatic processes usually involve nuclear dynamics on at least two coupled PESs and thus cannot be rationalized within the BO approximation.

Radiationless relaxation in electronic excited states is mediated by either an internal conversion (IC) or an inter-system crossing (ISC) process. Conical Intersections (CI) are the central requirement to understand the radiationless relaxation process and have been an important tool to model IC and ISC in polyatomic systems. The understanding, as well as the optimization of CIs in molecular systems, requires computational tools that can describe the dynamical correlation and configurations interaction of the system in electronically excited states.

An established tool for elucidating mechanisms of chemical reactions that occur in the electronic excited state is *Ab Initio* molecular dynamics (AIMD). However, to describe photo processes by AIMD, an underlying electronic-structure method that can treat excited states is necessary. Time-dependent density functional theory (TDDFT) provides a *in principle* exact description of electronically excited states. Compared to wavefunction-based methods, TDDFT is computationally less demanding and is relatively straightforward and easy to use. To model radiationless relaxation in systems, a state-to-state modelling procedure is required. This is facilitated by Mixed quantum-classical (MQC) scheme in particular, surface hopping (SH) method.

In this thesis, a TDDFT based MQC method, that can account for non-adiabatic effects in photo processes is implemented. The non-adiabatic scheme is based on the fewest switches trajectory surface hopping (FSSH) method introduced by John Tully.

The method is applied to describe chemical processes, such as isomerization and intravibrational relaxation, that occur upon photoexcitation of the photochromic systems like Spironaphopyran (SNP). In the case of SNP, the results of the TDDFT-MQC method are in good

agreement with PES simulations based on the state-averaged complete active space (SA-CASSCF) method, both concerning the observed reaction mechanisms and the excited state lifetimes which are obtained from experiments conducted in-house.

Parallel to this work, we applied second order algebraic diagrammatic construction (ADC(2)) for the possible refinement of the postulated reaction mechanism and energies in the case of *N*-methylnorpholine. The ADC(2)-based MQC simulations confirm the main experimental trends, energetics and provide an accurate description of the reaction mechanism.

Additionally, a critical assessment is made for the accuracy of the *ab-initio* methods employed throughout this work and possible extension to modeling reactions in solid-state.

**Key words:** TDDFT, ADC(2), mixed quantum-classical dynamics, surface hopping, photoelectron spectra, spironaphopyran, aliphatic amines, photoisomerization, reaction modes.

# Zusammenfassung

Die Born-Oppenheimer Näherung (BOA) ist ein Meilenstein in der Entwicklung der Molekülphysik. Das daraus resultierende Konzept einer *adiabatischen* Potenzialfläche (PES) ist grundlegend für unser Verständnis von Photonprozessen und Reaktionsdynamiken. Die Dynamik der Kerne auf einer einzelnen PES ist eine gute Erklärung für die Dynamik von chemischen Prozessen.

In vielen möglichen Situationen liefert die Bewegung von Kernen auf der PES eines einzelnen adiabatischen Zustands eine realistische Beschreibung der Molekulardynamik. In einigen Fällen jedoch bricht die BOA jedoch zusammen und das Bild einer einzelnen PES ist nicht mehr anwendbar. Dies geschieht typischerweise im Verlauf von photoinduzierten Reaktionen, Ladungstransferprozessen sowie molekularen Kollisions- und Fragmentierungsprozessen. Unter diesen Bedingungen muss die zeitliche Entwicklung des Systems unter Betrachtung mehrerer PES beschrieben werden, die nichtadiabatisch miteinander gekoppelt sind. Nichtadiabatische Prozesse beinhalten normalerweise Kerndynamik auf mindestens zwei gekoppelten PES und können daher nicht innerhalb der BOA beschrieben werden. Typische Phänomene, die mit einer Verletzung der Born-Oppenheimer-Näherung einhergehen, sind die strahlungslose Relaxation angeregter elektronischer Zustände, Ladungstransferprozesse, photoinduzierter molekularer Zerfall und Isomerisierungsprozesse mehratomiger Moleküle.

Die strahlungslose Relaxation in elektronisch angeregten Zuständen entweder über einen internen Umwandlungsprozess (IC) oder einen Inter-System-Crossing-Prozess (ISC) geschieht. Konische Durchschneidungen (CI) sind die zentrale Voraussetzung für das Verständnis des strahlungslosen Relaxationsprozesses und ein wichtiges Instrument zur Modellierung von IC und ISC in mehratomigen Systemen. Das Verständnis sowie die Optimierung von CIs in molekularen Systemen erfordern Rechenwerkzeuge, die die dynamische Korrelation und Konfigurationswechselwirkung des Systems in elektronisch angeregten Zuständen beschreiben können.

Ein etabliertes Werkzeug zur Aufklärung der Mechanismen chemischer Reaktionen, die in elektronisch angeregten Zuständen ablaufen, ist die *Ab Initio* Moleküldynamik (AIMD). Zur Beschreibung von Photonprozessen durch AIMD ist jedoch eine zugrunde liegende elektronische Strukturmethode erforderlich, mit der angeregte Zustände behandelt werden können. Die zeitabhängige Dichtefunktionaltheorie (TDDFT) liefert eine *im Prinzip* genaue Beschreibung elektronisch angeregter Zustände. Im Vergleich zu Wellenfunktionsmethoden ist TDDFT weniger rechenintensiv und benutzerfreundlich. Um die strahlungslose Relaxation in Systemen modellieren zu können, ist ein Zustands-Modellierungsverfahren erforderlich, welches durch das *Mixed quantum-classical* (MQC)-schema, insbesondere die *Surface Hopping*-Methode, gegeben ist.

In dieser Arbeit wird eine TDDFT-basierte MQC-Methode implementiert, die nicht-adiabatische

Effekte in Photoprozessen berücksichtigen kann. Das nicht-adiabatische Schema basiert auf der von John Tully eingeführten minimalen FSSH-Methode (*Trajectory Surface Hopping*).

Die Methode wird angewendet, um chemische Prozesse wie Isomerisierung und IC zu beschreiben, die bei Photoanregung von photochromen Systemen wie Spiroanthopyran (SNP) auftreten. Im Falle von SNP stimmen die Ergebnisse der TDDFT-MQC-Methode gut mit PES-Simulationen überein, die auf der Methode des zustandsgemittelten vollständigen aktiven Raums (SA-CASSCF) basieren. Dies gilt sowohl hinsichtlich der beobachteten Reaktionsmechanismen als auch der angeregten Zustandslebensdauern, wie kürzlich selbst durchgeführte Experimente zeigen.

Durch die Verwendung von MQC innerhalb von Second Order Algebraic Diagrammatic Construction (ADC(2)) wird die Verfeinerung des postulierten Reaktionsmechanismus und der Energiezustände ermöglicht. Im Falle von *N*-methylmorpholin bestätigen die ADC(2)-Simulationen die generellen experimentellen Trends, die Energielevel sowie eine genaue Beschreibung des Reaktionsmechanismus.

Zusätzlich wird eine kritische Bewertung der Genauigkeit der in dieser Arbeit verwendeten *ab-initio*-methoden und einer möglichen Ausweitung auf Modellierung von Reaktionen in Festkörpern vorgenommen.

**Schlüsselwörter:** TDDFT, ADC(2), gemischte quantenklassische Dynamik, nichtadiabatische Dynamik, Photoelektronenspektren, Spiroanthopyran, aliphatische Amine, Photoisomerisierung, Reaktionsmodi.

## PUBLICATIONS INCLUDED IN THIS THESIS

- **2018** – *Oscillatory Photoelectron Signal of N-Methylmorpholine as a Test Case for the Algebraic-Diagrammatic Construction Method of Second Order*.  
**Raison Dsouza**, Xinxin Cheng, Zheng Li, R. J. Dwayne Miller and Michał Andrzej Kochman  
[The Journal of Physical Chemistry A 122.50 : 9688-9700.](#)
- **2019** – *Ultrafast ring-opening and solvent dependent product relaxation of photochromic spironaphthopyran*.  
Simon F. Bittmann, **Raison Dsouza**, Khalid M. Siddiqui, Stuart A. Hayes, Andreas Rossos, Gastón Corthey, Michał Kochman, Valentyn I. Prokhorenko, R. Scott Murphy, Heinrich Schworer and R. J. Dwayne Miller  
[Physical Chemistry Chemical Physics, 2019, DOI: 10.1039/C9CP02950H.](#)

## REST OF THE PUBLICATIONS

- **2019** – *Half a minute of enzyme dynamics captured by time-resolved crystallography*.  
Pedram Mehrabi, Eike C. Schulz, **Raison Dsouza**, Henrike M. Mller-Werkmeister, Friedjof Tellkamp, R. J. Dwayne Miller and Emil F. Pai  
[\(In print\) Science.](#)
- **2019** – *Photo-induced isomerization of Spironaphthopyran molecular crystals using hybrid QM/QM*  
**Raison Dsouza**, Simon F. Bittmann, Khalid Siddiqui, Stuart A. Hayes, Michał Kochman, Valentyn I. Prokhorenko and R. J. Dwayne Miller  
[In preparation](#)
- **2019** – *Ultrafast charge localization and relaxation mechanism of photoexcited N,N'-dimethylpiperazine controlled by the topography of potential energy surface*  
Xinxin Cheng, **Raison Dsouza**, Zheng Li, R. J. Dwayne Miller, and Michał Andrzej Kochman  
[In preparation](#)



# List of Abbreviations

- **BO** : Born-Oppenheimer
- **FSSH** : Fewest switches surface hopping
- **ADC** : Algebraic diagrammatic construction
- **DFT** : Density functional theory
- **TDDFT** : Time-dependent density functional theory
- **TDA** : Tamn-Damncoff approximation
- **MP2** : Second order Møller-Plesset perturbation theory
- **CCSD** : Coupled-cluster singles-and-doubles method
- **EOM-CCSD** : Equation of motion coupled-cluster singles-and-doubles method
- **CC2** : Approximate coupled-cluster singles-and-doubles method
- **CASSCF** : Complete active space self-consistent field
- **CASPT2** : Complete active space perturbation theory of second order
- **TRPES** : Time-resolved photoelectron spectroscopy
- **RFS** : Rydberg fingerprint spectroscopy
- **BE** : Binding energy
- **TA** : Transient absorption
- **CI** : Conical intersections
- **MQC** : Mixed quantum-classical
- **PES** : Potential energy surface
- **MD** : Molecular dynamics
- **SNP** : Spiroanthopyran
- **BIPS** : Benzo-indolino-spiropyran



# Contents

|          |   |           |
|----------|---|-----------|
| <b>1</b> | <b>Thematic outline</b>   | <b>19</b> |
| 1.1      | Time-Resolved Spectroscopic Techniques . . . . .                  | 20        |
| 1.2      | Born-Oppenheimer approximation . . . . .                          | 24        |
| 1.3      | Mixed quantum-classical dynamics methodology . . . . .            | 26        |
| 1.4      | Surface hopping . . . . .   | 27        |
| 1.4.1    | Derivation . . . . .  | 28        |
| 1.5      | Outline of Simulation Scheme . . . . .                            | 32        |
| 1.6      | Excited-State Electronic Structure Methods . . . . .              | 34        |
| 1.6.1    | Time-dependent density functional theory . . . . .                | 34        |
| 1.6.2    | Second-order algebraic diagrammatic construction method . . . . . | 36        |
| <b>2</b> | <b>Publications</b>   | <b>39</b> |
| 2.1      | Summary : Article 1 . . . . .                                     | 39        |
| 2.2      | Summary : Article 2 . . . . .                                     | 51        |
| <b>3</b> | <b>Outlook</b>  | <b>67</b> |
|          | <b>Bibliography</b>   | <b>69</b> |



# Chapter 1

## Thematic outline

In this chapter, a summary of the research areas covered in this dissertation will be elaborated. An introduction to time-resolved techniques will be outlined along with the experiments to which the simulation was addressed. Then, a treatise into the Born Oppenheimer approximation is provided and its subtleties enlisted. The ‘Mixed quantum classical dynamics’ methodology will be introduced and its variant ‘Surface hopping’ will be discussed and derived. A flowchart into the implementation is also provided. Finally, the relevant electronic structure techniques used in this thesis work will be summarized.

## 1.1 Time-Resolved Spectroscopic Techniques

In this section, a summary of the methods of time-resolved laser spectroscopy and their significance is discussed.

Time-resolved spectroscopy provides a tool to monitor the time evolution of molecular processes like emission, absorption or scattering that are used to obtain information about the dynamics of physical systems. These methods provide kinetics of reactions occurring on relevant time scales of physical, chemical and biological processes. The actual atomic motions involved in chemical reactions were found to be extremely fast and presumed to occur on the picosecond and femtosecond time scale. To study these relevant fast motions, one needed a tool which provides a proper time resolution. Ultrafast pulsed lasers have made direct exploration of this temporal realm a reality [1].

Molecular motions that are relevant (*key modes*) in chemical reactions dynamics of the chemical bond at the atomic level such as the breaking and formation of bonds, ultrafast transformations leading to transition states, the redistribution of energy over different degrees of freedom can now be monitored in real-time. Time-resolved laser spectroscopy methods provide information about the dynamics of various processes, such as:

- dynamics of reaction coordinates, e.g., isomerization; excited-state proton/electron transfer, etc.
- rotational/orientational relaxation;
- vibrational dephasing ( $T_2$ )
- vibrational relaxation ( $T_1$ )

Some of the common configurations of time-resolved spectroscopy used nowadays are :

- fluorescence decay
- pump-probe methods
- non-linear stimulated Raman scattering based methods
- photon echoes.

### Pump-probe Spectroscopy

The concept of the pump-probe method is presented in Fig.1.1. The beam-splitter divides the pulsed laser beam into two beams : the pump and the probe beam. These beams travel along different optical path lengths before they are joined together again. The delay of the probe beam with respect to the pump beam is  $\Delta t = \frac{\Delta x}{c}$ , where  $\Delta x$  is the optical path difference (Fig. 1.1). The signal in the detector now depends only on the delay of the probe beam to the pump beam,  $\Delta t$ . Recording this signal for the different time delays, we are now able to monitor the dynamics of the relevant phenomena. The time resolution of this method does not depend on the time response of the detector but rather on the pulse duration.

In the configuration presented in Fig.1.1, the pump beam and the probe beam have the

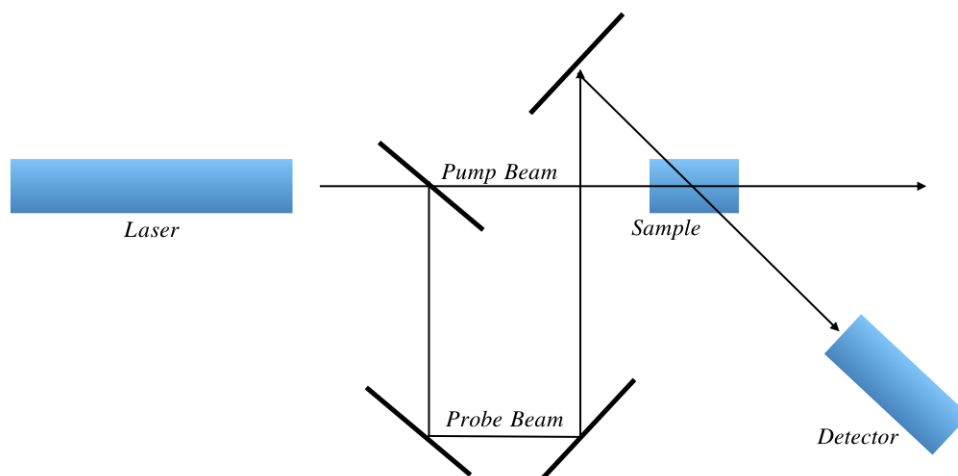


Figure 1.1: Scheme illustrating the principle of pump-probe method

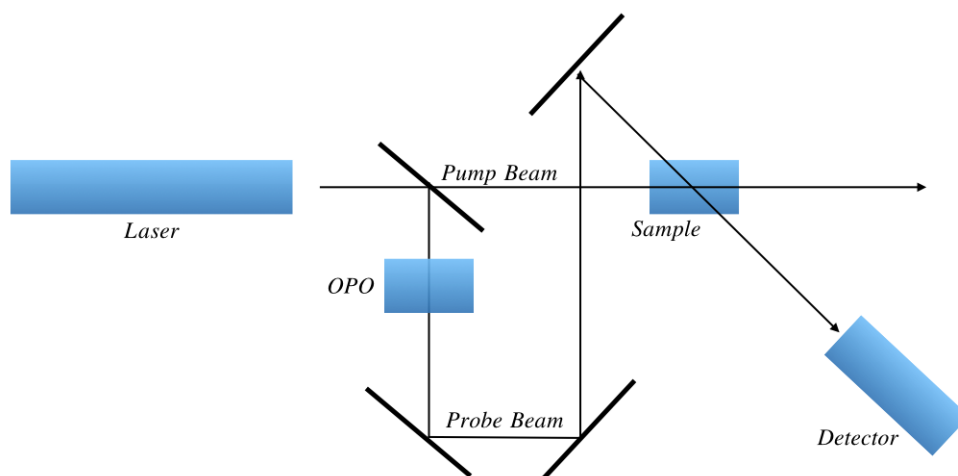


Figure 1.2: Scheme illustrating the principle of the pump-probe method when the pump and the probe beams have different frequencies

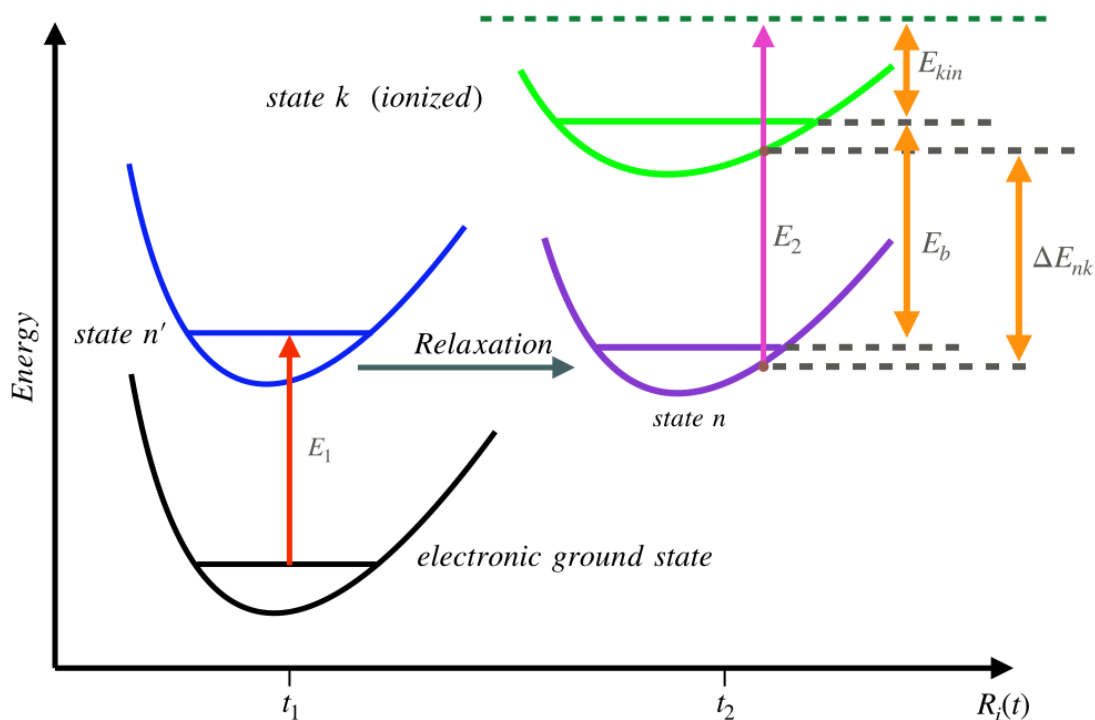


Figure 1.3: Schematic illustration of the steps involved in obtaining photo-electron spectra . At time  $t = t_1$ , the pump pulse with photon energy  $E_1$  excites the system to state  $n'$ , following which it is allowed to relax until  $t = t_2$  . By  $t = t_2$  , the system exists in electronic state  $n$  , which may in general be a different adiabatic state than  $n'$  . At  $t = t_2$  , the system is subjected to the probe pulse of photon energy  $E_2$  , which detaches a photoelectron with kinetic energy  $E_{kin}$  , leaving behind a ionized species in electronic state  $k$  . The approximation that the probe pulse does not alter the kinetic energy of the nuclei leads to the result that the electronic binding energy  $E_b = E_2 - E_{kin}$  is equal to the vertical energy difference between states  $k$  and  $n$

same wavelength, which considerably limits the number of possible applications in which this method can be used. In most experimental configurations, the setup is manipulated such that these beams have different frequencies (Fig.1.2). However, one can also tune the frequency of the pump or/and the probe beams over a broad spectral range by employing tunable light sources, such as parametric generators (OPG), parametric oscillators (OPO), parametric amplifiers (OPA) or using white continuum sources (WC) emitting radiation in a broad spectral range. The origin of the WC generation is well described elsewhere [2]. The WC process is mainly governed by SPM (self-phase modulation) and stimulated Raman emission. The most popular substances used to generate WC are water, deuterium-enriched water, quartz glass, and sapphire.

In the studies reported in this thesis, the experiments involved two approaches to pump-probe setup. In the first transient absorption setup, the system is excited with the pump pulse of high intensity and frequency such that some fraction of molecules will be promoted from the lower to the upper state. Consider a two-level system with energies  $E_1$  and  $E_2$ . The second pulse (probe) delayed with respect to the pump pulse by  $\Delta t$ , monitors

the transient absorption  $A(E_1 \rightarrow E_2)$  that is smaller than the absorption  $A_0$  recorded for the same probing pulse without employing the pumping pulse. When the time delay,  $\Delta t$ , of the probe beam increases and exceeds the lifetime of the excited level  $T_1$  ( $\Delta t > T_1$ ), one observes the return of the excited molecules to the lower level and recovery of the initial absorption value observed before the action of the pump pulse. The changes in the absorption spectrum may involve the spectral shifts and/or the optical density changes for a given wavelength. Analysis of the spectral changes provides information about new species or transitions created by the pump excitation, while the temporal analysis for a given wavelength provides information about the population dynamics.

In the study of photo-isomerization of spironaphopyran (SNP), a pump pulse in the ultra-violet range was used to initiate the dynamics and a WC source was used to probe the formulation of the product state merocyanine (MC). Since the reactant SNP has no absorption coefficient in the visible range, this configuration of pump-probe is only sensitive to monitor the dynamics of MC formation.

Time-resolved photoelectron spectroscopy (TRPES) is a pump-probe technique in which the pump pulse prepares the system and, after a time delay, the probe pulse ionizes it. Information on the time-evolution of the system is extracted from the analysis of the photoelectron current, resolved with respect to time and the kinetic energy of the photoelectrons. The second of the two studies that provide the basis for this thesis revolved around the TRPES signature of the aliphatic amine *N*-methylmorpholine (NMM). The TRPES spectrum of NMM was recorded experimentally by Zhang et al [3]. Its photoelectron signal arises from ionization from the Rydberg states. This particular variant of TRPES is often referred to as time-resolved Rydberg fingerprint spectroscopy (TR-RFS). It takes advantage of the fact that a Rydberg electrons' binding energy (BE) is extremely sensitive to both the underlying structure and the charge distribution of the molecular ion core. Because the Rydberg orbital is diffused (electron is sufficiently far from the core), the electronic and nuclear configuration of the molecular ion core are unaffected by it. Therefore, the PES of the Rydberg state is almost identical to that of the ion state. This makes RFS insensitive to the vibrational excitation and the photoelectron spectra free of vibrational congestion [4].

TR-RFS particularly combines the pump-probe methodology with RFS. In a typical pump-probe experiment using RFS, the molecule is resonantly excited to a Rydberg state with an ultra-short pump pulse. After a time delay, the time-evolution of the Rydberg-excited molecule are then ionized by the probe pulse. The structural dynamics is then followed by measuring the ejected photoelectrons as a function of time delay. The photoelectrons are collected and analyzed by a time-of-flight (TOF) spectrometer. The electron flight time is converted to kinetic energy (KE). Since the wavelength of the probe pulse is known, the BE of the photoelectron can be obtained by subtracting the KE from the total energy of the probe photon. A schematic energy diagram of the processes involved in calculating the photoelectron spectrum corresponding to a TR-RFS measurement is shown in Fig 1.3. Because the ejection of a photoelectron is fast compared to nuclear motions, the photoelectron spectra reflect the molecular structure at the time the electron is ejected.

## 1.2 Born-Oppenheimer approximation

This section aims to introduce the basic concepts of theoretical suppositions and approximations. When required one will find illustrations with examples from recent research and critical points mentioned which indicate current trends.

The Born-Oppenheimer (BO) approximation and the underlying ideas have been a milestone in the theory of molecules. The large mass of a nucleus compared to that of an electron permits an approximate separation of the electronic and nuclear motion. Molecules are many-body systems and this separation greatly simplifies their quantum mechanical treatment. Also, it allows us to visualize the dynamics of molecules and provides the essential link between quantum mechanics and chemistry.

In diatomic molecules, there is only a single degree of freedom (DoF) and the BO approximation provides an accurate description of the PES and dynamics. In polyatomic molecules, however, the electronic ground state is typically well separated from other electronic states energetically, and this allows for *a priori* application of the BO approximation. Historically, the picture has emerged that this approximation is generally accurate except for exotic cases. In the last few decades, however, there have been considerable strides in the development of experimental and theoretical techniques and a growing number of polyatomic systems in their excited electronic states have been investigated. A particularly impressive failure in BO approximation is encountered in situations where the so-called conical intersection (CI) of the electronic energies exists. For such an intersection to appear, at least two nuclear coordinates are necessary. Since polyatomic have dense electronic states and many nuclear degrees of freedom, conical intersections of the electronic energies are generic features and their absence is rather unusual [5].

The remarkable advances achieved in femtosecond laser technology and time-resolved spectroscopy have revealed that the radiationless decay of excited electronic states may take place much faster than previously anticipated. Hence, it is nowadays well-known that in large organic molecules internal conversion from upper to lower excited states occurs on a subpicosecond scale. The initial versions of the theory of internal conversion seemed to work fine for the weak coupling cases in which this process was relatively slow and competed with fluorescence or with intersystem crossing to a triplet state. However, this theory did not cast light on the nature of the ultrafast process. Although early works [6–9] indicated that there seemed to be no doubt that ultrafast internal conversion proceeded by passage through CIs, there was no attempt to provide any mechanistic insight into the nature of molecular configurations involved. Finally, in the reformulation of the Woodward-Hoffman rules by Zimmerman [10], the first clue in this direction was provided. It pointed out that in the Huckel approximation, the ground and excited potential energy surfaces touch at a point located on a symmetry-forbidden path of a pericyclic reaction, explaining the opposite nature of the rules for thermal and photochemical reactions of this type. Experiments conducted by Michl led him to conclude that both are important: with a barrier along the way, the pericyclic minimum will not be reached even if it is present, and the product will not form unless extra energy is provided (e.g. by a second photon) to pass above the barrier [11]. Later on, he summarized the state of understanding of the physical nature of processes involved in organic photochemistry at the time and the qualitative MO arguments that can be used for the rationalization of specific

reaction paths [12].

In recent years, Robb, Bernardi and Olivucci [13] have been particularly prolific in identifying conical intersections along the paths of a vast number of organic reactions and refining the detailed understanding of organic reaction paths. It is now increasingly recognized that CIs play a key mechanistic role in molecular spectroscopy and chemical reaction dynamics.

One requires procedures for the calculation of molecular dynamics on excited-state surfaces of polyatomic organic molecules, which needs a knowledge of nonadiabatic coupling matrix elements (in regions of CI). Without this information, we cannot even tell whether all the computational effort that has gone into identifying the lowest energy points in the conical intersection subspace is meaningful.

Although much progress has been made in recent years with electronic-structure theory and the efficient interpolation of multidimensional potential functions, the selection of the relevant coordinates and the construction of a diabatic representation for polyatomic molecules represent major bottlenecks in the theoretical treatment of the excited state dynamics. To avoid these bottlenecks, one can try another method which evaluates the potentials and the derivative couplings at every point. Several attempts combining this “on-the-fly” approach with classical surface-hopping trajectory calculations or similar trajectory-based methods for conical intersections have been reported in the recent literature [14–16].

“Mixed quantum-classical dynamics” methods are one of the few promising strategies to explore excited-state PESs of the multidimensional system in an unbiased manner. Serious obstacles encountered in this type of approach are the immense cost of these calculations if reasonably accurate *ab initio* methods are to be employed, the phase problem of electronic wave functions in the presence of intersections, and the development of quantitatively accurate surface-hopping prescriptions. Nevertheless, the development of full-dimensional on-the-fly methods for the dynamics at conical intersections will continue to be an active area of research in the future.

### 1.3 Mixed quantum-classical dynamics methodology

In this section, we now begin to consider the characterization of chemically reactive dynamics.

During the last few decades, the mixed quantum-classical (MQC) formulation has been used for the description of quantum-mechanical processes. As the numerical effort for quantum-mechanical basis-set calculation increases exponentially with the number of degrees of freedom (DoF), straightforward quantum computation is restricted to only a few vibrational DoF for a polyatomic system. Classical mechanics, on the other hand, scales linearly with the number of DoF, but it only represents a reasonable description of microscopic dynamics. Hence the strategy of MQC models is to combine the advantages of both methods, thus describing the dynamics of the “classical DoF” (e.g. the motion of heavy nuclei) in a classical framework and invoke quantum mechanics only for the description of the dynamics of the “quantum DoF” (e.g. the motion of electrons and protons). In this thesis, the application of this principle (using MQC methods) to describe non-Born-Oppenheimer dynamics mediated by a conical intersection is exemplified.

The MQC description can be derived by starting with a quantum-mechanically exact formulation for the complete system and performing a partial classical limit for the heavy-particle DoF. This procedure is not unique, however, since it depends on the particular quantum formulation chosen as well as on the specific way to achieve the classical limit. In the mean-field trajectory method, the wave-function formulation of quantum mechanics is adopted and the Ehrenfest classical limit is performed for the heavy-particle DoF. Alternatively, one may consider the Liouville equation of the density operator and perform a classical limit within the Wigner representation for the heavy-particle DoF. This leads to the quantum-classical Liouville description which has recently received considerable attention [17–19]. Also, the hydrodynamic or Bohmian formulation of quantum mechanics has been used recently as a starting point for a MQC description [20, 21] It should be made clear at the outset that the MQC formulations differ greatly, depending on whether the problem is approached via the wave-function, density-operator or hydrodynamic formulation of quantum mechanics.

Since the validity of an approximate description depends to a large extent on the specific physical application under consideration, one may ask whether a MQC strategy appears promising to describe the dynamics at conical intersections. The electronic and vibrational relaxation dynamics associated with conical intersections exhibit several characteristic features, which represent a hard challenge for an approximate theoretical description:

- the dynamics are caused by strong intramolecular interactions that cannot be accounted for in a perturbative manner
- due to the large anharmonicity of the adiabatic potential-energy surfaces, the vibrational motion is highly correlated, thus hampering the application of simple self-consistent-field schemes.

Within the limits of the underlying classical approximation, these requirements are fulfilled by an MQC formulation which is a nonperturbative description and also fully includes the correlation between the individual DoF. An MQC description appears to be

one of the few approximations that may be expected to work. Furthermore, it should be stressed that a classical (and therefore local) description is readily combined with an “on-the-fly” *ab initio* evaluation of the potential-energy [16, 22, 23]. Nonadiabatic *ab initio* molecular dynamics methods are one of the few promising strategies to explore the excited-state potential-energy surfaces of the multidimensional system in an unbiased manner.

We review the MQC methods that have been applied to the dynamics at conical intersections. Here the surface-hopping method has been the most popular approach, [24–26], in particular in combination with an on-the-fly *ab initio* evaluation of the potential-energy [22, 27]. Various self-consistent-field methods have been employed to describe internal-conversion dynamics associated with a conical intersection, including the mean-field trajectory method, the classical electron analog model, and the quasi classical mapping formulation [28, 29]. Since there is no sampling problem due to oscillating phases, all these methods are readily implemented and typically converge for a moderate number of trajectories.

## 1.4 Surface hopping

In this section, we focus on the *semiclassical* (i.e., one part of the system (the electrons) is treated quantum-mechanically, while the other (the nuclei) is treated essentially classically) model of Surface hopping (SH) methodology, which has turned out to be the most popular approach to describe non-adiabatic dynamics at conical intersections.

The semiclassical SH model employs the simple picture in which a molecular system always evolves on a *single adiabatic* potential-energy surface (PES). When the trajectory reaches an intersection point of the PESs  $\{n\}$ , the transition probability  $p_{n \rightarrow n'}$  to the other PES is calculated according to a defined hopping criterion and, depending on the comparison of  $p_{n \rightarrow n'}$  with a random number, the trajectory “hops” to the other adiabatic surface. To conserve the energy of the classical system during an electronic transition, the momenta of the nuclei have to be adjusted after every hop. The SH simulations are performed in the adiabatic representation, because

- the picture of instantaneous hops only appears plausible for highly localized interactions between the PESs such as the nonadiabatic kinetic-energy couplings
- a single adiabatic PES is expected to represent the coupled-surfaces problem better than a single diabatic one.
- adiabatic electronic states are readily obtained directly from electronic structure calculations. On the other hand, the diabatic states are not defined unambiguously, and must be obtained from the adiabatic states via an adiabatic-to-diabatic transformation. This procedure introduces additional complexity into the simulation.

The key problem of the SH approach is to establish a dynamically consistent hopping criterion and momentum adjustment because the hopping procedure accounts for the coupling of electronic and nuclear degrees of freedom. Here the most popular formulation is the *fewest switches surface hopping* algorithm proposed by Tully [30]. A detailed description can be found in many papers (see, e.g. Refs. [30], [31], [32] and [15]).

### 1.4.1 Derivation

The molecular Hamiltonian (non-relativistic) of  $N$  atoms with coordinates  $\{R\}$  and  $n$  electrons with coordinates  $\{r\}$  is given by

$$H_{mol}(r, R) = T(R) + T(r) + V(R) + V(r) + V(r, R) \quad (1.1)$$

where the individuals operators are given as  
kinetic energy of the nuclei

$$T(R) = -\frac{\hbar^2}{2} \sum_{J=1}^N \frac{\nabla_J^2}{M_J} \quad (1.2)$$

kinetic energy of the electrons

$$T(r) = -\frac{\hbar^2}{2m_e} \sum_{j=1}^n \nabla_j^2 \quad (1.3)$$

nuclei-nuclei repulsion

$$V(R) = \frac{e^2}{4\pi\epsilon_0} \sum_{J=1}^{N-1} \sum_{I>J}^N \frac{Z_I Z_J}{|R_J - R_I|} \quad (1.4)$$

electron-nuclear interaction

$$V(r, R) = -\frac{e^2}{4\pi\epsilon_0} \sum_{J=1}^N \sum_{j=1}^n \frac{Z_J}{|r_j - R_J|} \quad (1.5)$$

and electron-electron repulsion

$$V(r) = \frac{e^2}{4\pi\epsilon_0} \sum_{j=1}^{n-1} \sum_{i>j}^n \frac{1}{|r_j - r_i|} \quad (1.6)$$

where  $m_e$  is the mass of the electron,  $M_J$  and  $Z_J$  are the mass and charge of the  $J^{\text{th}}$  nuclei,  $\epsilon_0$  is the permittivity of vacuum,  $\hbar$  is Planck's constant.

The time-evolution of the molecular wavefunction  $\Psi(r, R; t)$  is given by the solution of the Time-dependent Schrödinger equation

$$H_{mol}\Psi(r, R; t) = i\hbar \frac{\partial}{\partial t} \Psi(r, R; t) \quad (1.7)$$

We now perform what is known as *clamped - nuclei* approximation (i.e., setting  $T(R) = 0$ ). With this we obtain the electronic Hamiltonian as

$$H_{el} = T(r) + V(R) + V(r, R) + v(r) \quad (1.8)$$

Let us now suppose we could solve this Hamiltonian to obtain eigenvalues and eigenfunctions.

$$H_{el}\psi_j(r; R) = E_j(R)\psi_j(r; R) \quad (1.9)$$

The spectrum of  $H_{el}$  is assumed to be discrete and the eigenfunctions orthonormalized :

$$\int_{-\infty}^{\infty} \psi_i^*(r, R) \psi_j(r, R) dr = \delta_{ij} \quad (1.10)$$

Now we make an ansatz that the total molecular wavefunction  $\Psi(r, R; t)$  can be expanded in the complete set of eigenfunctions of  $H_{el}$  as

$$\Psi(r, R; t) = \sum_j \psi_j(r, R) \chi_j(R, t) \quad (1.11)$$

where  $\chi(R, t)$  is the nuclear wavefunction. Inserting this ansatz into Equation 1.7 and multiplying from the left by  $\psi_i^*(r, R)$  and integrating over the electronic coordinates  $\{r_i\}$  one obtains

$$\left[ T(R) + E_i(R) \right] \chi_i(R, t) + \sum_j C_{ij} \chi_j(R, t) = i\hbar \frac{\partial}{\partial t} \chi_i(R, t) \quad (1.12)$$

where  $C_{ij}$  is called the electron-nuclear coupling operator which has the explicit form

$$C_{ij} = \langle \psi_i | T(R) | \psi_j \rangle - \sum_J \frac{\hbar^2}{M_J} \langle \psi_i | \nabla_J | \psi_j \rangle \nabla_J \quad (1.13)$$

We are now in a position to make the *adiabatic approximation* (i.e., setting  $C_{ij} = 0$ ) we obtain

$$\left[ T(R) + E_i(R) \right] \chi_i(R, t) = i\hbar \frac{\partial}{\partial t} \chi_i(R, t) \quad (1.14)$$

The coupled differential equations in Eq. 1.12 are now uncoupled and we obtain an equation of motion for the nuclei which evolve on a single PES  $i$ . That is, the nuclear evolution doesn't change the quantum state of the electron cloud. This means that the total wavefunction has only a single term

$$\Psi(r, R; t) \approx \psi_i(r, R) \chi_i(R, t) \quad (1.15)$$

This equation can be applied to a variety of phenomena in chemistry. Albeit, there are many important phenomena like charge transfer and photoisomerization which involve the inseparability of electronic and nuclear motion. We now proceed to formulate the semi-classical approach of Mixed-quantum classical dynamics.

The assumption here is that the nuclear evolution follows some classical path (called trajectory)  $R(t)$  while the electronic degrees of freedom are handled quantum mechanically. That is, the nuclei follow some classical equation of motion (Eg: Newton's) and the electronic motion is characterized by a time-dependent wavefunction  $\Phi(r; t)$  which satisfies the electronic Schrödinger equation

$$H_{el}(R, R(t)) \Phi(r; t) = i\hbar \frac{\partial}{\partial t} \Phi(r; t) \quad (1.16)$$

This wavefunction can be expressed by a linear-combination of solutions  $\psi(r; t)$  of adiabatic Schrödinger equation Eq 1.9

$$\Phi(r; t) = \sum_k a_k(t) \phi_k(r, R) e^{-\frac{i}{\hbar} \int E_k(R) dt} \quad (1.17)$$

In order to obtain an expression for the expansion coefficients  $a_k$  we multiply Eq 1.17 by the left by  $\phi_j^*(r, R)$  to obtain a set of coupled differential equations

$$\dot{a}_k = - \sum_j C_{kj} e^{-\frac{i}{\hbar} \int (E_j - E_k) dt} \quad (1.18)$$

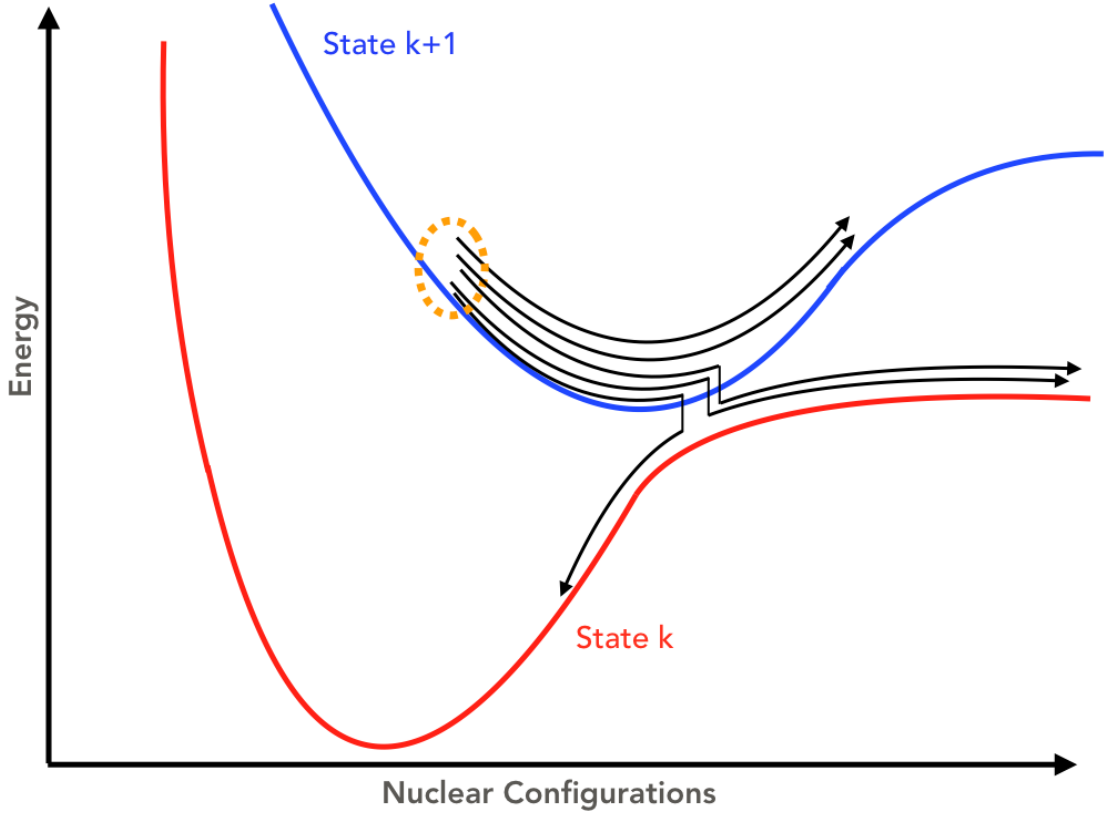


Figure 1.4: Illustrative diagram of surface hopping scheme

where

$$C_{kj} = \langle \phi_k | \frac{\partial}{\partial t} | \phi_j \rangle \quad (1.19)$$

are the nonadiabatic coupling matrix elements between the quantum states  $j$  and  $k$  of the electron cloud. In order to make the connection to Mixed-quantum classical technique we will derive the surface hopping technique which involves the idea of an *ensemble* of nuclear trajectories  $\{R(t)\}$  (See Fig 1.4). We will discuss here the formulation by Tully [15], called the “fewest-switches” algorithm. Basically, this procedure ensures the minimum number of state switches in an area of nonadiabatic coupling while also ensuring the correct ensemble averaged state populations at all times.

Out of the total  $M$  trajectories (nuclear configurations), consider  $M_s$  will be in state  $k$  and time  $t$ ,

$$M_k(t) = \rho_{kk}(t)M \quad (1.20)$$

here we use the density matrix notation for it's simplicity in connecting to ideas of population and coherence.

$$\rho_{kk}(t) = a_k^*(t)a_k(t) \quad (1.21)$$

At some later point in time  $t'$ , the new occupation would be

$$M_k(t') = \rho_{kk}(t')M \quad (1.22)$$

where  $t' = t + \delta t$ . Now suppose that  $M_k(t') < M_k(t)$  or  $\delta M = M_k(t) - M_k(t') > 0$ , then the minimum number of state jumps  $k \rightarrow k'$  required from  $M_k(t)$  to  $M_k(t')$  is  $\delta M$ . The

probability  $P_k(t, \delta t)$  for a transition out of state  $k$  to other states  $\{k\}$  during the interval  $t, t + \delta t$  is given by

$$P_k(t, \delta t) = \frac{\delta M}{M} = \frac{\rho_{kk}(t) - \rho_{kk}(t')}{\rho_{kk}} \approx -\frac{\dot{\rho}_{kk} \delta t}{\rho_{kk}} \quad (1.23)$$

where

$$\dot{\rho}_{kk} \approx \frac{\rho_{kk}(t') - \rho_{kk}(t)}{\delta t} \quad (1.24)$$

The derivative of the *population* term  $\rho_{kk}$  is given as

$$\frac{d}{dt}(a_k^* a_k) = \dot{a}_k^* a_k + a_k^* \dot{a}_k = (\dot{a}_k^* a_k)^* + a_k^* \dot{a}_k = 2\Re\epsilon(a_k^* \dot{a}_k) \quad (1.25)$$

Inserting Equation 1.18 into the Equation 1.25, we get

$$\dot{\rho}_{kk} = -2\Re\epsilon\left(\sum_l \rho_{kl} C_{kl} e^{-\frac{i}{\hbar} \int (E_l - E_k) dt}\right) \quad (1.26)$$

Substituting 1.26 into 1.23 we get

$$P_{k'}(t, \delta t) = \frac{2\Re\epsilon\left(\sum_l \rho_{kl} C_{kl} e^{-\frac{i}{\hbar} \int (E_l - E_k) dt}\right) \delta t}{\rho_{kk}} \quad (1.27)$$

Since  $P_k$  must be the sum over all the probabilities  $P_{kk'}$ , for a state jump from  $k$  to  $k'$  we get

$$P_{k'}(t, \delta t) = \sum_k P_{kk'}(t, \delta t) \quad (1.28)$$

it also follows from Equation 1.27 that

$$P_{kk'}(t, \delta t) = \frac{2\Re\epsilon\left(\sum_l \rho_{kk'} C_{kk'} e^{-\frac{i}{\hbar} \int (E_{k'} - E_k) dt}\right) \delta t}{\rho_{kk'}} \quad (1.29)$$

A state transition  $k \rightarrow k'$  is only allowed if

$$P_k^{(k')} < \xi < P_k^{(k'+1)} \quad (1.30)$$

where  $\xi$  ( $0 \leq \xi \leq 1$ ) and  $P_k^{(k')}$  is the sum of the transition probabilities for the first  $k'$  states

$$P_k^{(k')} = \sum_k^{k'+1} P_{k k'+1} \quad (1.31)$$

## 1.5 Outline of Simulation Scheme

- The starting nuclear configuration was optimized at second order Møller-Plesset perturbation theory (MP2) and density-functional theory. The optimized configurations are compared to check for any deviations in structure parameters (equilibrium bond lengths, dihedrals, etc.).
- Vertical excitation energies (corresponding to Franck Condon excitation) are computed using TDDFT/ADC(2) with a fairly large basis (if experimental data is available, these energies are compared).
- A relaxed potential energy scan along the *reaction coordinate* is computed. Whenever available, a method that includes electron correlation/dynamical configurations interaction at a higher level of theory is used to recalculate and compare.
- The corresponding hessian calculated for the optimized configuration is used to obtain a phase-space distribution (i.e., sets of atomic coordinates and velocities) are computed using the Wigner formula for quantum harmonic oscillator.
- For each set of phase space points, a single-point excitation energy calculation is performed. All these values are used to characterize the absorption spectra using the nuclear ensemble method.
- Using the calculated absorption spectra, an energy bandwidth criteria is used to pick phase-space points as initial phase-space distribution for dynamics simulations. The criteria here are the energy and corresponding oscillator strength of the transition.
- The selected phase-space points are assigned to have population at the state which is sampled and the electronic plus nuclear degrees of freedom are propagated.
- A hopping-criteria is checked at every time-step to simulate the internal conversion process.
- At every few steps of the simulation, the observable quantities are written as output files. The electronic average is performed to obtain the electronic populations.

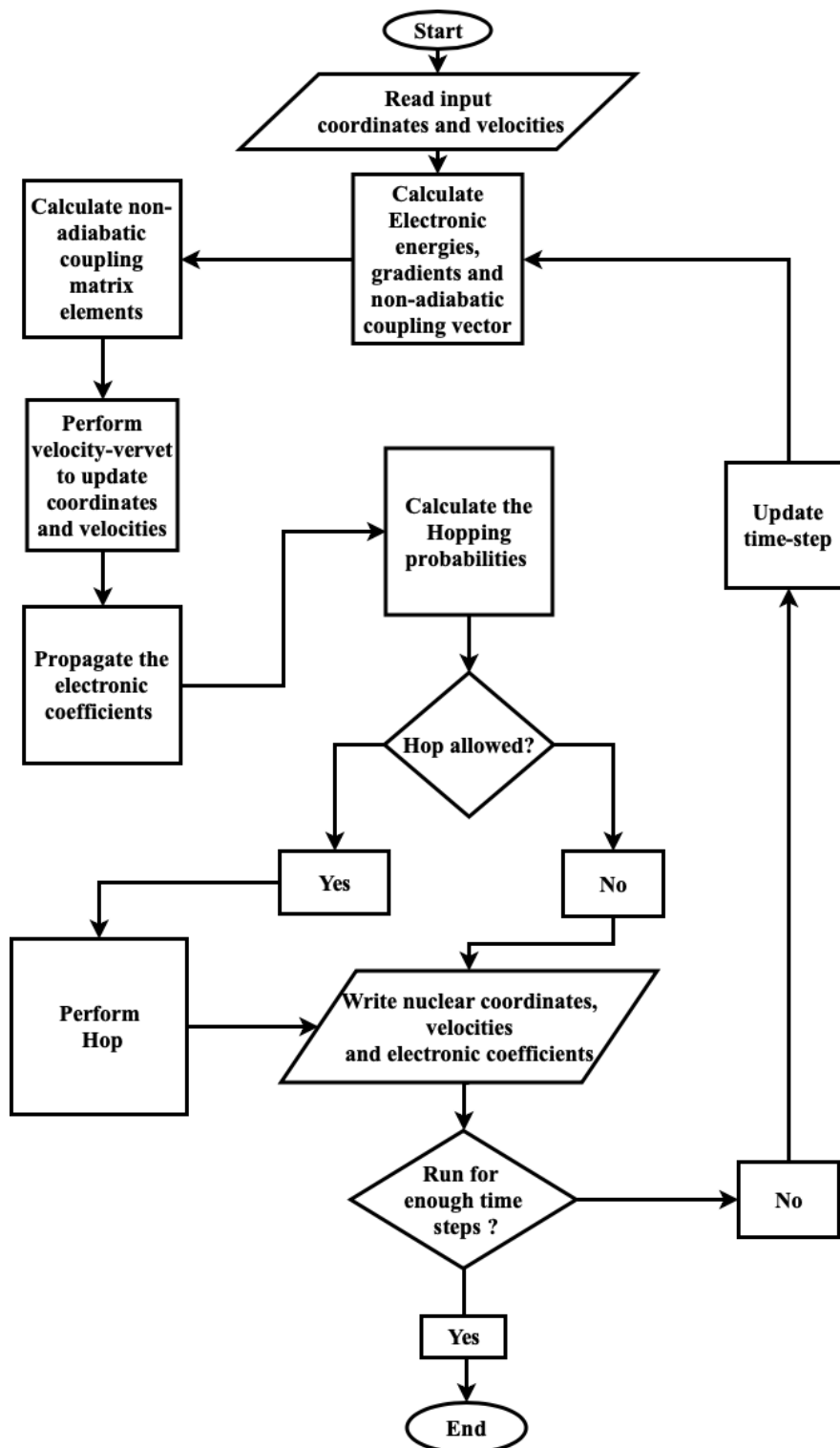


Figure 1.5: Flowchart illustrating the implementation of the fewest switches surface hopping algorithm

## 1.6 Excited-State Electronic Structure Methods

In this section, we review some of the current state-of-the-art excited-state electronic structure methods. More extensive in-depth derivations of these method can be found in the following references.

The wavefunction based approaches beginning from Hartree-Fock to Configuration interaction (CI), including Multi-configurational self-consistent field (MCSCF), and the Coupled cluster (CC) method are described in detail in the book of Szabo and Ostlund [33] and the recent book of Helgaker, Jørgensen and Olsen [34] also covers these aspects. In addition, approximate CC methods and linear response Coupled cluster (LR-CC) theory is reviewed by Christiansen [35] and the detailed description is present in the original literature [36]. Density functional theory (DFT) is a subject of several textbooks [37–39]. Reviews on time-dependent density functional theory (TDDFT) have been published [40, 41]. There is also a good textbook on TDDFT [42]. A comparison between single-reference excited-states based on HF and DFT can be found in a review of Dreuw and Head-Gordon [43].

### 1.6.1 Time-dependent density functional theory

TDDFT allows one to describe the electronic structure of systems that are in the excited state. The foundations of TDDFT is rooted in two fundamental theorems

- Runge-Gross Theorem [44]

*It states that there is a unique, one-to-one correspondence between the time-dependent one-electron density  $n(r,t)$  and an external potential  $v_{ext}(r,t)$  for a many body system with wavefunction  $\Psi$*

- van Leeuwen Theorem [45]

*It states that the time-dependent one-electron density  $n(r,t)$  for a many-body system evolving from  $\Psi(t=0)$  under the influence of an external potential  $v_{ext}(r,t)$  can always be reproduced by a different initial state  $\Psi'(t=0)$  with a different external potential  $v'_{ext}(r,t)$*

If  $v_{ext}$  is the perturbation applied to the system, the linear-response TDDFT (LR-TDDFT) consists of calculation the first order change in density  $\delta n(r)$ , which is related to the linear response kernel  $\delta P$  of the reference ground state (Kohn-Sham) system as

$$\delta n(r) = \sum_{kl}^{all\ orbitals} \psi_k(r) \delta P_{kl} \psi_l(r) \quad (1.32)$$

Using the response function theory, we can calculate the corresponding susceptibility as

$$\chi_{kl} = \frac{f_k - f_l}{\omega - (\epsilon_k - \epsilon_l)} \quad (1.33)$$

where  $\epsilon_k$  are the energies of the orbitals and  $f_k$  their occupation numbers. The generalized susceptibility connects the first order change of the effective potential  $\delta v_{eff}(\omega)$  with the first order change of the response function

$$\delta P_{kl}(\omega) = \frac{f_k - f_l}{\omega - (\epsilon_k - \epsilon_l)} \delta v_{eff}(\omega) \quad (1.34)$$

where  $v_{eff}(\omega)$  contains the frequency dependent term. Assuming that the perturbation takes the form of an oscillating time-dependent electric field,  $\delta P(\omega)$  can be used to compute the tensor components of the frequency dependent dynamic polarizability. Excitation energies are obtained as the poles of the dynamic polarizability. Determination of these poles and the excitation energies can be done by solving the following matrix equations, also known as the Casida equations [46].

During the last two decades, a great effort has been made to develop and improve LR-TDDFT [44,47,48]. LR-TDDFT allows for an accurate calculation of absorption spectra of large molecules for a low computational cost. However using TDDFT, the vertical excitation energies are known to be sensitive to the choice of exchange-correlation (xc) functional. Good accuracy in ground-state DFT calculations does not automatically guarantee the same for excited-state calculations. For example, the B3LYP functional, which has been used widely in ground-state calculations, is known to be inaccurate for the calculation of excited-state properties [49]. In particular, it's time-dependent formulation it is found to be unsuccessful in describing the following processes :

- the polarizability of long chain conjugated systems [50]
- excitation of Rydberg type among excited electronic states [51, 52]
- charge-transfer excitation [53, 54]

The reason for this failure is that at long-range, the exchange potential as implemented in B3LYP behaves as  $-0.2r^{-1}$ , instead of  $r^{-1}$ . To correct this inadequacy, an Ewald split of  $r_{12}^{-1}$  was proposed [55] as follows.

$$\frac{1}{r_{12}} = \frac{1 - \text{erf}(\mu r_{12})}{r_{12}} + \frac{\text{erf}(\mu r_{12})}{r_{12}} \quad (1.35)$$

The first term here accounts for short-range type of interaction while the second term accounts for long-range interaction. The long-range corrected (LC) exchange functional scheme requires a balanced description involving the short-range term which is the DFT exchange and the long-range term which is included in the Hartree-Fock (HF) exchange integral. The equation 1.35 is generalized with two parameters  $\alpha$  and  $\beta$  as

$$\frac{1}{r_{12}} = \frac{1 - [\alpha + \beta \text{erf}(\mu r_{12})]}{r_{12}} + \frac{\alpha + \beta \text{erf}(\mu r_{12})}{r_{12}} \quad (1.36)$$

where  $0 \leq \alpha + \beta \leq 1$ ,  $0 \leq \alpha \leq 1$  and  $0 \leq \beta \leq 1$  should be satisfied. This is regarded as the Coulomb attenuated method (CAM). The  $\alpha$  parameter enables one to incorporate HF exchange over it's whole range and  $\beta$  allows for DFT counter part for the whole range by a factor of  $(1 - (\alpha + \beta))$ .

So B3LYP is implemented with a CAM split of  $\alpha = 0.2$  and  $\beta = 0.0$ ,

$$E_x^{B3} = (1 - \alpha) E_x^{slater} + \alpha E_x^{HF} + C^{B88} \Delta E_x^{B88} \quad (1.37)$$

where  $\Delta E_x^{B88}$  is Becke's 1998 gradient correction for exchange with semi-empirical parameter  $C^{B88} = 0.72$ . CAM-B3LYP has seen to have a significant improvement in the calculation of its excitation bands over other functionals. In particular, the spuriously low charge-transfer states found previously do not appear for CAM-B3LYP [56].

## 1.6.2 Second-order algebraic diagrammatic construction method

Despite the large number of available exchange-correlation functionals in DFT/TDDFT and their levels of sophistication, these methods are not systematically improvable. Quite recently, methods based on Coupled Cluster (CC) approaches like the equations-of-motion coupled-cluster methods (EOM-CC) have been useful in calculating excited states [57]. These methods are an extension of the coupled-cluster approach for excited electronic states, and they form a well-defined hierarchy of approximations (EOM-CC2, EOM-CCSD, EOM-CC3, etc.). Using these methods, the calculated vertical excitation energies are believed to be accurate to within around 0.1 eV [58] - but are very expensive in terms of computing time.

On the other end of the “ladder” of approximations, the approximate coupled-cluster singles-and-doubles model (CC2) is cost-efficient and can be applied to large systems [36]. At the same time, propagator-based approaches have gained considerable attention, especially the second-order polarization propagator approximation (SOPPA) and the algebraic diagrammatic construction (ADC) scheme of the polarization in the second and third order of perturbation theory [ADC(2) and ADC(3)]. [59–63]. The ADC(2) method is closely related to the CC2 method [64], which is the lowest-level coupled-cluster approximation for excited states, and provides a similar level of accuracy .

The interest in applying these methods arose by the recent efficient implementation of the second-order scheme ADC(2) into popular quantum chemistry programs like Turbomole [65], QChem [66] and Psi4 [67].

Starting from a correlated ground state wavefunction  $\psi_0$ , a correlated excited-state basis  $\{\Psi_J^0\}$  can be generated by operating with excitation operators  $\{\hat{C}_J\} = \{\hat{c}_a^\dagger \hat{c}_k, \hat{c}_a^\dagger \hat{c}_b^\dagger \hat{c}_k \hat{c}_l \dots\}$  representing single, doubles .... etc., excitation. The diagonal compact representation of the polarization propagator can be written as (matrix representation) [68, 69]

$$\Pi(\omega) = \mathbf{x}^\dagger (\omega - \Omega)^{-1} \mathbf{x} \quad (1.38)$$

where  $\Omega$  is the diagonal matrix of vertical excitation energies  $\omega_n$  and  $\mathbf{x}$  is the matrix of transition *spectroscopic* amplitudes. In order to derive the ADC approximation scheme, Equation 1.38 is rewritten in a non-diagonal representation as

$$\Pi(\omega) = \mathbf{f}^\dagger (\omega - \mathbf{M})^{-1} \mathbf{f} \quad (1.39)$$

where  $\mathbf{M}$  is the *non-diagonal* representative of an effective Hamiltonian and  $\mathbf{f}$  is the matrix of effective transition moments.

These quantities are now expressed in the intermediate state representation (ISR) as follow

$$\langle M \rangle_{IJ} = \langle \tilde{\psi}_I | \hat{H} - \hat{E}_0^N | \tilde{\psi}_J \rangle \quad (1.40)$$

$$\langle f \rangle_{Jpq} = \langle \tilde{\psi}_J | \hat{c}_p^\dagger \hat{c}_q | \psi_0 \rangle \quad (1.41)$$

Choosing now the  $n^{\text{th}}$  order Møller-Plesset (MP) ground state as a starting point for the derivation of the ISR basis, one arrives at the  $n^{\text{th}}$  order ADC(n) scheme for excitation energies. ADC(n) converges to full CI with increasing  $n$ .

The ISR is particularly convenient, since every operator  $\hat{O}$  can be represented in IS analogous to 1.40 and 1.41,

$$\langle O_{IJ} \rangle = \langle \tilde{\psi}_I | \hat{O} | \tilde{\psi}_J \rangle \quad (1.42)$$

The excited state wave functions can now be constructed explicitly as  $\Psi_n = \sum_J \mathbf{y}_{nJ} \tilde{\psi}_J$  where  $\mathbf{y}$  are ADC eigenvectors. This aids in constructing quantities like one-electron densities, transition densities, etc for interpreting electronic structure.

In contrast to CC methods, the ADC(n) schemes are hermitian and fully size consistent for the calculation of excited-state properties [70, 71]. Needless to say, ADC only yields reasonable results for molecules whose electronic ground state are described well by MP(n) which does not include ground states with multi-reference character. The accuracy of the ADC schemes has recently been thoroughly evaluated by comparison to a benchmark set of medium-sized molecules [72–74]. The accuracy and limits of different ADC schemes and TDDFT are critically examined elsewhere [69, 75].



# Chapter 2

## Publications

### 2.1 Summary : Article 1

The first enclosed manuscript entitled :

*Ultrafast ring-opening and solvent dependent product relaxation of photochromic spironaphthopyran*

was published as an article in *Physical Chemistry Chemical Physics* (PCCP).

Spiropyran and its derivatives are one of the archetypal families of photochromic compounds. Despite extensive studies, their operating mechanism is, as yet, not fully understood [76]. In recent literature [77], there are discrepancies regarding even the most basic aspects of the excited-state dynamics of these compounds, such as the timescale of the formation of the merocyanine photoproduct. In this manuscript, we study the spironaphthopyran molecule to resolve the issue of the timescale and modes involved in the reaction. To this end, using pump-probe absorption spectroscopy we monitored sub-picosecond changes at respective wavelengths of reactant and product absorption and applied extensive dynamical spectral and global fitting analyses. Also to add high-level quantum chemical simulations were performed. In the simulations, we used time-dependent density functional theory (TDDFT) with state-of-the-art nonadiabatic dynamics to reveal the molecules static and dynamical properties treating the entire system at the quantum level and incorporated techniques to simulate internal conversion and vibrational relaxation mechanisms.

In doing so, our work has revealed two main channels of photo-induced dynamics. The reactive channel proceeds to form the merocyanine photoproduct via an excited-state intermediate in about one picosecond (good agreement with dynamics simulation). Furthermore, our work allows us to understand the role of the solvent during the reaction (a much-discussed aspect). The non-reactive channel (rapid internal conversion to the ground state) is mediated by a conical intersection between the  $S_1$  and  $S_0$  state of the reactant. Our work has the potential to open up further exploration of dynamical properties of photochromic compounds, especially spiro-systems which have long been researched for their scope as ultrafast photoswitches and can, in turn, impact the synthetic efforts of such systems towards more robust designs.

This work not only offers a new understanding of the molecules dynamics but also out-

lines an effective strategic approach to tackle outstanding questions regarding the dynamics of photochemical reactions via combined experiment and theory.

- **2019** *Ultrafast ring-opening and solvent dependent product relaxation of photochromic spironaphthopyran.*

Simon F. Bittmann, **Raison Dsouza**, Khalid M. Siddiqui, Stuart A. Hayes , Andreas Rossos, Gastón Corthey, Michał Kochman, Valentyn I. Prokhorenko, R. Scott Murphy, Heinrich Schworer and R. J. Dwayne Miller

*Physical Chemistry Chemical Physics*, 2019, DOI: [10.1039/C9CP02950H](https://doi.org/10.1039/C9CP02950H).

**Raison Dsouza** Theory Lead Author and Equal Contributor

Cite this: DOI: 10.1039/xxxxxxxxxx

## Ultrafast ring-opening and solvent-dependent product relaxation of photochromic spironaphthopyran

Simon F. Bittmann<sup>a,‡</sup>, Raison Dsouza<sup>a,f,‡</sup>, Khalid M. Siddiqui<sup>a,‡</sup>, Stuart A. Hayes<sup>a</sup>, Andreas Rossos<sup>a</sup>, Gastón Corthey<sup>a,b</sup>, Michał Kochman<sup>a,e</sup>, Valentyn I. Prokhorenko<sup>a</sup>, R. Scott Murphy<sup>c</sup>, Heinrich Schwörer<sup>a</sup> and R. J. Dwayne Miller<sup>\*a,d</sup>

Received Date

Accepted Date

DOI: 10.1039/xxxxxxxxxx

www.rsc.org/journalname

The ultrafast dynamics of unsubstituted spironaphthopyran (SNP) were investigated using femtosecond transient UV and visible absorption spectroscopy in three different solvents and by semi-classical nuclear dynamics simulations. The primary ring-opening of the pyran unit was found to occur within 300 fs yielding a non-planar intermediate in the first singlet excited state ( $S_1$ ). Subsequent planarisation and relaxation to the product ground state proceed through barrier crossing on the  $S_1$  potential energy surface (PES) and take place within 1.1 ps after excitation. Simulations show that more than 90% of the trajectories involving C-O bond elongation lead to the planar, open-ring product, while relaxation back to the  $S_0$  of the closed-ring form is accompanied by C-N elongation. All ensuing spectral dynamics are ascribed to vibrational relaxation and thermalisation of the product with a time constant of 13 ps. The latter shows dependency on characteristics of the solvent with solvent relaxation kinetics playing a role.

### 1 Introduction

Photochromic compounds exhibit dramatic changes in their structural, chemical and physical properties upon absorption of light which are generally reversible<sup>1</sup>. This makes them suitable for promising applications, for instance as photoswitches<sup>2-4</sup>, memory devices<sup>5,6</sup> and as tools in biological imaging<sup>7</sup>, motivating research on their synthesis and characterisation<sup>8,9</sup>. An important class of photochromics is that of spiropyrans<sup>10</sup>, which are composed of nearly orthogonal indoline and pyran subunits related by a common  $sp^3$ -hybridised spiro-carbon atom, but can differ in their substituents (see Fig 1). A common view of the photophysical properties of spiropyrans is that the two subunits are electron-

ically uncoupled in the closed (spiro-)form and thus, its absorption spectrum lies in the ultraviolet (UV) region of the electromagnetic spectrum ( $\lambda < 400$  nm). When a UV photon is absorbed by the molecule, the bond between the spiro-carbon and the oxygen in the pyran ring undergoes cleavage leading to a cascade of processes, including opening of the pyran ring, hybridisation of the spiro-carbon and conformational isomerisation. These structural changes yield a planar isomer called merocyanine (MC), in which the two moieties are linked by a methine bridge and become electronically coupled. The improved wave function overlap and delocalisation causes a reduction of the energy difference between the highest occupied and the lowest unoccupied molecular orbital giving rise to an intense absorption of the MC in the visible range. Consequently, the MC form appears coloured in solution. Eight different conformers are in principle possible due to an additional degree of freedom brought upon by the formation of the methine bridge. In Fig 1, one such conformer is shown as an example. Which conformers are most stable depends on the respective spiropyran derivative<sup>11</sup> and the solvent environment<sup>12</sup>.

Understanding the fundamental photophysical processes of spiropyrans has been a matter of great interest for the photochemistry community. In 1952, Fischer and Hirshberg were the first to synthesise spiropyrans and also to characterise the role of temperature and the wavelength of light on the behaviour of this class of compounds<sup>13</sup>. Since then, several studies have been carried out investigating different aspects, such as structural changes during the reaction, their time scales and the quantum yields of possible

<sup>a</sup> Max Planck Institute for the Structure and Dynamics of Matter, Center for Free Electron Laser Science, Luruper Chaussee 149, 22761, Hamburg, Germany; E-mail: dwayne.miller@mpsd.mpg.de

<sup>b</sup> Instituto de Nanosistemas, Universidad Nacional de San Martín, San Martín, Buenos Aires, Argentina

<sup>c</sup> Department of Chemistry and Biochemistry, Research and Innovation Centre, University of Regina, 3737 Wascana Parkway, Regina, SK S4S 0A2, Canada

<sup>d</sup> Departments of Chemistry and Physics, University of Toronto, 80 St. George Street, Toronto, ON M5S3H6, Canada

<sup>e</sup> Department of Physics, Chemistry and Biology (IFM), Linköping University, Linköping, Sweden

<sup>f</sup> Department of Physics, University of Hamburg, Jungiusstrasse 9, 20355 Hamburg, Germany

† Electronic Supplementary Information (ESI) available: [details of any supplementary information available should be included here]. See DOI: 10.1039/C9CP00000x/

‡ S. F. Bittmann, R. Dsouza and K. M. Siddiqui contributed equally to this work.



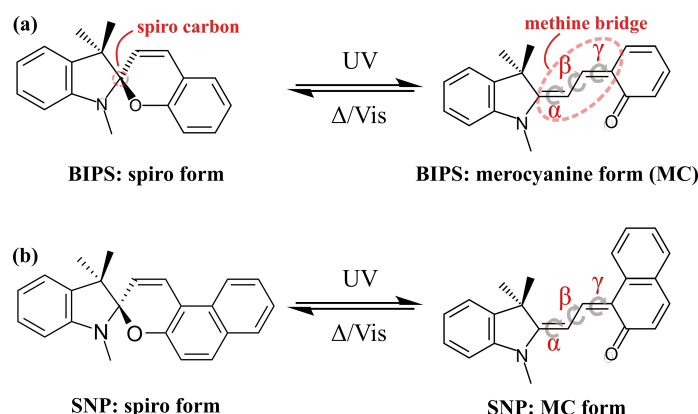


**Fig. 1** Photochemical reaction scheme of spiropyran conversion to merocyanine shown for indolinobenzospiropyran (BIPS, a) and indolinonaphthospiropyran (SNP, b). Due to rotation about the three bonds in the methine bridge (dihedral angles  $\alpha$ ,  $\beta$  and  $\gamma$ ), up to 8 isomers are possible out of which the trans-trans-cis (TTC) configuration is shown. The reverse reaction can be achieved thermally or triggered with visible light.

MC isomers<sup>14,15</sup>.

The most studied spiropyran have been indolinobenzospiropyran (BIPS, see Fig 1 a) and its 6-nitro ( $-\text{NO}_2$ ) substituted analogue. However, the time scale for the ring-opening reaction remains a debated point. In the early 90's, Ernsting and co-workers reported the results of optical pump-probe experiments in the visible range carried out on BIPS solutions in n-pentane<sup>16,17</sup> as well as ethanol<sup>18</sup> and observed the formation of merocyanine species upon excitation at 308 nm with a rise time of  $\sim 0.9$  ps. They found that the spectrum in the 450-600 nm range at 30 ps resembled that of one recorded in the microsecond timescales suggesting that the product is well-established within this time frame. From a sterics argument they predicted the observed species to be either in a trans-trans-cis (TTC) or cis-trans-cis (CTC) conformation or both. A transient mid-infrared study in 2003 from Rini *et al.* cast doubt on the time scale of this photochemical reaction<sup>19</sup>. Based on their measurements, they concluded that a rapid  $S_1 \rightarrow S_0$  internal conversion was the dominant relaxation channel with a quantum yield of  $\sim 90\%$ , while the remaining 10% goes into forming the product via an unknown intermediate with a time constant of 28 ps. On the other hand, a water soluble, pyridinium substituted BIPS, which can be expected to exhibit dynamics similar to BIPS, was investigated by Kohl-Landgraf *et al.* and the MC formation following 350 nm excitation was found to occur within a picosecond<sup>20</sup>.

Spiro-naphthopyran (SNP), which is closely related to BIPS (see Fig 1 b), has been reported to display transient photochromism even in the crystalline state<sup>21</sup>. This renders it a promising target for time-resolved crystallographic studies, which have the capability to unambiguously resolve the question of the MC formation time scale and to provide insight into the structural isomerisation dynamics with atomic resolution<sup>22</sup>, motivating our interest in this system.

For SNP, a rise time of 1.4 ps for the MC absorption band in solution has been reported<sup>16,17</sup>. However, detailed transient absorption data with sub-ps resolution has only been measured up

to 8 ps after UV excitation and only for the non-polar solvent n-pentane. As mentioned, the solvent environment is known to influence the equilibrium between different MC conformers depending on the solvent polarity and capability of forming hydrogen bonds<sup>12</sup>. What role this plays towards the MC formation dynamics however warrants further investigation. Moreover, studies of unsubstituted spiropyran have mainly been carried out with excitation directly to the  $S_1$  state ( $E \sim 4$  eV). Excitation into higher lying electronic states than  $S_1$  can lead to larger excess energies being deposited into the system which can potentially influence the outcome of a photochemical reaction<sup>23-26</sup>. In this context, the solvent can play a determining role on the time scales of vibrational relaxation, as has been reported for instance in the case of 9-methyladenine<sup>27</sup>.

A number of theoretical studies concerning the ring-opening mechanism of spiropyran have been carried out more recently, treating smaller model systems at a high level of theory (CASPT2//CASSCF)<sup>28</sup>. These studies have provided useful insight into the relevant modes and reaction channels leading to either the closed or the open form, but give no direct information about the respective time scales. The latter can be obtained by carrying out excited state dynamics simulations, which has so far only been reported for BIPS<sup>29</sup>.

In this work, we investigated the photochemical dynamics of spiro-naphthopyran up to extended time scales (one nanosecond) using 266 nm femtosecond excitation (4.6 eV) and comparing between a non-polar (n-hexane), a polar aprotic (acetonitrile) and a polar protic (ethanol) solvent environment. We performed femtosecond transient absorption spectroscopy covering the visible (380-700 nm) as well as the ultraviolet spectral range (250-350 nm), where electronic changes associated with the ground state of the spiro-species can be observed. Furthermore, we carried out semi-classical excited state dynamics simulations treating the complete molecule with time-dependent density functional theory and simulating a sufficient number of trajectories to be able to compare the time scales between simulations and experiments. In addition to gaining insight into the ring-opening mechanism and the involved electronic states from theory, this makes it possible to differentiate between chemical reaction dynamics and product relaxation in the analysis of the spectroscopic data.

## 2 Methods

### 2.1 Computational methods

The modified-surface hopping dynamics are calculated using the adiabatic electronic energies and gradients calculated on the fly at time-dependent density functional theory (TDDFT) level of theory using the *ab initio* electronic structure package Gaussian 09<sup>30</sup>. We treated the electronic structure of the SNP molecule with the use of density functional theory (DFT) for the ground electronic state in combination with (linear response) time-dependent DFT (TDDFT) for the relevant excited states. The reactant geometry of the ground state was optimized using DFT using CAM-B3LYP<sup>31</sup> functional with a def2SVP<sup>32</sup> basis set. CAM-B3LYP is a long range-corrected functional, owing to which its accuracy for excited-state potential energy surfaces is superior



to conventional hybrid functionals. Subsequently, the first singlet excited state ( $S_1$ ) was optimised using the same functional and basis set using TDDFT within Tamn-Damncoff Approximation. These calculations were also performed using Gaussian 09.

The simulations assumed that the vertical excitation was instantaneous, with an initial phase space distribution generated by using a vibrational Wigner distribution for the ground state minimum. The phase space coordinates were generated from the total distribution using Monte Carlo sampling. As a by-product of this sampling, the absorption spectra was also calculated from 500 configurations. A spectral window based on experimental excitation energy was used to pick the initial conditions. A total of 30 trajectories were chosen from a larger randomly selected set on the basis of the computed  $S_0$ - $S_2$  and  $S_0$ - $S_3$  transition probabilities. (See Supplementary Information). These trajectories were propagated for 1.1 ps with time steps of 0.5 fs in singlet excited states  $S_2$  and  $S_3$ .

## 2.2 Experimental details

1,3,3-Trimethylindolino- $\beta$ -naphthopyrrolospiran (SNP) powder was purchased from TCI Chemicals, Japan and used without further purification. Spectroscopic grade n-hexane, ethanol and acetonitrile were used to prepare SNP solutions with a concentration of 1.5 mM. To obtain the respective spectra of merocyanine, the solutions were irradiated continuously with 266 nm laser light until reaching a photostationary state.

Transient absorption experiments were performed using a Titanium:Sapphire (Ti:Sa) femtosecond laser system (800 nm central wavelength, 1 kHz). In all measurements, the samples were excited at 266 nm with a fluence of  $4 \text{ mJ}\cdot\text{cm}^{-2}$  (490 nJ pulse energy with a beam diameter of  $120 \mu\text{m}$  FWHM) and a repetition rate of 500 Hz. The visible probe light (380-700 nm) was generated by focusing 800 nm pulses in water ( $200 \mu\text{m}$  cuvette), with the magic angle ( $54.7^\circ$ )<sup>33</sup> between the pump and probe polarisations. For the UV supercontinuum (250-350 nm), 400 nm pulses passing through a quarter-wave plate to create circular polarised light were focused in a rotating [001] calcium fluoride crystal.<sup>34</sup> The polarisation of the resulting UV continuum was not modified and assumed to be circular. Sample solutions were flowed through an in-line UV-quartz cuvette with a  $200 \mu\text{m}$  thin window. The transient absorption signal was calculated as:

$$\Delta A(\lambda, \Delta t) = -\log\left(\frac{I_{ON}(\lambda, \Delta t)}{I_{OFF}(\lambda)}\right) \quad (1)$$

where  $I_{OFF}(\lambda)$  and  $I_{ON}(\lambda, \Delta t)$  are the background-corrected probe spectra transmitted through the unexcited and the excited sample, respectively,  $\Delta t$  is the time delay between pump and probe and  $\lambda$  is the probe wavelength. Keeping the probe repetition rate at 1 kHz, the  $I_{OFF}(\lambda)$  and  $I_{ON}(\lambda, \Delta t)$  spectra were recorded alternately. For the UV/UV measurements, every third and fourth probe pulse was blocked using a mechanical chopper to enable the subtraction of the pump scattering background at 266 nm (see supplementary)<sup>35</sup>. The temporal resolution was determined from a cross-correlation measurement in the neat solvent as  $170 \pm 10$  fs and the sensitivity of the measurement was  $10^{-4}$  OD.

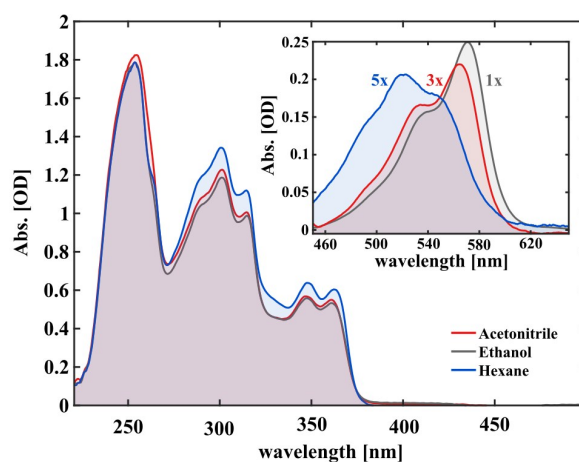


**Fig. 2** Steady-state absorption spectra of 1.5 mM SNP solutions in the UV and visible range. The inset shows the merocyanine spectra in the steady state under UV irradiation (photostationary state), scaled for comparison.

## 3 Results and Discussions

### 3.1 Steady-state spectra

The UV/Vis absorption spectra of 1.5 mM solutions of SNP in hexane, ethanol and acetonitrile are shown in Fig 2. At thermal equilibrium, the molecules exist mainly in the closed form (SNP) which only absorbs below 380 nm. From this spectrum, three main bands can be seen, which show no significant solvent dependence.

The inset of Fig 2 shows the respective absorption spectra of the merocyanine form in the photostationary state. Immediately obvious are their different shapes and/or positions. The MC spectrum in hexane displays a maximum at  $\sim 520$  nm and an additional spectral feature on either side of it. For acetonitrile and ethanol, once more at least three peaks can be deciphered. Two are intense peaks with the longest wavelength peak being the most intense and one smaller shoulder at the lower wavelength tail. The MC spectra in ethanol and acetonitrile have similar shapes and are red-shifted with respect to the corresponding spectrum in hexane. The bathochromic shift is most pronounced for ethanol showing a 17 nm shift of the lower absorption edge with respect to hexane and 5 nm with respect to acetonitrile. Notably, the overall absorption under the same excitation conditions follows the same trend with hexane showing the least and ethanol the highest absorption (see the scaling factors in Fig 2). This hints at the solvent acting to stabilise the merocyanine form, which is discussed further in the supplementary information.

### 3.2 Transient absorption experiments

#### 3.2.1 UV-Visible

Measured transient absorption spectra of SNP dissolved in the three respective solvents are shown in Fig 3 a-c for the first 14 ps after 266 nm excitation. Spectral cuts at chosen time delays from scans covering the range up to 100 ps after excitation are pre-



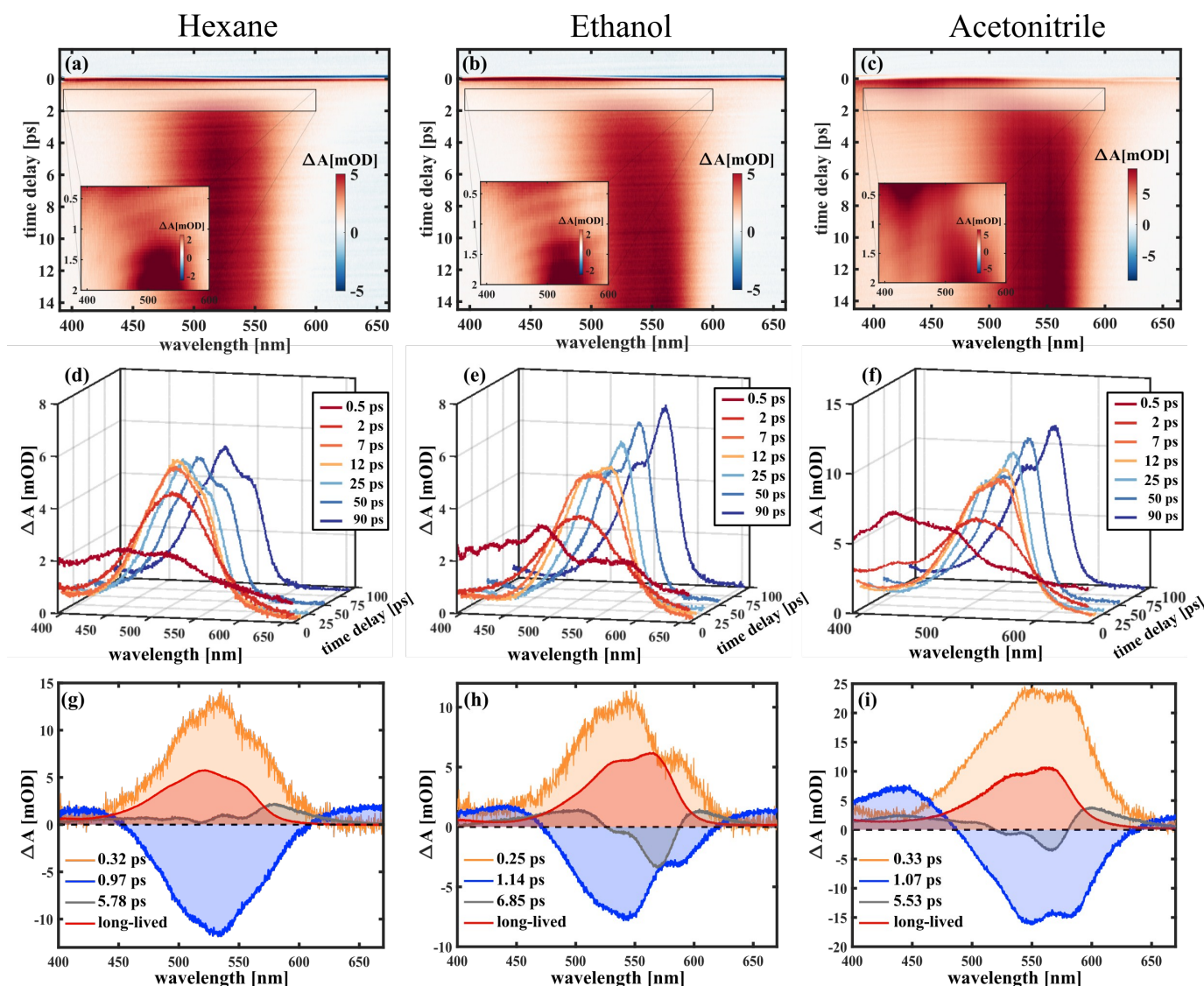


**Fig. 3** Transient absorption spectra of SNP in hexane (a,d,g), ethanol (b,e,h) and acetonitrile (c,f,i), probing in the visible. Depicted are TA maps for the first 14 ps (upper panel), spectral traces for selected delay times within 100 ps after excitation (middle panel), and decay associated spectra from global fitting (lower panel) for all three solvents.

sented in the middle panel of the figure. Measurements up to one nanosecond show that there is no significant spectral evolution beyond 100 ps (see supplementary). The signal observed at time zero is due to the cross-phase modulation (CPM) of the pump and the probe pulse in the solvent. Around 0.3 ps, a broad spectrum appears peaking at 450 nm with an extended tail reaching 650 nm. This signal decays within 1-2 picoseconds accompanied by the emergence of a band in the visible region (450-650 nm). Closer inspection of the first two picoseconds reveals that between 0.3 and 1.2 ps, the maximum continuously shifts from the initial band to the spectrum centered around 550 nm (see insets of Figs 3 a-c). From two picoseconds onwards, the initially structureless spectrum evolves over time towards the steady-state spectrum in the respective solvent becoming narrower and more intense. In the ethanol solution, an additional red-shift in wavelength most prominently within 2-7 ps can be observed, which is

absent in case of the other solvents.

To analyse the data in more detail, we have applied two methods, a global fit routine<sup>36</sup> on the one hand and a dynamic Gaussian line shape analysis on the other hand. The decay-associated spectra (DAS) from global fitting using four exponential components for the time window between 0.3 and 14 ps are shown in the lowest panel of Fig 3. A single component with a lifetime of  $\sim 1.0$  ps (DAS2, blue line) describes both the decay of the initially broad spectrum (positive sign of DAS2) and the rise of the band between 450 and 600 nm (negative sign of DAS2) in all solvents. The decay-associated spectrum with the shortest lifetime of around 0.3 ps (DAS1, orange line) has a positive amplitude between 450 and 600 nm, mirroring the negative region of DAS2, thus describing a delayed onset of the latter. The intermediate component (DAS3, grey line) describes the spectral development from the initial band towards the long-lived component (DAS4,



**Table 1** Time constants from fits of the evolution of position ( $\tau_{pos}$  for overall peak position and  $\tau_{spac}$  for the peak spacing) and FWHMs ( $\tau_{FWHM}$ ) of the Gaussian peaks (Key: r - rise; d - decay).

|              | $\tau_{pos}$ [ps] | $\tau_{spac}$ [ps] | $\tau_{FWHM}$ [ps] |
|--------------|-------------------|--------------------|--------------------|
| Acetonitrile | 13 ± 0.2 (r)      | 21 ± 3 (r)         | 13 ± 0.3 (d)       |
| Hexane       | 13 ± 0.5 (r)      | 16 ± 1 (r)         | 13 ± 0.8 (d)       |
| Ethanol      | 50 ± 5 (d)        | 33 ± 8 (d)         | 14 ± 0.4 (d)       |

red line), which represents the spectrum at 14 ps. Although the global fitting represents the data well, interpreting the time-dependent spectral shift is not straightforward. Therefore, we treat the intermediate time constant in a separate analysis involving decomposition of the spectra into Gaussian functions, which is described in the following.

Such a dynamic Gaussian line shape analysis is able to describe spectral shifts and provides information about the temporal evolution of the peaks constituting the spectra. For this purpose, the spectra (converted to wavenumbers) for each time point were fit with a sum of four Gaussian functions (three in case of ethanol) tracking their respective spectral positions, widths and areas from 100 ps down to 9 ps after excitation. A detailed description of the fitting procedure and a model comparison can be found in the supplementary information. After careful evaluation of different constraints to the parameters it was found that the data in this time window could be described properly by a simplified model, which ascribes the spectral fine structure to a vibrational progression with equal spacings between the peaks and a linear increase in peak width from lowest transition energy to highest. It was thus possible to fit all peak widths  $w_i$  with a single parameter  $w_1$  by using the relation  $w_i = i \cdot w_1$  with  $i$  being the peak number. The peak positions were characterised by one parameter for the absolute position  $b_1$  and one for the peak spacing  $\delta$  related by  $b_i = b_1 + (i - 1) \cdot \delta$ . All three parameters exhibited a monoexponential behaviour over time and the respective time constants are shown in Table 1.

Notably, both in acetonitrile and hexane, a time constant of 13 ps was found for the relative changes in peak positions, which blue-shift, and for the peak widths, which decay over time. While in ethanol a similar decay constant (14 ps) was obtained for the FWHM values, the aforementioned red-shift is reflected in the peak position changes with a time constant of 50 ps. Furthermore, in the former two solvents the peak spacing increases over time, while decreasing with a time constant of 35 ps in case of ethanol.

### 3.2.2 UV-UV

The transient UV absorption map of SNP in n-hexane from is shown in Fig 5. Measurements were also carried out in ethanol but exhibited no qualitative difference (see supplementary). Around time zero, following the CPM signal, an intense absorption covering the entire measured range is observed. As the initial absorption decays within 2 ps, a negative feature between 270 and 305 nm and a positive feature between 305 and 340 nm start to dominate. After this time, the spectra do not change significantly either in their intensities or profiles within the measured time window up to one nanosecond (see Fig 5 d).

The data were fitted using two decay associated spectra, one of which gave a time constant of 0.6-0.7 ps representing the broad absorption near time zero, whereas the second time constant exceeded the measurement time window ( $\gg 1$  ns).

### 3.3 Excited-state dynamics simulations

The populations of the first four electronic states over time obtained from semi-classical excited state dynamics simulations and averaged over all 30 trajectories are depicted in Fig 6. Starting with an initial population of 0.5 in both the  $S_2$  and the  $S_3$  state, the dynamics proceed via internal conversion processes into  $S_1$ . Subsequently, the molecules relax to the ground state of either the merocyanine or the closed-ring form. The populations were fitted with a unidirectional, sequential kinetic model to obtain the transfer rates between states. To enable an accurate fitting of the  $S_1$  population dynamics, the decay of the initially occupied superposition state between  $S_3$  and  $S_2$  was described with a single rate constant. The resulting time constant for the transfer to  $S_1$  was 90 fs, while transfer from  $S_1$  to  $S_0$  occurred with a time constant of 1.3 ps. This rate constant represents a combination of all relaxation pathways to the ground states of either the SNP or the MC form.

In 14 of the 30 simulated trajectories, C-O bond breaking occurred along the  $S_1$  vibrational relaxation coordinate and the carbon hybridisation changed from  $sp^3$  to  $sp^2$ . As a result of this, the two orthogonal moieties rotated with respect to each other along the methine bridge. This bridge can be described by using the three dihedral angles  $\alpha$ ,  $\beta$  and  $\gamma$  along it (see Fig 1). The various orientations of these angles determine the final conformer to be formed. Notably, only one of these trajectories led back to the spiro form, once the bond had been broken.

Plots of the C-O bond distances during the first 700 fs for both trajectories yielding the open-ring form and trajectories leading back to the closed form are shown in Fig 7. The bond breaking trajectories involve rapid elongation of the C-O bond from the equilibrium distance of 1.5 Å to about 3.5 Å. Subsequently, the C-O distances fluctuate around that value and any further changes upon conversion towards the planar form occur on a longer time scale. To characterise the ring-opening time, the formation of open-ring isomers was obtained using a C-O bond elongation threshold of 1 Å and fitted with an exponential function starting at 90 fs. This yielded a ring-opening time constant of 350 fs (see supplementary). Based on the geometry optimisation on the first excited state, a minimum on the  $S_1$  potential energy surface was found corresponding to an open-ring non-planar structure with a C-O distance of 2.7 Å and dihedral angles of  $\alpha = -132^\circ$ ,  $\beta = 5.9^\circ$  and  $\gamma = 43.8^\circ$ .

In case of the trajectories where the molecules did not undergo C-O bond breaking, but relaxed to the ground state of SNP, a temporary elongation of the bond between the indoline nitrogen and the spiro-carbon of  $1.1 \pm 0.1$  Å for a duration of  $100 \pm 30$  fs occurred during the transfer from  $S_1$  to  $S_0$ . The temporal correlation between the elongation and relaxation to  $S_0$  is demonstrated in Fig 8 and is in agreement with previously reported CASPT2//CASSCF studies on BIPS<sup>28</sup>.



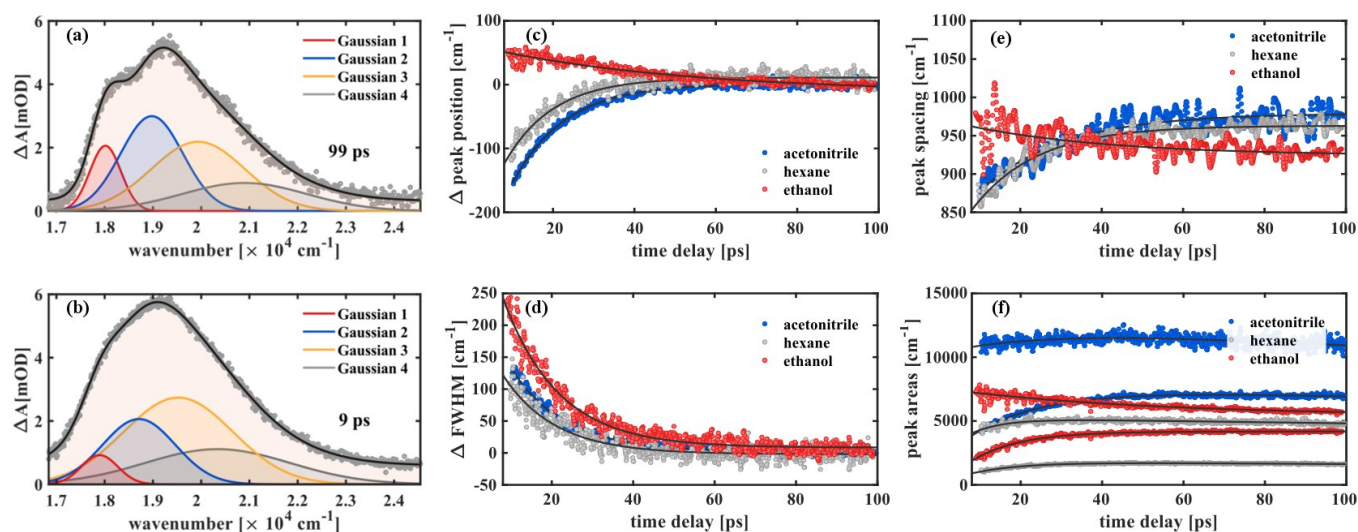


**Fig. 4** Line shape analysis of the transient UV/vis absorption data. The Gaussian components are labeled from 1 to 4, where Gaussian 1 refers to the peak at the lowest energy and Gaussian 4 is the highest energy peak. The fit is shown for the spectra in hexane at 99 ps (a) and 9 ps (b) after excitation representing the analysed time window. The changes in peak position and FWHM values of Gaussian 1 for all three solvents are shown in Figs (c) and (d), respectively. Fig (e) shows the peak spacings and Fig (f) the areas of the first two Gaussians for each solvent (in all three cases, the larger area belongs to the second peak).

## 3.4 Discussions

### 3.4.1 Ring-opening and isomerisation dynamics

A schematic energy diagram of the ring-opening dynamics of SNP based on our interpretation of the experimental and theoretical results is presented in Fig 9. Upon 266 nm excitation, the ground state of SNP is depopulated and high-lying excited states are populated. According to our simulations, internal conversion from  $S_3$  and  $S_2$  to the  $S_1$  state occurs rapidly with a time constant of 90 fs, which is below our experimental time resolution. The instrument response limited, positive signal observed in the TA experiments (Fig 3) can thus be attributed to absorption from the  $S_1$  state, in agreement with previously reported assignments<sup>16,17</sup>.

On the pathway leading to the MC product (see Fig 9 a), the wave packet propagates on the  $S_1$  potential energy surface towards an excited state minimum. During this propagation, the bond between the spiro-carbon and the pyran oxygen is elongated and eventually broken. This results in an open-ring intermediate with nearly orthogonal arrangement of the two subunits according to the  $S_1$  geometry optimisation. The formation of this intermediate manifests as a delayed onset of the product band, which is found to be around 300 fs (see section 3.2.1) and is in good agreement with the bond breaking time of 350 fs obtained from simulations. Importantly, our simulations show that the ring-opening dynamics occur exclusively on the  $S_1$  surface regardless of the excitation wavelength. Subsequent propagation in the next 0.8-0.9 ps involves crossing of an energy barrier on the  $S_1$  surface and the passage through a conical intersection (CI) towards the planar MC configuration in the electronic ground state. This interpretation is consistent with the observed red-shift of  $\sim 100$  nm

( $4000\text{ cm}^{-1}$ ) in the absorption spectrum occurring between 0.3 and 1.1 ps. The fact that all subsequently observed spectral shifts are either towards shorter wavelengths or at least an order of magnitude smaller supports the suggestion that no further planarisation takes places.

As our simulations show that only one out of 14 trajectories involving breaking of the C-O bond led back to the spiro form, we conclude that the bifurcation into two main relaxation channels occurs earlier than 300 fs post-excitation. The key driving mode for internal conversion to the spiro form (see Fig 9 b) has been proposed to involve C-N elongation in a theoretical study mapping the potential energy surfaces<sup>28</sup>, which is also corroborated from our excited-state dynamics simulations.

Important insight regarding the time scales of both reaction pathways can be gained from the transient UV absorption data (see Fig 5). The long-lived differential absorption can be attributed to depletion of the spiro-form and formation of MC and both positive and negative signals in this range do not change significantly after 1-2 ps, except for residual decay of the strong excited state absorption. Besides further supporting our previous assignment of the MC formation time, this observation suggests that relaxation back to SNP also occurs within 1 ps or less.

### 3.4.2 Merocyanine ground-state dynamics and solvent effects

Based on the interpretations given in the previous section, we assign the spectral dynamics observed after 2 ps in the visible range mainly to relaxation of the planar open-ring isomer in the electronic ground state. This is discussed in the following based on the outcome of our line shape analysis (Fig 4).

In all cases, a narrowing of the bands was found with a time constant of 13 ps for acetonitrile and hexane and 14 ps for



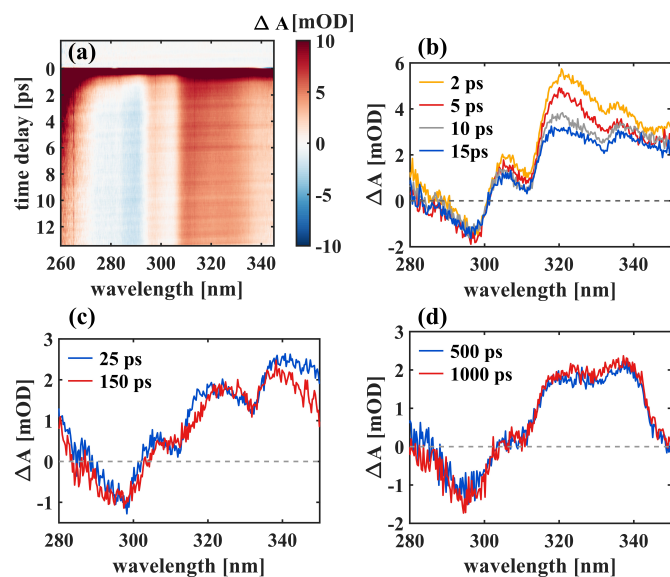


**Fig. 5** UV transient absorption of SNP in hexane, excited at 266 nm. An intense broad absorption around time zero decays within 1 ps revealing a long-lived difference spectrum with decreased absorption between 270 and 305 nm and increased absorption between 305 and 340 nm with respect to the closed-ring form.

ethanol. The reason for narrowing can be that the product configuration space is converging towards the most stable structural conformer<sup>37</sup> or dissipation of vibrational energy to the environment<sup>38,39</sup>. The observed overall blue-shift of the product band in hexane and acetonitrile can be explained analogously in the context of change in occupation number of vibrational states from higher to lower due to intramolecular vibrational relaxation in the electronic ground state and vibrational cooling via collisions with surrounding solvent molecules. The excellent match of the time scales between the blue-shift and the narrowing in these two solvents supports this assignment.

The latter effect is masked in case of ethanol by a dynamic decrease in transition energies resulting in a red-shift of 50  $\text{cm}^{-1}$  within 10 and 100 ps. Furthermore, the energy difference between the vibrational levels decreases over time in ethanol in contrast to the other two solvents. We note that out of the three solvents used in this study, ethanol is the only one capable of forming hydrogen bonds with merocyanine. In addition, its viscosity is higher by a factor of 3 compared to the other two solvents ( $1.1 \cdot 10^{-3}$  Pa·s for ethanol and  $\sim 0.3 \cdot 10^{-3}$  Pa·s for both acetonitrile and n-hexane). These characteristics could account for the observed differences, but an unambiguous assignment exceeds the scope of this work. However, the particularity of solvation in ethanol has been reported previously and it has been shown by Horng *et al.*, using time-resolved emission of coumarin 153 as solute, that ethanol exhibits significantly more complex relaxation dynamics than the other two solvents, with a long-lived component of  $\sim 30$  ps.<sup>40</sup> In contrast, solvation times in acetonitrile ( $\sim 0.6$  ps) and non-polar solvents ( $\sim 0.3$  ps) were found to be in the sub-ps regime.<sup>40,41</sup> This suggests that in case of ethanol, the solvent relaxation causing a red-shift of the bands dominates the ps-dynamics whereas the effect would be invisible in cases of

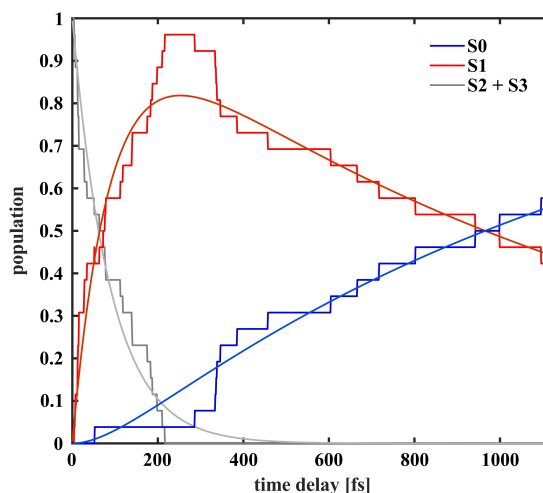


**Fig. 6** Populations of the first four electronic states of SNP after UV excitation according to the excited state dynamics simulation. The data were averaged over 30 trajectories and fit with a kinetic model.

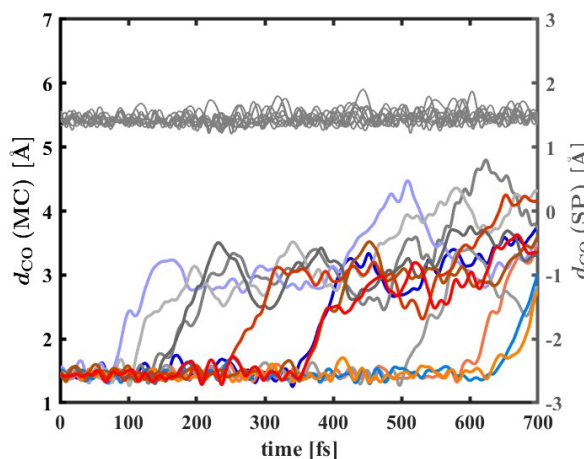


**Fig. 7** Bond distance  $d_{\text{CO}}$  between the spiro-carbon and the pyran oxygen for the excited state dynamics trajectories leading to MC (coloured lines, left ordinate) and trajectories leading back to the SNP ground state (grey lines, right ordinate). In the MC trajectories,  $\text{C}_{\text{spiro}}\text{-O}$  bond breaking occurs via rapid elongation of the bond of about 1.5 Å taking less than 100 fs and no return to a closed-ring isomer was found. In contrast, no significant changes in  $\text{C}_{\text{spiro}}\text{-O}$  bond length were present in the trajectories leading back to the ground state of SNP.



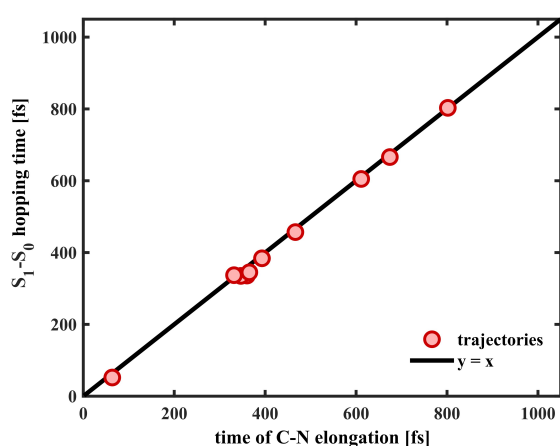


**Fig. 8** Temporal correlation between the transfer from  $S_1$  to  $S_0$  and the  $C_{\text{spiro}}\text{-N}$  elongation of  $1.1 \pm 0.1 \text{ \AA}$  in the trajectories that did not undergo  $C_{\text{spiro}}\text{-O}$  bond breaking. The values on the abscissa for each trajectory were obtained by taking the mean of the time points during which the  $C_{\text{spiro}}\text{-N}$  bond was elongated above the half-maximum value. The black line ( $y = x$ ) is shown as reference for a perfect correlation.

acetonitrile and hexane since the relaxation time scales coincide with those of the reaction itself. Thus, our observations and analyses reflect the distinctive solvent relaxation dynamics in ethanol.

An unambiguous interpretation of the peak area dynamics is not possible without additional information about the excited state PES and the corresponding vibrational wavefunctions and Franck-Condon factors. The possibility of interconversion between different MC conformers further complicates the interpretation. The fact that the spectra could be adequately described by a simple vibrational progression model implies that the peaks in the final spectrum correspond to a vibrational fine structure originating from a single conformer. The energy difference between the peaks is found to be on the order of  $1000 \text{ cm}^{-1}$ , which falls well within the stretching frequency of C-C bonds in organic molecules. It should be stressed however that the identity of the conformer that is formed cannot be revealed with certainty by means of electronic spectroscopy, since the merocyanine isomers are geometrically close and likely to have similar electronic structures. This has recently been demonstrated by Xiong *et al.* for the closely related spironaphthoxazine<sup>7</sup>.

The key insight from this analysis of the spectral dynamics between 9 and 100 ps is thus, that they can be ascribed purely to thermalisation (13 ps) of the product and in case of ethanol solvation equilibration ( $\sim 50$  ps). This confirms that the chemical reaction itself takes place on a faster time scale.

## 4 Conclusion

Combining semi-classical nuclear dynamics simulations and transient absorption spectroscopy in both the visible and the UV, the present study provides deeper insight into the mechanism and following product equilibration of the photochemical reaction of unsubstituted spiropyrans. Thorough analysis of the spectral data up to 100 ps after excitation allowed differentiating between the dynamics of the isomerisation reaction itself and product relaxation

and equilibration. Evidence was found for an open-ring reaction intermediate being formed within 300 fs which subsequently planarises yielding the merocyanine form in a vibrationally hot ground state within 1.1 ps. Theoretical calculations confirm the existence of such an intermediate with an open-ring, non-planar geometry. According to the dynamics simulations, all trajectories that showed C-O bond breaking led to the planar MC, whereas trajectories returning to the SNP ground state did not exhibit any significant C-O bond elongation, but were driven by a C-N stretch mode in accordance with previously reported calculations. The internal conversion back to the initial state was found to occur within less than 1 ps.

The product relaxation dynamics could be described with a simplified vibrational progression model suggesting that vibrational relaxation takes place with a time constant of  $\sim 13$  ps. While the chemical dynamics did not exhibit any considerable solvent dependence, product equilibration in ethanol was influenced by solvent relaxation dynamics. With the present study, we have demonstrated that a dynamic line shape analysis is a useful method to describe time-dependent spectral shifts and spectral fine structure, complementing conventional global fit routines.

## Conflicts of interest

The authors declare no conflicts of interest.

## Acknowledgements

This work was funded by the Max Planck Society. We thank Dr Hong Guang-Duan and Dr Ajay Jha for scientific advice and Dr Arunangshu Debnath and Dr Zheng Li for helpful discussions. This work made use of the GWDG High Performance Computing Facility at Göttingen (<https://www.gwdg.de/application-services/high-performance-computing>).

## 5 Author contributions

S.F.B., R.D. and K.M.S. contributed equally to this work. K.M.S., G.C. and S.F.B. constructed the experimental setup. S.F.B. and K.M.S. led the experimental front. Data analysis was carried out by S.F.B., K.M.S., R.D., S.A.H. and V.I.P. R.D. led the theoretical efforts with contributions from M.K. A.R., S.F.B. and K.M.S. prepared samples for the experiments. All authors contributed towards data interpretations and discussions. The project was conceived by R.J.D.M. and directed by R.J.D.M. and K.M.S.

## References

- 1 *Photochromism: Molecules and Systems*, ed. H. Dürr and H. Bouas-Laurent, Elsevier BV, 2003.
- 2 M. E. Gemayel, K. Börjesson, M. Herder, D. T. Duong, J. Hutchison, C. Ruzié, G. Schweicher, A. Salleo, Y. Geerts, S. Hecht, E. Orgiu and P. Samori, *Nature Communications*, 2015, **6**, 5054–5075.
- 3 E. Orgiu, N. Crivillers, M. Herder, L. Grubert, M. Pätzel, J. Frisch, E. Pavlica, D. T. Duong, G. Bratina, A. Salleo, N. Koch, S. Hecht and P. Samori, *Nature Chemistry*, 2012, **4**, 675–679.
- 4 D. Bléger and S. Hecht, *Angewandte Chemie International Edition*, 2015, **54**, 11338–11349.



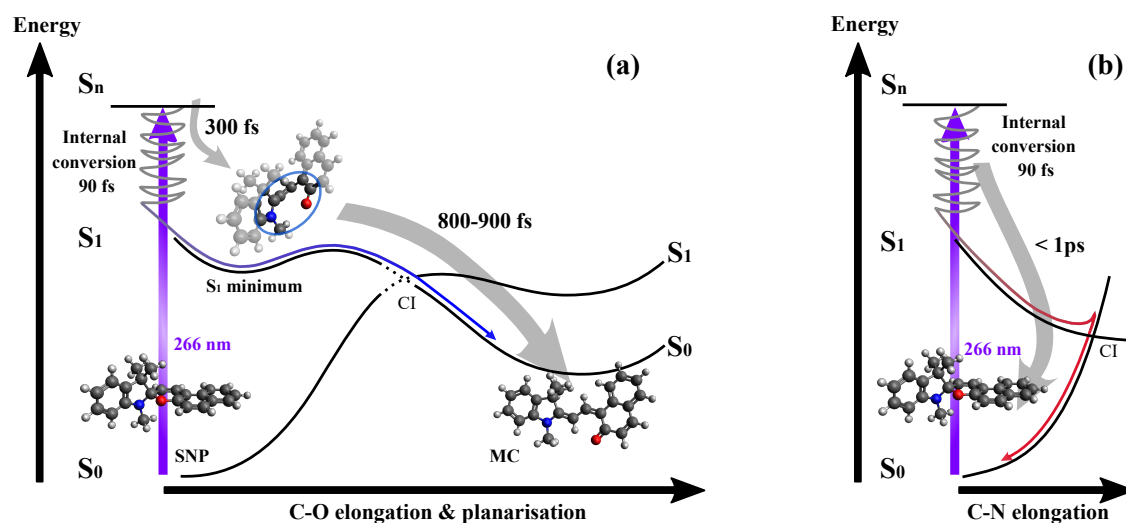


**Fig. 9** Schematic illustration of the reaction pathways along the relevant reaction coordinates. Upon excitation at 266 nm, internal conversion to the  $S_1$  potential energy surface (PES) occurs within 90 fs according to simulations. (a) On the trajectory leading to MC, the  $C_{\text{spiro}}\text{-O}$  bond is broken leading to an open-ring intermediate with a formation time of 300 fs according to experiments (350 fs in simulations). The  $S_1$  minimum structure shown here was found by geometry optimisation. The subsequent planarisation and relaxation to the ground state of MC occurs with a time constant between 800 and 900 fs based on our experimental data. (b) Relaxation back to the ground state of the closed-ring form involves elongation of the  $C_{\text{spiro}}\text{-N}$  bond rather than the  $C_{\text{spiro}}\text{-O}$  bond, according to our simulations and previously reported PES calculations. Transient absorption measurements in the UV range indicate that this relaxation takes less than 1 ps.

- 5 G. Berkovic, V. Krongauz and V. Weiss, *Chemical Reviews*, 2000, **100**, 1741–1754.
- 6 M. Irie, T. Fukaminato, K. Matsuda and S. Kobatake, *Chemical Reviews*, 2014, **114**, 12174–12277.
- 7 Y. Xiong, A. V. Jentzsch, J. W. M. Osterrieth, E. Sezgin, I. V. Sazanovich, K. Reglinski, S. Galiani, A. W. Parker, C. Eggeling and H. L. Anderson, *Chemical Science*, 2018, **9**, 3029–3040.
- 8 C. Beyer and H.-A. Wagenknecht, *The Journal of Organic Chemistry*, 2010, **75**, 2752–2755.
- 9 M. Livendahl, J. Jamroskovic, M. Hedenström, T. Görlich, N. Sabouri and E. Chorell, *Organic & Biomolecular Chemistry*, 2017, **15**, 3265–3275.
- 10 R. Klajn, *Chem. Soc. Rev.*, 2014, **43**, 148–184.
- 11 J. Buback, P. Nuernberger, M. Kullmann, F. Langhojer, R. Schmidt, F. Würthner and T. Brixner, *The Journal of Physical Chemistry B*, 2011, **115**, 3924–3935.
- 12 H. Takahashi, K. Yoda, H. Isaka, T. Ohzeki and Y. Sakaino, *Chemical Physics Letters*, 1987, **140**, 90–94.
- 13 E. Fischer and Y. Hirshberg, *Journal of the Chemical Society*, 1952, 4522–4524.
- 14 R. D. P. L. J. A. E. P. R. G. A. Kellmann, F. Tfibel, *J. Chem. Soc.*, 1961, 156–163.
- 15 A. Kellmann, F. Tfibel, R. Dubest, P. Levoir, J. Aubard, E. Potier and R. Guglielmetti, *J. Photochem. Photobiol. A*, 1989, **49**, 63–73.
- 16 N. P. Ernstring, B. Dick and T. Arthen-Engeland, *Pure and Applied Chemistry*, 1990, **62**, 1483–1488.
- 17 N. P. Ernstring and T. Arthen-Engeland, *The Journal of Physical Chemistry*, 1991, **95**, 5502–5509.
- 18 N. P. Ernstring, *Chemical Physics Letters*, 1989, **159**, 526–531.
- 19 M. Rini, A.-K. Holm, E. T. J. Nibbering and H. Fidler, *Journal of the American Chemical Society*, 2003, **125**, 3028–3034.
- 20 J. Kohl-Landgraf, M. Braun, C. Özçoban, D. P. N. Gonçalves, A. Heckel and J. Wachtveitl, *Journal of the American Chemical Society*, 2012, **134**, 14070–14077.
- 21 T. A. Mototsugu Suzuki and H. Masuhara, *Physical Chemistry Chemical Physics*, 2002, **4**, 185–192.
- 22 R. J. D. Miller, *Science*, 2014, **343**, 1108–1116.
- 23 T. Elsaesser and W. Kaiser, *Annual Review of Physical Chemistry*, 1991, **42**, 83–107.
- 24 J. C. Owrtusky, D. Raftery and R. M. Hochstrasser, *Annual Review of Physical Chemistry*, 1994, **45**, 519–555.
- 25 G. A. Voth and R. M. Hochstrasser, *The Journal of Physical Chemistry*, 1996, **100**, 13034–13049.
- 26 T. Brust, S. Malkmus, S. Draxler, S. A. Ahmed, K. Rück-Braun, W. Zinth and M. Braun, *Journal of Photochemistry and Photobiology A: Chemistry*, 2009, **207**, 209–216.
- 27 C. T. Middleton, B. Cohen and B. Kohler, *The Journal of Physical Chemistry A*, 2007, **111**, 10460–10467.
- 28 F. Liu and K. Morokuma, *Journal of the American Chemical Society*, 2013, **135**, 10693–10702.
- 29 G. Zhai, S. Shao, S. Wu, Y. Lei and Y. Dou, *International Journal of Photoenergy*, 2014, **2014**, Article ID 541791, 9 pages.
- 30 M. Frisch, G. Trucks, H. Schlegel, G. Scuseria, M. Robb, J. Cheeseman, G. Scalmani, V. Barone, B. Mennucci, G. Pe-



The Supporting Information is available free of charge  
on the ACS Publications website at  
<http://www.rsc.org/suppdata/c9/cp/c9cp02950h/c9cp02950h1.pdf>.

## 2.2 Summary : Article 2

The second paper entitled:

*The Oscillatory Photoelectron Signal of N-Methylmorpholine as a Test Case for the Algebraic-Diagrammatic Construction Method of Second Order* was published as an article in The Journal of Physical Chemistry A (2018).

Therein, we were motivated by recent progress in the characterization of molecular Rydberg states with the use of time-resolved photoelectron spectroscopy (TRPES) and our work aimed to advance the state of the art in the computational modeling of these systems, with the ultimate goal of enabling accurate prediction of TRPES spectra.

To this end, we assessed the performance of the second-order algebraic diagrammatic construction (ADC(2)) theory, in combination with a semi-classical method for the propagation of nuclear dynamics, in the simulation of the TRPES spectrum of a representative molecule whose excited-state evolution occurs in Rydberg states. As the model system for the present study, we selected the tertiary aliphatic amine *N*-methyl morpholine, whose TRPES spectrum was recorded by Zhang and coworkers [Zhang, Y.; Deb, S.; Jónsson, H.; Weber, P. M. *J. Phys. Chem. Lett.* 2017, 8, 3740-3744]. This particular compound is notable for the fact that the photoelectron signal of its 3s state exhibits long-lived oscillations along the electron binding energy axis. In the work cited above, these oscillations were attributed to the oscillatory motions of a coherent vibrational wavepacket along the umbrella inversion coordinate of the amine group.

Our simulations reproduce the fine oscillatory structure of the photoelectron signal of the 3s state. This reflects positively on the accuracy of the ADC(2) method for the relevant excited- and ionized-state potential energy surfaces. At the same time, however, we find that these oscillations are best described as arising from vibrations along with the deformation modes of the six-membered ring, rather than the umbrella inversion coordinate. The above observation points to the need for a reinterpretation of the experimentally-observed TRPES spectrum.

We expect that our findings will be of particular interest to those computational chemists whose work concerns the relaxation processes of photoexcited molecules, as well as researchers in the field of time-resolved photoelectron spectroscopy. Quite recently, an Ultra-fast X-ray molecular scattering study captured the vibrational coherence to confirm the postulated mechanism in our study [78].

\* **2018** *Oscillatory Photoelectron Signal of N-Methylmorpholine as a Test Case for the Algebraic-Diagrammatic Construction Method of Second Order.*

**Raison Dsouza**, Xinxin Cheng, Zheng Li, R. J. Dwayne Miller, and Michał Andrzej Kochman

[The Journal of Physical Chemistry A 122.50 : 9688-9700.](#)

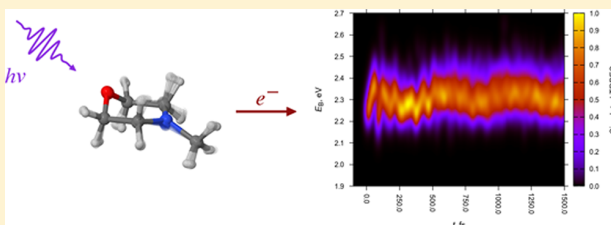
**Raison Dsouza** First Author Contribution

# Oscillatory Photoelectron Signal of *N*-Methylmorpholine as a Test Case for the Algebraic-Diagrammatic Construction Method of Second Order

Raison Dsouza,<sup>†</sup> Xinxin Cheng,<sup>†,‡</sup> Zheng Li,<sup>†</sup> R. J. Dwayne Miller,<sup>†,‡,¶</sup> and Michał Andrzej Kochman<sup>\*,§,||</sup><sup>†</sup>Max Planck Institute for the Structure and Dynamics of Matter, Bldg. 99 (CFEL), Luruper Chaussee 149, 22761 Hamburg, Germany<sup>‡</sup>Hamburg Centre for Ultrafast Imaging (CUI), Universität Hamburg, Luruper Chaussee 149, 22761 Hamburg, Germany<sup>¶</sup>Department of Chemistry and Physics, University of Toronto, 80 St. George Street, Toronto, Ontario M5S 3H6, Canada<sup>§</sup>Department of Physics, Chemistry and Biology (IFM), Linköping University, 581 83 Linköping, Sweden

## Supporting Information

**ABSTRACT:** Motivated by recent progress in the application of time-resolved photoelectron spectroscopy (TRPES) to molecular Rydberg states, we report herein a detailed assessment of the performance of the second-order algebraic diagrammatic construction (ADC(2)) method in the simulation of their TRPES spectra. As the test case, we employ the tertiary aliphatic amine *N*-methylmorpholine (NMM), which is notable for the fact that the signal of its 3s state exhibits long-lived oscillations along the electron binding energy axis. The relaxation process of photoexcited NMM is simulated via the Born–Oppenheimer molecular dynamics method, and the resulting TRPES spectrum is generated on the basis of ionization energies and approximate Dyson orbital norms calculated with the continuum orbital technique. On the whole, the simulated TRPES spectrum achieves satisfactory agreement with experiment, which suggests that the ADC(2) method provides a realistic description of the potential energy surfaces of the relevant excited and ionized states. In particular, the simulations reproduce the fine oscillatory structure of the signal of the 3s state, and provide evidence to the effect that it results from a coherent vibrational wavepacket evolving along the deformation modes of the six-membered ring. However, it is found that ADC(2) underestimates electron binding energies by up to a few tenths of an electronvolt. The case of NMM demonstrates the usefulness of ADC(2) as a tool to aid the interpretation of the TRPES spectra of large organic molecules.



## 1. INTRODUCTION

Although not usually thought of as standalone chromophores, aliphatic amine groups under gas-phase conditions give rise to transitions to a manifold of spatially diffuse Rydberg-type states, leading to a rich and complex photophysics that has been the subject of longstanding research.<sup>1–25</sup> Over the past decade, a leading role in the spectroscopic study of aliphatic amines has been played by time-resolved photoelectron spectroscopy<sup>4,26–32</sup> (TRPES), a pump–probe technique in which the pump pulse prepares the system and, after a time delay, the probe pulse ionizes it. Information on the time evolution of the system is extracted from the analysis of the photoelectron current, resolved with respect to time and electron binding energy.

The subpicosecond time resolution achieved by TRPES enables the monitoring of nonradiative transitions such as internal conversion and intersystem crossing. What is more, photoelectron spectroscopy has certain special advantages when it comes to Rydberg states. Namely, during photoionization from a Rydberg state, the kinetic energy of the nuclei remains largely unchanged and, consequently, the

spectral signals arising from these states are relatively narrow.<sup>33</sup> This is in contrast to the case of photoionization from valence excited states, which typically leads to broad spectral features. Furthermore, the binding energy of the Rydberg electron is sensitive to the structure and instantaneous conformation of the cationic core.<sup>11,33–35</sup> In several cases, this latter property has enabled the observation of the TRPES signatures of conformational transitions and coherent molecular vibrations,<sup>6,13,15,16,18,21,22,24,25</sup> and aliphatic amines are increasingly drawing attention as accessible model systems for the spectroscopic study of these phenomena. In recognition of these strengths, the term “Rydberg fingerprint spectroscopy” has been coined to describe applications of photoelectron spectroscopy to molecular Rydberg states.<sup>11,33–35</sup>

In parallel to the experimental work, considerable theoretical efforts have been devoted to the interpretation of TRPES spectra of aliphatic amines and related compounds whose

**Received:** October 21, 2018

**Revised:** November 26, 2018

**Published:** November 27, 2018

excited-state relaxation occurs in Rydberg states. Notably, Gudmundsdóttir and co-workers<sup>36</sup> developed a procedure for the treatment of the electronic structures of such states within the framework of the  $\Delta$  self-consistent field ( $\Delta$ SCF) method employing density functional theory with the imposition of self-interaction corrections<sup>37</sup> (DFT-SIC). The method of Gudmundsdóttir et al. has subsequently been applied to calculate the electronic excitation spectra and electron binding energies of a number of aliphatic amines and their clusters.<sup>16–18,21,22,24,25</sup> What is more, several studies have reported coupled cluster calculations of excited and ionized states of compounds of this class.<sup>19–23</sup>

A common limitation of previous studies of aliphatic amines is that electron binding energies were calculated only at a small number of fixed molecular geometries, or at most along a predefined relaxation path in the course of a potential energy surface scan. Because TRPES is, by definition, a temporally resolved technique, it is desirable to improve on this static picture by conducting dynamical (i.e., time-resolved) simulations of the relaxation dynamics and the resulting TRPES spectrum. Aside from testing the predictive power of the underlying theory, the motivation for such an undertaking is that TRPES provides only an indirect insight into the motions of nuclei. Computer simulations, on the other hand, are capable of drawing a direct connection between the observed spectral features and the dynamics of the molecule.

As a first step in the exploration of the TRPES spectroscopy of aliphatic amines with the use of dynamical simulations, the present paper investigates the accuracy of the second-order algebraic diagrammatic construction (ADC(2)) method<sup>38,39</sup> when applied to these systems. Among the excited-state electronic structure methods that could potentially be used in dynamical simulations, ADC(2) stands out for its combination of reasonable accuracy with good numerical stability and low computational cost. It should be pointed out here the idea of employing ADC(2) for the purpose of simulating photoelectron spectra is not new. Previously, Neville et al.<sup>40</sup> simulated the relaxation of photoexcited ethylene with the use of the *ab initio* multiple spawning (AIMS) method, treating its electronic structure at the multireference first-order configuration interaction (MR-FOCI) level, and subsequently used ADC(2) in order to calculate the resulting TRPES spectrum. In the present study, however, the ADC(2) method takes center stage, and it is used both in the calculation of the TRPES spectrum and in the simulation of the underlying relaxation dynamics. Because the TRPES spectrum is sensitive to the topographies of both the excited- and ionized-state potential energy surfaces, its calculation represents a very stringent test of the method.

The test case for the purposes of the present study is the tertiary aliphatic amine *N*-methylmorpholine (NMM; see Figure 1 for molecular structure). The relaxation dynamics of NMM was recently investigated with the use of TRPES by Zhang and co-workers<sup>24,25</sup> in the course of a systematic research program on aliphatic amines by the Weber group. This particular compound is noteworthy for the fact that the TRPES signal arising from its 3s state (which corresponds to the  $S_1$  adiabatic state) exhibits long-lived oscillations along the binding energy axis with a period of 650 fs<sup>24,25</sup> (see Figure 8c later in the present paper). On the basis of static calculations at the level of  $\Delta$ SCF, Zhang et al. attributed these oscillations to a coherent vibrational wavepacket evolving along the nitrogen umbrella inversion mode.<sup>24,25</sup> What is more, Zhang et al.<sup>24</sup>

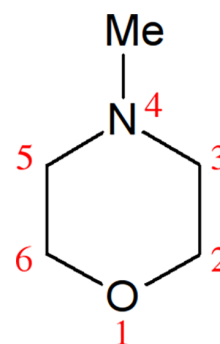


Figure 1. Molecular structure of NMM.

modeled the relaxation process of photoexcited NMM by means of molecular dynamics simulations. However, in those simulations, the nuclear dynamics was actually propagated on the potential energy surface of the ground electronic state ( $D_0$ ) of the  $NMM^+$  radical cation, rather than that of the  $S_1$  ( $3s$ ) state of the neutral molecule, which seems an overly severe approximation. What is more, no attempt was made to calculate the time evolution of the spectrum on the basis of the simulated dynamics.

From the standpoint of the present study, the challenge is to see whether dynamical simulations based on the ADC(2) method can reproduce, and thereby explain, the fine oscillatory structure of the signal of the  $S_1$  ( $3s$ ) state. As we shall see later in this paper, that is indeed the case. However, according to our simulations, the oscillations are actually caused by a coherent wavepacket moving along the deformation modes of the six-membered ring.

The rest of this paper is organized as follows. First, we outline the simulation methodology that was employed to simulate the TRPES spectrum of NMM. We then review the results of the static calculations, including equilibrium molecular geometries and the topographies of the relevant potential energy surfaces. We then move on to discuss the relaxation dynamics of photoexcited NMM. Finally, we present the resulting TRPES spectrum and tie in the emergent oscillations with the vibrational modes of the molecule.

## 2. COMPUTATIONAL DETAILS

The present simulations aimed to model the experiments reported by Zhang and co-workers,<sup>24</sup> whereby NMM was excited at a wavelength of 226 nm, populating the  $S_1$  ( $3s$ ) state. The subsequent relaxation dynamics was simulated with the use of Born–Oppenheimer molecular dynamics (BOMD). Finally, the resulting trajectories were utilized as the basis for the calculation of the TRPES.

**2.1. Electronic Structure Methods.** The electronic structure of NMM was treated with the use of the Møller–Plesset perturbation method (MP2) for the singlet ground state in combination with ADC(2) for the excited states. In what follows, we will collectively refer to this combination of methods as MP2/ADC(2). For the sake of brevity, the discussion of the level of accuracy achieved by MP2/ADC(2) for the relevant excited and ionized states of NMM, as well as the analysis of basis set size effects, are relegated to the Supporting Information.

In all calculations, a custom basis set was applied that was generated from the standard aug-cc-pVDZ basis set<sup>41</sup> by deleting the diffuse d subshell on the heavy atoms, as well as

the diffuse p subshell on the hydrogens. Thus, the diffuse functions retained in the basis set were the diffuse s and p functions on the heavy atoms, and the diffuse s functions on the hydrogens. In what follows, this basis set will be referred to as the r-aug-cc-pVDZ (“reduced aug-cc-pVDZ”) basis set. This reduction of basis set size allows substantial savings of CPU time relative to the full aug-cc-pVDZ basis.

On the subject of basis set construction, it is worth referencing the work of Papajak and co-workers,<sup>42</sup> who generated and tested a series of so-called calendar basis sets derived via the reduction of the standard aug-cc-pVnZ basis sets. In these calendar basis sets, no diffuse functions are placed on hydrogen atoms. We believe that for an accurate description of the Rydberg states of a hydrogen-rich molecule such as NMM, at least the diffuse s functions should be retained on hydrogens. For this reason, we did not attempt to use the calendar basis sets in the present study. However, there is no reason to question the applicability of the calendar basis sets in many other contexts.

The calculation of the TRPES spectrum requires a means to calculate the target ionized states, as well as Dyson orbitals for ionization. To this end, we employed again the MP2/ADC(2) method, but now in combination with the continuum orbital technique of Stanton and Gauss.<sup>43</sup> The continuum orbital technique takes advantage of the fact that ionization can be viewed as a vertical excitation process in which an electron is promoted from an occupied orbital localized on the molecule into a virtual continuum orbital. In practice, the continuum orbital is represented by an extremely diffuse (low-exponent) s-type orbital. Then, the vertical ionization energy (VIP) is simply equal to the calculated vertical excitation energy.

We note here that the continuum orbital method has some advantages and disadvantages relative to the standard approach, in which the electronic states of the ionized species are described with the use of ( $N-1$ )-electron wave functions,  $N$  being the number of electrons of the neutral molecule. When the continuum orbital technique is applied in combination with the MP2/ADC(2) method, qualitatively accurate results can be expected only for ionized states dominated by single excitations from the reference determinant of the neutral molecule. In this regard, the standard approach, based on the reference determinant of the ionized species, is more general.

Fortunately, the coupled cluster calculations reported in the [Supporting Information](#) indicate that the two relevant ionized states of NMM (namely,  $D_0$  and  $D_1$ ) are dominated by single excitations from the reference determinant of the neutral molecule. As such, they fall into the category of states that can be described with the use of the continuum orbital method in combination with MP2/ADC(2).

An advantage of the continuum orbital method over the standard approach is that in the former, all ionized states are treated on an equal footing. In the standard approach, however, the ground electronic state of the ionized species is typically treated on a different footing to its excited electronic states. For example, in the standard approach, the ground state of the ionized species might be treated with the use of MP2 in combination with an unrestricted Hartree–Fock reference determinant, whereas its excited states would be treated with ADC(2). As a consequence, the standard approach is expected to be problematic when the ground state of the ionized species is degenerate, or near-degenerate with another ionized state. Such a situation does not arise in the case of the  $\text{NMM}^+$

radical cation, whose  $D_0$  state is well separated in energy from the  $D_1$  state and all higher ionized states. However, in aliphatic amines that possess two or more nitrogen atoms, such as  $N,N,N',N'$ -tetramethylethylenediamine<sup>16,18</sup> (TMEDA) and  $N,N'$ -dimethylpiperazine<sup>15,22</sup> (DMP), the lowest few ionized states are expected to be narrowly spaced. Therefore, with a view to possible future work on these systems, we elected to use the continuum orbital method.

The MP2/ADC(2) calculations were performed within the computational chemistry software package Turbomole, version 6.3.1,<sup>44</sup> taking advantage of the frozen core and resolution of the identity<sup>45–48</sup> approximations. The default auxiliary basis set for aug-cc-pVDZ<sup>49</sup> was used as the auxiliary basis set for the r-aug-cc-pVDZ basis set. Due to the extremely diffuse nature of the continuum orbital, the calculated VIPs are not sensitive to the choice of its central point. In the present implementation, it was arbitrarily placed on the nitrogen atom. Integrals between the Gaussian primitive making up the continuum orbital, and the other basis functions, were neglected as per program defaults.

**2.2. Born–Oppenheimer Molecular Dynamics.** The relaxation dynamics of NMM was simulated by propagating BOMD trajectories on the potential energy surface of the  $S_1$  adiabatic state. In this approach, the nuclear wavepacket of the system is represented by a so-called “swarm”, or ensemble, of mutually independent semiclassical trajectories. In each trajectory, the nuclei are described using classical mechanics, while the electrons are treated quantum-mechanically. The above model of nuclear dynamics is expected to qualitatively capture the coherent vibrational motions triggered by photoexcitation of NMM. The restriction that the system is confined to the  $S_1$  state is justified by the fact that the experimentally observed TRPES spectrum reported by Zhang and co-workers<sup>24</sup> exhibits only a single band that originates from the  $3s$  state, which corresponds to the  $S_1$  adiabatic state.

The initial conditions for the BOMD simulations were generated by sampling phase space points (which is to say, sets of nuclear positions and velocities) from the ground-state harmonic-oscillator Wigner distribution of the dominant ground-state conformer of NMM (i.e., the chair-equatorial conformer; see [section 3.1.1](#)). A total of 38 phase space points were sampled in this manner, and each was used as the starting point for the propagation of a single trajectory. Afterward, the nuclear dynamics was propagated using the velocity Verlet integrator with a time step of 0.5 fs, for a time period of 1.6 ps.

As pointed out in [refs 50 and 51](#), semiclassical simulations of hydrogen-rich molecules are susceptible to a physically unrealistic leakage of zero-point energy from the stretching modes of bonds between hydrogens and heavy atoms to other vibrational modes. In order to alleviate this problem, the 11 highest vibrational modes, which correspond to C–H stretching modes, were frozen when the Wigner distribution was generated.

The equilibrium geometries on the ground- and excited-state potential energy surfaces of NMM, as well as the BOMD trajectories, were described in terms of a set of parameters whose definitions we will now provide. As illustrated in [Figure 2](#), in order to monitor the geometry of the nitrogen atom ( $N_4$ ), we defined  $\alpha$  as the angle formed by the bond  $N_4$ – $C(\text{Me})$ , where  $C(\text{Me})$  is the methyl group carbon atom, and the plane containing atoms  $C_3$ ,  $N_4$ , and  $C_5$ .

The conformation of the six-membered ring was characterized with the use of the puckering coordinates  $\theta_0$ ,  $\theta_1$ , and  $\theta_2$

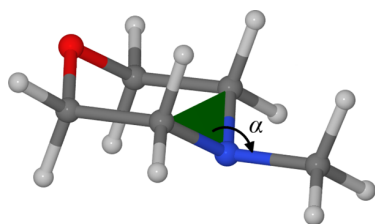


Figure 2. Definition of the angle  $\alpha$ .

introduced by Hill and Reilly.<sup>52</sup> Furthermore, during the analysis of the BOMD trajectories, we found it useful to monitor how much the geometry of the six-membered ring deviates from a chair conformation. To this end, we defined  $\Delta$  as the distance between the current molecular geometry, and an ideal  ${}^4C_1$  or  ${}^1C_4$  conformation, in the three-dimensional space spanned by the parameters  $\theta_0$ ,  $\theta_1$ , and  $\theta_2$ . For a more detailed explanation, the reader is referred to the [Supporting Information](#).

**2.3. Simulation of Time-Resolved Photoelectron Spectrum.** Having completed the BOMD simulations, we proceeded to calculate the TRPES spectrum using the algorithm formulated by Arbelo-González and co-workers<sup>53</sup> (see also literature cited therein). This method takes as input the set of  $N_{\text{trajs}}$  semiclassical trajectories, which will be denoted  $\{\mathbf{R}_i(t)\}$ . As shown schematically in [Figure 3](#), the TRPES spectrum is considered to arise from ionization from the current state along a given trajectory, denoted as the  $n$ -th state, into the electronic states of the cation, which are labeled by the

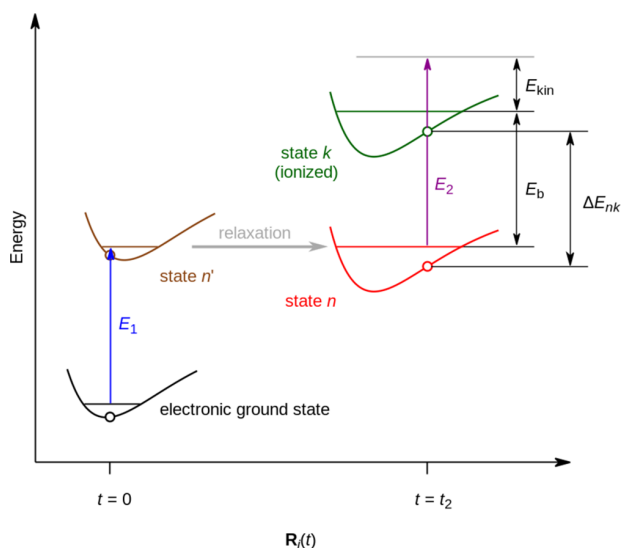


Figure 3. Definition of the quantities used in the calculation of the photoelectron spectrum. At time  $t = 0$ , the probe pulse with photon energy  $E_1$  excites the system to state  $n'$ , following which it is allowed to relax until  $t = t_2$ . By  $t = t_2$ , the system exists in electronic state  $n$ , which may in general be a different adiabatic state than  $n'$ . At  $t = t_2$ , the system is subjected to the probe pulse of photon energy  $E_2$ , which detaches a photoelectron with kinetic energy  $E_{\text{kin}}$ , leaving behind a ionized species in electronic state  $k$ . The approximation that the probe pulse does not alter the kinetic energy of the nuclei leads to the result that the electron binding energy  $E_b = E_2 - E_{\text{kin}}$  is equal to the vertical energy difference between states  $k$  and  $n$ .

index  $k$ . Then, the photoelectron intensity resolved with respect to time and electron binding energy is calculated as

$$\Gamma(E_b, t) = \sum_k \frac{1}{N_{\text{trajs}}} \sum_{i=1}^{N_{\text{trajs}}} \sigma_{nk}(\mathbf{R}_i(t)) w_s(E_b, \Delta E_{nk}(\mathbf{R}_i(t))) \quad (1)$$

As per the usual convention, the electron binding energy  $E_b = E_2 - E_{\text{kin}}$  is defined as the difference between the photon energy of the probe pulse ( $E_2$ ), and the kinetic energy of the electron being ejected from the molecule ( $E_{\text{kin}}$ ). Anticipating the results of [section 3.1.3](#), we note here that the TRPES spectrum of NMM in the electron binding energy range of interest arises predominantly from the  $S_1(3s) \rightarrow D_0$  photoionization process. Thus, in the present case, the initially excited state  $n'$  as well as the current state  $n$  always correspond to the  $S_1(3s)$  state, whereas the final state  $k$  is always the  $D_0$  state of the cation.

The quantity  $\sigma_{nk}(\mathbf{R}_i(t))$  which appears in [eq 1](#) is the photoionization cross section for the  $n \rightarrow k$  ionization process. Following an approximation suggested in [ref 53](#), we assume that  $\sigma_{nk}(\mathbf{R}_i(t))$  is proportional to the squared norm of the Dyson orbital associated with the  $n \rightarrow k$  ionization process and, furthermore, that the constant of proportionality ( $C$ ) is independent of any other characteristics of this particular process:

$$\sigma_{nk}(\mathbf{R}_i(t)) = C \|\phi_{nk}^D(\mathbf{r}_N; \mathbf{R}_i(t))\|^2 \quad (2)$$

Here,  $\phi_{nk}^D(\mathbf{r}_N)$  is the Dyson orbital for the  $n \rightarrow k$  ionization. The calculation of the Dyson orbital with the use of the ADC(2) method will be outlined later on.

$w_s$ , in turn, is best described as a signal shape function; its purpose is to account for the dependence of the kinetic energy of the ejected electron ( $E_{\text{kin}}$ ) on the photon energy of the probe pulse ( $E_2$ ). Unfortunately, no universally applicable expression for  $w_s$  exists and, in practice, it is necessary to construct an approximation on the basis of assumptions of the interaction of the probe pulse with the target molecule. In the case of ionization from Rydberg states, the probe pulse does not impart significant vibrational excitation on the target molecule,<sup>33</sup> and the resulting TRPES bands are fairly narrow, usually not exceeding 0.2 eV in full width at half-maximum (fwhm). This observation suggests that a sharp  $w_s$  function should be chosen for the purpose of modeling the TRPES spectrum of NMM. Accordingly, we imposed the approximation that the nuclear kinetic energy remains constant in the course of photoionization. As can be seen from [Figure 3](#), the electron binding energy is then equal to the vertical energy difference ( $\Delta E_{nk}$ ) between the initial ( $n$ ) and final ( $k$ ) states in the photoionization:

$$E_b = E_2 - E_{\text{kin}} = \Delta E_{nk} \quad (3)$$

Furthermore, we note that a continuous line shape function is desirable, as this simplifies the numerical analysis of the resulting spectrum. For these reasons, we decided to take  $w_s$  as a Gaussian function of the difference between  $E_b$  and  $\Delta E_{nk}$ :

$$w_s(E_b, \Delta E_{nk}(\mathbf{R}(t))) = \frac{2^{1/2}}{\pi^{1/2} \eta} \exp\left(-\frac{2(E_b - \Delta E_{nk}(\mathbf{R}(t)))^2}{\eta^2}\right) \quad (4)$$

The broadening parameter was set to  $\eta = 0.1$  eV. It must be emphasized that the above choice of the form of  $w_s$  represents

**Table 1.** Characterization of the Equilibrium Geometries of NMM on the  $S_0$  and  $S_1$  Adiabatic States: Relative Energies ( $E$ ), Hill–Reilly Conformational Parameters ( $\theta_0$ ,  $\theta_1$ , and  $\theta_2$ ), and Values of the Methyl Wagging Angle ( $\alpha$ )<sup>a</sup>

| electronic state | equilibrium geometry    | $E$ , eV | ring conformation           | $\theta_0$ , deg | $\theta_1$ , deg | $\theta_2$ , deg | $\alpha$ , deg |
|------------------|-------------------------|----------|-----------------------------|------------------|------------------|------------------|----------------|
| $S_0$            | chair equatorial        | 0        | <sup>4</sup> C <sub>1</sub> | 34.4             | 34.7             | 34.4             | 127.7          |
|                  | chair axial             | 0.208    | <sup>4</sup> C <sub>1</sub> | 34.6             | 26.9             | 34.6             | 227.7          |
|                  | twisted boat equatorial | 0.366    | <sup>1</sup> S <sub>5</sub> | −60.6            | 61.2             | 1.2              | 129.9          |
|                  | twisted boat axial      | 0.448    | <sup>1</sup> S <sub>5</sub> | −60.2            | 55.7             | −2.5             | 228.6          |
| $S_1$ (3s)       | chair                   | 4.269    | <sup>4</sup> C <sub>1</sub> | 35.8             | 33.9             | 35.8             | 195.4          |
|                  | twisted boat            | 4.458    | <sup>1</sup> S <sub>5</sub> | −65.4            | 40.0             | 9.1              | 178.7          |

<sup>a</sup>The energies are stated relative to the chair-equatorial conformer on the  $S_0$  state, and include zero-point vibrational corrections. The ring conformation is described using the IUPAC notation.<sup>57</sup>

an *ad hoc* approximation tailored to the specific problem at hand.

The Dyson orbital for ionization  $\phi^D(\mathbf{r})$  is defined as the overlap of the  $N$ -electron electronic wave function  $\Psi^N$  of the original system, and the  $(N-1)$ -electron wave function  $\Psi^{N-1}$  of the resulting ionized molecule:

$$\phi^D(\mathbf{r}_N) = \sqrt{N} \int \Psi^N(\mathbf{r}_1, \dots, \mathbf{r}_N) \Psi^{N-1}(\mathbf{r}_1, \dots, \mathbf{r}_{N-1}) \, d\mathbf{r}_1 \dots d\mathbf{r}_{N-1} \quad (5)$$

In the present case,  $\Psi^N$  represents an excited state of the neutral molecule and  $\Psi^{N-1}$  is a ionized state. Either state is calculated with the use of the MP2/ADC(2) method.

Within the formalism of the second quantization,  $\phi^D(\mathbf{r}_N)$  may be expressed in terms of a linear combination of the canonical Hartree–Fock orbitals  $\{\phi_p\}$  of the neutral molecule:

$$\phi^D = \sum_p \langle \Psi^{N-1} | \hat{p} | \Psi^N \rangle \phi_p \quad (6)$$

A complication arises because ionization is being modeled via the continuum orbital technique, in which the electronic wave functions of the original system and the ionized molecule formally describe the same number of electrons. This problem was circumvented by applying an approximation introduced by Neville et al.<sup>40</sup> Let  $\bar{\Psi}^N$  denote the  $N$ -electron ADC(2) wave function describing the ionized molecule. The  $(N-1)$ -electron wave function  $\Psi^{N-1}$  is obtained from  $\bar{\Psi}^N$  by acting on the latter with the operator  $\hat{k}$  annihilating an electron from the continuum orbital:

$$|\Psi^{N-1}\rangle = \hat{k}|\bar{\Psi}^N\rangle \quad (7)$$

The above step can be justified by the fact that the ADC(2) wave function  $|\bar{\Psi}^N\rangle$  is dominated by singly excited configurations in which an electron is promoted from an occupied orbital localized on the molecule into the virtual continuum orbital. Informally speaking, the role of the operator  $\hat{k}$  is to empty the continuum orbital. Thus, the formula for the Dyson orbital can be written out as

$$\phi^D = \sum_{p \neq k} \langle \bar{\Psi}^N | \hat{k}^\dagger \hat{p} | \Psi^N \rangle \phi_p = \sum_{p \neq k} \rho_{kp} \phi_p \quad (8)$$

where  $\rho$  is the transition density matrix (in molecular orbital basis) between states  $\bar{\Psi}^N$  and  $\Psi^N$ .

For the purpose of calculating the transition density matrix, the ADC(2) excited-state wave function  $\Psi^N$  is approximated as a wave function of the configuration interaction singles (CIS) type:

$$|\Psi^N\rangle = \sum_{i,a} R_i^a |\Phi_i^a\rangle \quad \text{where} \quad |\Phi_i^a\rangle = \hat{a}^\dagger \hat{i} |\Phi_0\rangle \quad (9)$$

Here,  $\Phi_0$  is the RHF reference determinant, and  $R_i^a$  are elements of the Jacobian eigenvector corresponding to single excitations. An analogous approximation is used for the ADC(2) ionized-state wave function,  $\bar{\Psi}^N$ .

The singles excitations part of the Jacobian eigenvector for each state was extracted from Turbomole output files with the use of the program bin2matrix distributed as part of the simulation package Newton-X.<sup>54–56</sup> Subsequently, it was rescaled so as to ensure that the resulting  $\Psi^N$  and  $\bar{\Psi}^N$  were each normalized to unity.

At the postprocessing stage, the raw simulated spectrum obtained from eq 1 was subjected to a Gaussian blur in the time domain with a standard deviation of  $\sigma = 25$  fs. The motivation for applying the blur was to account for the various effects that limit the time resolution of the experiment. For comparison, the raw simulated spectrum with no blur is shown in the Supporting Information.

### 3. RESULTS AND DISCUSSION

**3.1. Static Calculations.** **3.1.1. Ground-State Conformers.** We begin the discussion of the simulation results by examining the conformational preference of NMM in its electronic ground state ( $S_0$ ). A conformation search reveals the existence of four minima on the potential energy surface of the  $S_0$  state. As set out in Table 1, the four conformers differ from one another mainly in terms of the geometry of the six-membered ring (chair- or twisted boat-like), and the orientation of the methyl group (axial or equatorial). In order of increasing energy, these are the chair equatorial, chair axial, twisted boat equatorial, and twisted boat axial conformers. A common feature of all four conformers is the pyramidalization of the nitrogen atom N4. Out of the four, the first three have been reported previously by Zhang et al.<sup>24</sup> The molecular geometry of the chair-equatorial conformer is illustrated in Figure 4a, whereas the geometries of the higher-energy conformers are given in the Supporting Information.

In agreement with the findings of Zhang et al.,<sup>24</sup> we identify the chair equatorial conformation as the global minimum on the  $S_0$  state. The second-lowest conformer, the chair axial, lies 0.208 eV higher in energy (energy difference corrected for zero-point vibrational energies). As a consequence, at normal temperatures the chair equatorial conformer is by far the predominant form of NMM in the gas phase. Accordingly, in what follows, we restrict ourselves to considering the relaxation process of the chair equatorial conformer and its contribution

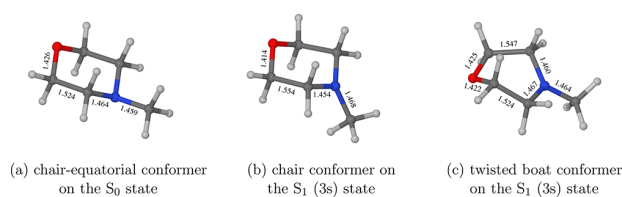


**Figure 4.** Key equilibrium geometries on the  $S_0$  and  $S_1$  ( $3s$ ) potential energy surfaces of NMM. Selected bond lengths are indicated in units of Å.

to the TRPES spectrum. The contributions of the minority conformers are neglected as insignificant.

**3.1.2. Excited Electronic States.** The vertical excitation spectrum of the chair-equatorial conformer is summarized in the upper part of Table 2. The lowest vertical transition is into

**Table 2. (Top) Vertical Excitation Spectrum of the Chair-Equatorial Conformer of NMM As Calculated at the MP2/ADC(2)/r-aug-cc-pVDZ Level of Theory (Vertical Excitation Energies ( $\Delta E$ ) and Associated Oscillator Strengths ( $f$ )); (Bottom) Vertical Ionization Spectrum (Vertical Ionization Potentials (VIPs))**

| Excited States   |                 |        |
|------------------|-----------------|--------|
| state            | $\Delta E$ , eV | $f$    |
| $S_1$ ( $3s$ )   | 5.261           | 0.0145 |
| $S_2$ ( $3p_z$ ) | 5.703           | 0.0877 |
| $S_3$ ( $3p_x$ ) | 5.729           | 0.0051 |
| $S_4$ ( $3p_y$ ) | 5.900           | 0.0074 |
| Ionized States   |                 |        |
| state            | VIP, eV         |        |
| $D_0$            | 7.494           |        |
| $D_1$            | 8.272           |        |

the  $3s$  state, which is dominated by the excitation of an electron from the occupied orbital corresponding to the nitrogen lone electron pair into a spatially diffuse  $3s$ -type virtual orbital which envelops the molecule. At somewhat higher energies, a trio of closely spaced  $3p$  states is detected, each of which arises from the excitation of an electron from the nitrogen lone electron pair orbital into a diffuse  $3p$ -type virtual orbital.

Further diffuse states are found above the  $3p$  states. We forego a discussion of their properties, as at least some of these states are, presumably, poorly described by a basis set including only a single layer of diffuse functions, such as the r-aug-cc-pVDZ basis set. In any case, these higher states are not involved in the photophysics of NMM excited initially into the  $S_1$  ( $3s$ ) state.

**3.1.3. Ionized States.** The ionized states of NMM are characterized in the lower part of Table 2. Note that the values of the vertical ionization potential (VIP) listed therein refer to ionization from the ground electronic state ( $S_0$ ), even though the TRPES spectrum of NMM arises from ionization from the  $S_1$  ( $3s$ ) state.

The ADC(2) calculation places the lowest vertical ionization potential (VIP) of NMM at 7.494 eV. The resulting electronic state  $D_0$  of the cation can be described as arising from the removal of an electron from the nitrogen lone pair orbital (denoted  $n_N$ ) of the neutral molecule. As such, the predominant electronic configuration may be written out in

terms of the orbitals of the neutral molecule as [closed shells] $n_N^1$ . It differs by exactly one orbital, namely, the  $3s$  orbital, from the predominant electronic configuration of the  $S_1$  ( $3s$ ) state, which is [closed shells] $n_N^1 3s^1$ . On the basis of the first ionization rule formulated in ref 53, it follows that the  $S_1$  ( $3s$ )  $\rightarrow$   $D_0$  photoionization process is allowed, and the corresponding Dyson orbital consists mainly of the  $3s$ -like LUMO of the neutral molecule. In agreement with the above qualitative picture, the Dyson orbital obtained from eq 8 turns out to resemble the  $3s$  orbital (see Figure 5). Its norm takes a value of 0.995, very close to the maximum possible value of 1, which confirms that the  $S_1$  ( $3s$ )  $\rightarrow$   $D_0$  photoionization process is allowed.

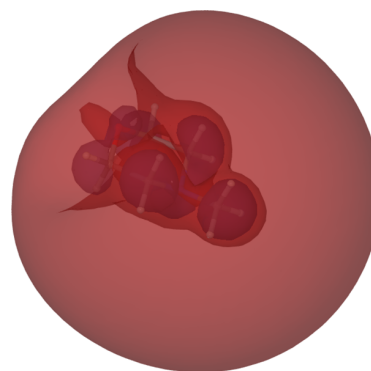


**Figure 5.** Dyson orbital for ionization from the  $S_1$  ( $3s$ ) state into the  $D_0$  state, at the ground-state equilibrium geometry of the former ( $S_0$ -min), plotted in the form of isosurfaces with isovalues of  $\pm 0.005 a_0^{-3/2}$ .

In turn, the second-lowest VIP of NMM takes a value of 8.272 eV and corresponds to ionization into the  $D_1$  state. The inspection of the right Jacobian eigenvector for that state indicates that it arises from the removal of an electron from an oxygen lone pair orbital of the neutral molecule. The fact that  $D_1$  and all higher electronic states of the  $NMM^+$  radical cation are well separated in energy from the  $D_0$  state energy means that photoionization into these states does not contribute to the TRPES spectrum of NMM in the electron binding energy range of interest. Therefore, when simulating the TRPES spectrum, we take into account only the  $S_1$  ( $3s$ )  $\rightarrow$   $D_0$  photoionization process. As a side note, the  $S_1$  ( $3s$ )  $\rightarrow$   $D_1$  ionization process is only very weakly allowed, as the norm of the corresponding Dyson orbital takes a low value of 0.081. This observation provides an additional justification for neglecting ionization into the  $D_1$  state.

**3.1.4. Excited-State Conformers.** Following photoexcitation at 226 nm, NMM persists in the  $S_1$  ( $3s$ ) state for at least several picoseconds,<sup>24</sup> which implies the existence of a minimum on the potential energy surface of that state. As a matter of fact, two such minima are found, and their geometries are characterized in the lower part of Table 1. The first, illustrated in Figure 4b, features a chair conformation of the six-membered ring, and a near-planar geometry of the nitrogen atom. At the second minimum, shown in Figure 4c, the six-membered ring adopts a twisted boat geometry, and the nitrogen atom is, again, near-planar. The roles of the two minima on the  $S_1$  ( $3s$ ) state will be discussed in the following section, which deals with the simulated relaxation dynamics of NMM.

**3.1.5. Relationship between Electron Binding Energy and Molecular Geometry.** Although the simulation of the TRPES spectrum of NMM requires the propagation of nuclear dynamics, already static calculations are able to identify the nuclear motions capable of modulating the electron binding energy. As noted in section 2.3, in the present study the electron binding energy was approximated as the vertical energy difference between the initial adiabatic state of the neutral molecule, and the final adiabatic state of the cation. Subsequently, in section 3.1.3, it was demonstrated that the only significant contribution to the TRPES spectrum in the energy range of interest is from the  $S_1(3s) \rightarrow D_0$  photoionization process. It follows that the electron binding energy along a nuclear trajectory  $\mathbf{R}(t)$  is given by

$$E_b(\mathbf{R}(t)) = E[D_0](\mathbf{R}(t)) - E[S_1](\mathbf{R}(t)) \quad (10)$$

where  $E[D_0](\mathbf{R}(t))$  and  $E[S_1](\mathbf{R}(t))$  are the energies of the respective adiabatic states. By using the chain rule, we may express the time-derivative of  $E_b$  as

$$\begin{aligned} \frac{d}{dt}E_b(\mathbf{R}(t)) &= \frac{d}{dt}E[D_0](\mathbf{R}(t)) - \frac{d}{dt}E[S_1](\mathbf{R}(t)) \\ &= (\nabla_{\mathbf{R}}E[D_0] - \nabla_{\mathbf{R}}E[S_1]) \cdot \dot{\mathbf{R}} \end{aligned} \quad (11)$$

In other words, changes in the electron binding energy along a simulated trajectory are caused by nuclear motions parallel, or antiparallel, to the gradient difference vector between the states  $D_0$  and  $S_1$ .

The gradient difference vector itself depends on the molecular geometry. While it would be impracticable to evaluate this vector for all nuclear geometries accessed during the relaxation dynamics, a useful qualitative picture may nevertheless be obtained by calculating it at a number of representative molecular geometries. We chose for this purpose the chair-equatorial equilibrium geometry on the  $S_0$  state, and the two equilibrium geometries that exist on the  $S_1(3s)$  state. The gradient difference vector at the chair-equatorial equilibrium geometry on the  $S_0$  state will indicate the motions that affect in the binding energy at the earliest stage of the simulated dynamics, when the molecule relaxes away from the Franck–Condon geometry. Subsequently, the molecule will undergo vibrations in the potential energy basin around a minimum on the  $S_1(3s)$  state. The gradient difference vector at the minimum on the  $S_1(3s)$  state will show the motions that influence the binding energy at that later stage.

The resulting gradient difference vectors are shown in Figure 6. We note, first, that the electron binding energy turns out to be quite sensitive to the geometry of the six-membered ring. This point is evidenced by the fact that at each of the geometries considered here, the gradient difference vector has fairly large components on oxygen atom O1 and the carbon atoms belonging to the six-membered ring. (Presumably, the

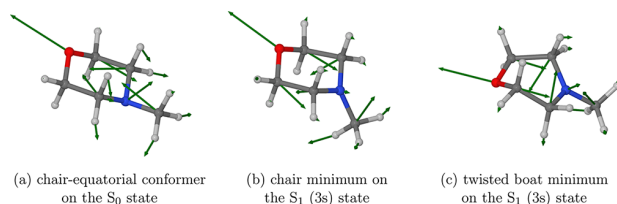


**Figure 6.** Visual representation of the vector  $\nabla_{\mathbf{R}}E[D_0] - \nabla_{\mathbf{R}}E[S_1]$  at selected equilibrium geometries of NMM.

same holds true throughout most of the volume of configuration space accessed by the NMM molecule during its relaxation dynamics.) In qualitative terms, the vector corresponds to a combination of the compression or elongation of the bonds forming part of the six-membered ring, and the deformation modes (bending, torsion) of that ring. As a consequence of the above, the ring modes of the equilibrium geometries on the  $S_1(3s)$  state are capable of modulating the electron binding energy, and we will return to this point when discussing the simulated TRPES spectrum in section 3.2.2.

However, of the three geometries considered here, only at the chair-equatorial geometry on  $S_0$  is there an appreciably large component of the gradient difference vector on the nitrogen atom. At either of the equilibrium geometries on the  $S_1(3s)$  state, the gradient difference vector has only a very small component on the nitrogen atom. These observations suggest that during the earliest stage of the relaxation dynamics following the initial photoexcitation, the planarization of the nitrogen atom N4 will lead to an increase the electron binding energy. However, once the molecule has reached the vicinity of a minimum on the  $S_1(3s)$  state, continuing vibrations along the nitrogen umbrella mode are not expected to be able to affect the electron-binding energy to a significant extent. This is because the gradient difference at either equilibrium geometry on the  $S_1(3s)$  state has only a small component on atom N4.

As a digression, we note that in the continuum orbital technique, the evaluation of the gradient of an ionized state (such as  $D_0$ ) is considerably more expensive in terms of computing time than the evaluation of the gradient of a low-lying excited state (such as the  $S_1(3s)$  state). This is because the ionized state is obtained as a high-energy excited state of the neutral system. The evaluation of the gradient of  $D_0$  involves three steps. First, a single-point MP2/ADC(2) calculation is performed in which a large number (typically, 20 to 30) excited states are computed. Then, the Jacobian eigenvector of each state is analyzed, and the ionized state, or states, are identified as those states that are dominated by single excitations into the continuum orbital. Finally, another single-point MP2/ADC(2) calculation must be performed, again with the inclusion of a large number of states, in order to calculate the gradient of the ionized state.

**3.2. Relaxation Dynamics.** **3.2.1. Evolution of Molecular Geometry.** Having characterized the underlying electronic states, we are now prepared to discuss the simulated relaxation dynamics of NMM photoexcited into the  $S_1(3s)$  state, and the resulting TRPES spectrum. In this section, we will concern ourselves with the motions of the nuclei. The time evolution of the angle  $\alpha$ , which is the angle formed by the N4–C(Me) bond and the plane defined by atoms C3, N4, and C5, along the ensemble of simulated trajectories is plotted in Figure 7a. Likewise, Figure 7b shows the deviation of the ring geometry from an ideal chair geometry as measured by the parameter  $\Delta$ . For either quantity, we additionally show the mean and the median from among the ensemble of simulated trajectories.

At the time of the initial photoexcitation ( $t = 0$ ), the ensemble of trajectories which represents the nuclear wavepacket is localized in a small region of configuration space near the equilibrium geometry of the chair equatorial conformer on the  $S_0$  state. As a consequence of the topography of the potential energy surface of the  $S_1(3s)$  state, immediately following photoexcitation, nitrogen atom N4 becomes subject

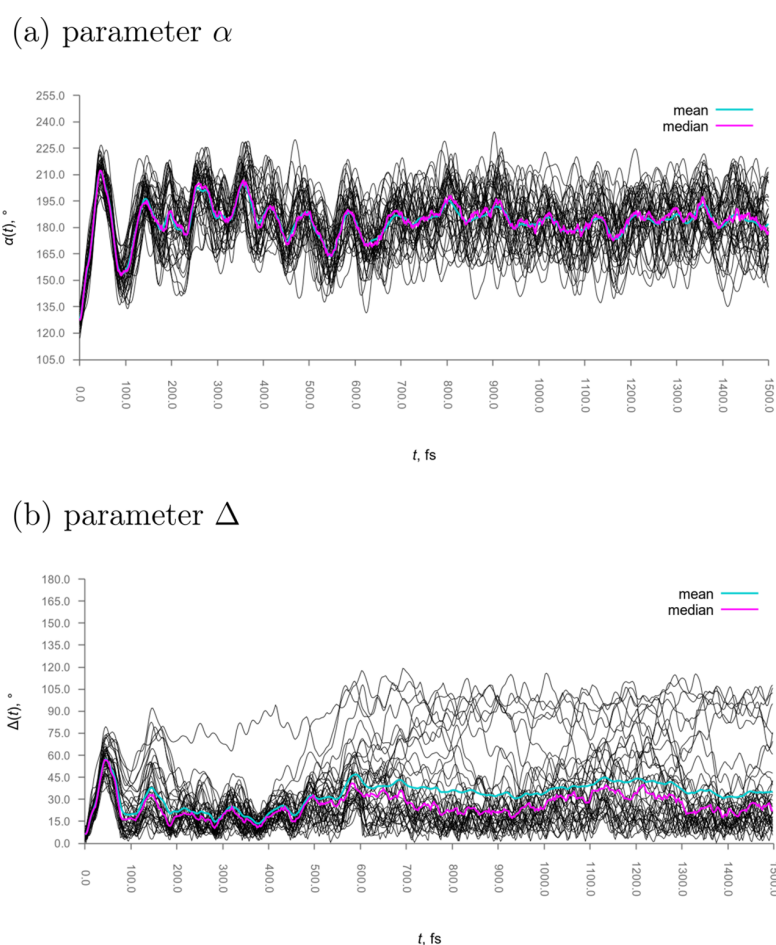


Figure 7. Time evolution of the angle  $\alpha$  and the parameter  $\Delta$  during the simulated relaxation dynamics of NMM.

to a strong force that acts to propel it toward a planar geometry. During the earliest stage of the ensuing relaxation process, atom N4 first planarizes and then goes on to undergo umbrella inversion; this is reflected by the mean value of  $\alpha$ , which initially increases rapidly, reaching a maximum of  $211^\circ$  at  $t = 45$  fs. At that point, the nitrogen atom is reflected back, and the mean value of  $\alpha$  begins to decrease again. Afterward, atom N4 settles into an oscillatory umbrella motion characterized by a period of around 90 fs. What is more, inspection of Figure 7a reveals another, slower component of the oscillations along the angle  $\alpha$ , with a period of roughly 500 fs. This low-frequency component arises from the wagging of the methyl group with atom N4 acting as the pivot.

During the first few hundreds of femtoseconds following the initial photoexcitation, oscillations along the angle  $\alpha$  in the individual trajectories exhibit a high degree of phase coherence, which manifests itself in the form of periodic oscillations in the mean and the median values of  $\alpha$  from among the ensemble of simulated trajectories. Gradually, however, the phase coherence is lost, until by around  $t = 1000$  fs the oscillations along  $\alpha$  appear to have dephased completely. From then on, the mean and the median values of  $\alpha$  undergo only minor fluctuations around  $180^\circ$ .

Simultaneously with the planarization and umbrella inversion of atom N4 during the initial 45 fs long time period following photoexcitation, the six-membered ring undergoes a deformation from a chairlike geometry ( ${}^4C_1$ ) to an envelope-

like geometry ( $E_1$ ). The departure from a chairlike geometry is reflected by a rapid increase of mean and median values of parameter  $\Delta$ . At roughly  $t = 45$  fs, the mean and median values of  $\Delta$  reach their respective maxima and then decrease again as the molecule begins to vibrate between chairlike and envelope-like geometries.

At later times, especially from around  $t = 500$  fs, some from among the simulated trajectories seemingly escape the potential energy well around the chair minimum on the  $S_1$  ( $3s$ ) state and adopt twisted boat-like geometries similar to the other minimum on the  $S_1$  ( $3s$ ) state, or other, deformed, ring geometries. The affected trajectories adopt high values of parameter  $\Delta$  (over  $60^\circ$ ), which is clearly seen in Figure 7b. The propensity of simulated trajectories to deviate from chairlike geometries may be in part due to an artificial leakage of zero-point energy from high-frequency vibrational modes, such as bond stretching and bending, to the low-frequency torsional modes that are associated with change of ring conformation. Though, as mentioned in section 2.2, we have attempted to mitigate this effect by freezing all C–H stretching modes when generating the Wigner distribution, it is possible that doing so did not completely eliminate the problem.

The escape of simulated trajectories from the potential energy well around the chair minimum on the  $S_1$  ( $3s$ ) state manifests itself as a gradual increase with time in the mean value of the parameter  $\Delta$ . The median value of  $\Delta$  is less susceptible to this possibly artificial phenomenon (as a rule,

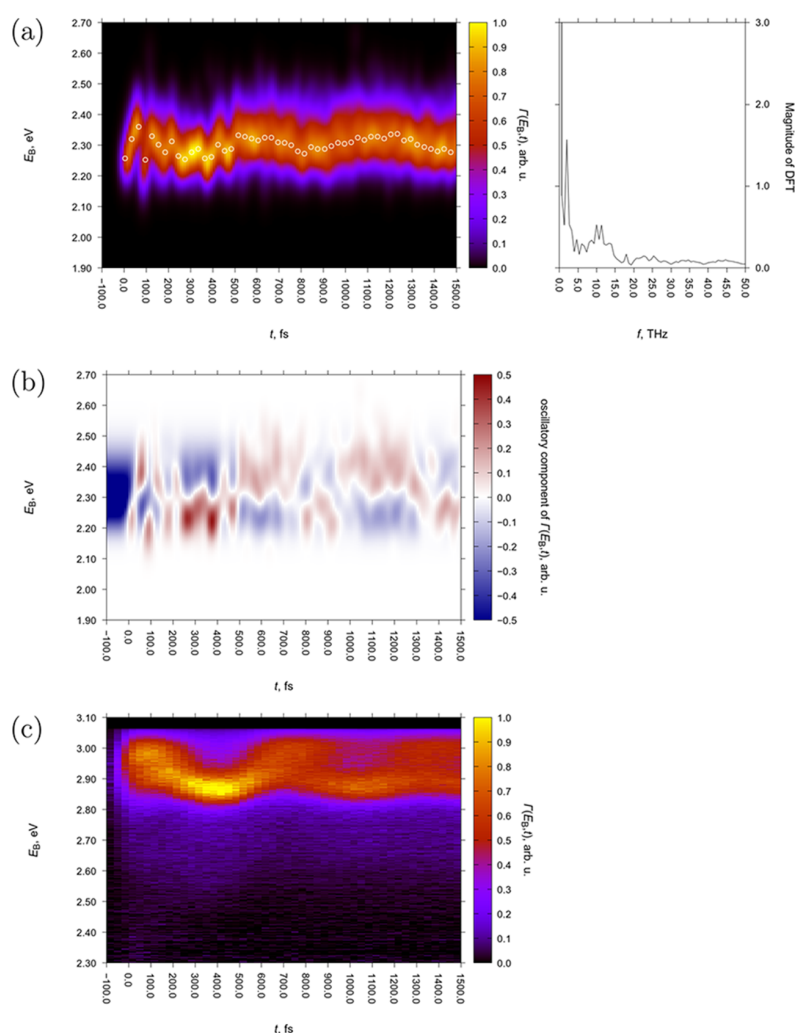


**Figure 8.** (a) Simulated TRPES spectrum of NMM following photoexcitation into the  $S_1$  ( $3s$ ) state. Photoelectron intensity, in arbitrary units, is indicated with the use of color. The white circles indicate the signal maximum. The panel on the right-hand side shows the magnitude of the discrete Fourier transform of the signal maximum. (b) Oscillatory component of simulated TRPES spectrum. (c) Experimentally observed TRPES spectrum of NMM. Adapted with permission from ref 24. Photoelectron intensity, in arbitrary units, is indicated with the use of color. Note that the binding energy axis covers a different range than in (a) and (b).

the median is less sensitive to outliers than the mean). Hence, in subsequent analysis, we will mainly focus on the median.

Oscillations in the mean and median value of  $\Delta$  continue for the remainder of the simulated dynamics. Notably, a slow component of the oscillations, with a period of roughly 500 fs, appears to maintain phase coherence for the entire simulation time. This is especially apparent in the median value of  $\Delta$ .

Accompanying this narrative, as part of the [Supporting Information](#) we provide animations of three representative simulated trajectories. Each animation shows the time evolution of the molecular geometry and the position of the system in the space spanned by the ring puckering coordinates of Hill and Reilly.<sup>52</sup>

During the simulation period of 1.6 ps, there were no instances of simulated trajectories approaching an  $S_1$  ( $3s$ )/ $S_0$  crossing seam, which could potentially mediate internal conversion into the electronic ground state. The energy gap between the  $S_1$  ( $3s$ ) and  $S_0$  states remained above 2.5 eV at all times and along all trajectories. This is consistent with the fact

that NMM photoexcited at 226 nm persists in the  $S_1$  ( $3s$ ) state for at least several picoseconds.<sup>24</sup>

**3.2.2. Time-Resolved Photoelectron Spectrum.** We are now prepared to discuss the simulated TRPES spectrum of NMM, which is plotted in [Figure 8a](#). For comparison, the experimentally observed spectrum of NMM reported in ref 24 is presented in [Figure 8c](#). The observed spectrum takes the form of a single band that spans an energy range of roughly 2.80–3.05 eV. Outside of that range, the photoelectron intensity is nonzero, but negligible.

The simulated spectrum likewise consists of a single band, but it is shifted relative to the observed band by a few tenths of an electronvolt in the direction of lower electron binding energies. Its maximum (indicated with white circles in [Figure 8a](#)) remains in the binding energy range 2.20–2.40 eV. NB in what follows, the term “intensity maximum” will always refer to the position of the photoelectron intensity maximum along the binding energy axis.

On the basis of the benchmark calculations reported in the [Supporting Information](#), we attribute the downward shift of the

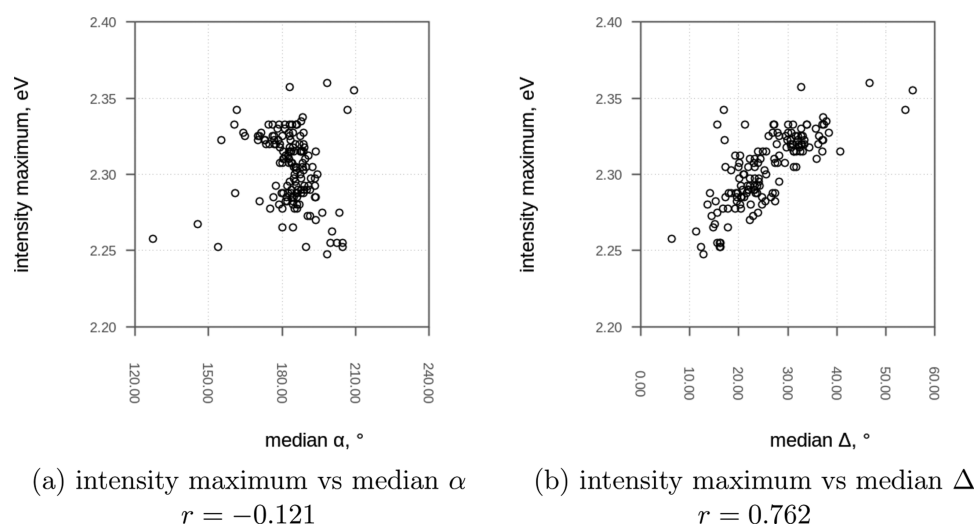


**Figure 9.** Scatter diagrams between (a) intensity maximum and the median value of  $\alpha$  and (b) intensity maximum and the median value of  $\Delta$ . The data points were sampled at intervals of 10 fs over the time period 0–1500 fs.  $r$  denotes the value of the sample Pearson correlation coefficient for a given pair of variables.

band in the simulated spectrum to a systematic error of the ADC(2) method for diffuse excited states, which leads to an underestimation of the electron binding energy associated with the  $S_1(3s) \rightarrow D_0$  ionization process. The possibility can be ruled out that this shift results from a more serious problem, such as, for example, the calculations converging on a wrong electronic state.

Already on visual inspection, it becomes apparent that the simulated TRPES signal exhibits a periodic, oscillatory component with a period of roughly 500 fs, which modulates the intensity maximum. Superimposed on this “slow”, low-frequency oscillation is one or more higher-frequency oscillations with periods of the order of 100 fs.

The periodic, oscillatory nature of the changes in the intensity maximum becomes especially evident if we subtract from the simulated spectrum its time-averaged value. More formally, the oscillatory component of the spectrum was defined as the difference between the spectrum and the average value of the spectrum over the time interval from 0 to 1500 fs:

$$\begin{aligned} & \text{oscillatory component of } \Gamma(E_b, t) \\ &= \Gamma(E_b, t) - \frac{1}{1500 \text{ fs}} \int_0^{1500 \text{ fs}} \Gamma(E_b, t') dt' \end{aligned} \quad (12)$$

The resulting plot of the oscillatory component of the TRPES spectrum is presented in Figure 8b. The low-frequency oscillations of the intensity maximum manifest themselves clearly in the positive and negative regions of the oscillatory component.

In order to unambiguously determine the frequencies of the oscillations in the TRPES spectrum, the intensity maximum in the time interval from 0 to 1500 fs was subjected to the discrete Fourier transform (DFT). As seen from the plot of the DFT in the panel on the right-hand side of Figure 8a, the intensity maximum exhibits a “slow” component at  $2.0 \pm 0.3$  THz (i.e., a period of  $500 \pm 75$  fs). (The uncertainty in the stated frequency value originates from the finite frequency resolution of the DFT.) This “slow” component may be identified with the oscillation with a period of 650 fs seen in the experimentally observed TRPES spectrum.<sup>24</sup> We have no

definite explanation for the fact that the simulations predict a somewhat shorter oscillation period than is seen in experiment. In any case, the difference between the simulated and observed oscillation period is small in relative terms.

Also visible are some “fast” components in the range from 8 to 14 THz (with periods in the range from 70 to 125 fs). No oscillations in this frequency range are seen in the observed TRPES spectrum, possibly because the experimental time resolution was not sufficient.<sup>24</sup>

Finally, we return to the issue of the mechanistic origin of the “slow” component of the oscillations in the simulated spectrum. As already noted in section 3.1.5, static calculations indicate that these oscillations are more likely to result from nuclear motions along the deformation modes of the six-membered ring than along the umbrella mode of the nitrogen atom. In order to verify whether the dynamical calculations support this view, we examined the relationship between the intensity maximum on one hand and the median values of the structural parameters  $\alpha$  and  $\Delta$  on the other. To this end, Figure 9 presents scatter diagrams between these pairs of variables.

As can be seen from Figure 9a, there is no evidence for a statistically significant relationship, linear or otherwise, between the intensity maximum and the median value of  $\alpha$ . This observation is reflected by the value of the sample Pearson correlation coefficient between the signal maximum and the median value of  $\alpha$ , which takes a near-zero value of  $-0.121$ , indicating weak negative correlation.

However, inspection of Figure 9b suggests a linear relationship between the intensity maximum and the median value of  $\Delta$ . Indeed, the sample Pearson correlation coefficient for this pair of variables takes a value of 0.762, which points to a moderately strong positive correlation (high values of the intensity maximum go with high values of  $\Delta$ , and vice versa). The above observations provide further support for our contention that the fine oscillatory structure of the signal of the 3s state is caused by a coherent wavepacket evolving along the ring modes.

In this regard, our findings stand in contrast to those of Zhang et al.,<sup>24</sup> who attributed the fine oscillatory structure of

that signal to a coherent vibrational motion along the nitrogen umbrella inversion coordinate. The main argument for this assignment came from electronic structure calculations at the  $\Delta$ SCF level, according to which the electron binding energy should be highly sensitive to the umbrella inversion angle.<sup>24</sup> However, this latter result is not supported by the wavefunction-based calculations performed in the course of the present study. Presumably, the strong sensitivity of the electron binding energy to the umbrella inversion angle predicted by  $\Delta$ SCF is an artifact of that method. It must be remembered that this latter method is only a heuristic scheme for the calculation of excited states and is not necessarily able to resolve fine details of their potential energy surfaces.

#### 4. CONCLUSIONS

The present study represents a pilot application of dynamical simulations based on the ADC(2) method in the interpretation of the TRPES spectra of aliphatic amines. Taking, as a test case, the compound NMM, the relaxation dynamics was simulated with the use of the BOMD method. The simulated trajectories subsequently formed the basis for the calculation of the TRPES spectrum.

Rewardingly, the simulated spectrum achieves satisfactorily good agreement with experiment, save for a systematic error that causes the photoelectron signal to be shifted toward lower binding energies. The signal of the  $S_1$  ( $3s$ ) state exhibits oscillations along the binding energy axis with a period of  $500 \pm 75$  fs, which can be identified with the oscillations with a period of 650 fs that are seen in the experimentally observed spectrum. Through an analysis of the motions of the nuclei, as well as the gradient difference vector between the initial and final states in the photoionization process, it is determined that the oscillations arise from a coherent wavepacket evolving along the deformation modes of the six-membered ring. The fact that the oscillations emerge in the simulated spectrum indicates that the ADC(2) method provides a realistic description of the relevant excited- and ionized-state potential energy surfaces.

The success of ADC(2) at simulating the relaxation dynamics and resulting TRPES spectrum of NMM cements its position as the electronic structure method of choice for the modeling of large organic systems that are difficult to treat with higher-level techniques.<sup>58–70</sup> Nevertheless, care must be taken to account for the relatively poor quantitative accuracy of ADC(2) for excitation energies and ionization potentials. For the purposes of the present study, this issue is less of a concern, because the TRPES spectrum of NMM excited initially at 226 nm consists of only a single signal, and there is no ambiguity over which photoionization process is responsible. What is more, in the case of photoionization from a Rydberg-type state, the error in the calculated electron binding energy is partially kept in check by a fortuitous error cancellation between the vertical excitation potential and the vertical excitation energy. This issue is discussed at more length in the [Supporting Information](#). In the general case, however, the correspondence between observed and simulated signals may be less obvious, and the predictive power of ADC(2) will hinge on the availability of high-level theoretical benchmarks.

#### ■ ASSOCIATED CONTENT

##### 📄 Supporting Information

The Supporting Information is available free of charge on the ACS Publications website at DOI: [10.1021/acs.jpca.8b10241](https://doi.org/10.1021/acs.jpca.8b10241).

Animations of three representative simulated trajectories in MP4 format ([ZIP](#))

Simulated trajectories in xyz format ([ZIP](#))

Analysis of basis set effects, benchmark coupled-cluster calculations, gradient difference vector structures, molecular structures, and eigenvectors, Lewis structure of morpholine, table of normal modes of morpholine, comments on the definition of parameter  $\Delta$ , discussion of the raw simulated spectrum and the effect of the Gaussian blur, ground-state conformers of NMM, and Cartesian coordinates of ground- and excited-state equilibrium geometries ([PDF](#))

#### ■ AUTHOR INFORMATION

##### Corresponding Author

\*M. A. Kochman. E-mail: [michal.kochman@liu.se](mailto:michal.kochman@liu.se). Phone: +46 701 697 673.

##### ORCID

Michał Andrzej Kochman: [0000-0003-2552-9464](https://orcid.org/0000-0003-2552-9464)

##### Notes

The authors declare no competing financial interest.

#### ■ ACKNOWLEDGMENTS

We are indebted to Prof. Dr Peter M. Weber for interesting and valuable discussion and for having shared with us the experimentally recorded TRPES spectrum of NMM, as well as information on its excited-state lifetime. This work was supported by the Max Planck Society and by the Excellence Cluster, the Hamburg Centre for Ultrafast Imaging (CUI), as well as by the Alexander von Humboldt Foundation. We acknowledge invaluable technical assistance from Dr. Tim Ehlers and Dr. Christian Boehme at the Gesellschaft für wissenschaftliche Datenverarbeitung mbH Göttingen (GWGD).

#### ■ REFERENCES

- (1) Halpern, A. M. The spectroscopy, photophysics and photochemistry of saturated amines. In *Amino, Nitroso and Nitro Compounds and Their Derivatives*; Patai, S., Ed.; Wiley: New York, 1982; pp 155–180.
- (2) Kassab, E.; Evleth, E. M. The Rydberg Photophysics and Photochemistry of Amines In *The Role of Rydberg States in Spectroscopy and Photochemistry: Low and High Rydberg States Sándorfy*; Kluwer Academic Publishers: New York, 1999; pp 231–246.
- (3) Cheng, W.; Kuthirummal, N.; Gosselin, J. L.; Sølling, T. I.; Weinkauff, R.; Weber, P. M. Control of Local Ionization and Charge Transfer in the Bifunctional Molecule 2-Phenylethyl-*N,N*-dimethylamine Using Rydberg Fingerprint Spectroscopy. *J. Phys. Chem. A* **2005**, *109*, 1920–1925.
- (4) Minitti, M. P.; Weber, P. M. Time-Resolved Conformational Dynamics in Hydrocarbon Chains. *Phys. Rev. Lett.* **2007**, *98*, 253004.
- (5) Gosselin, J. L.; Minitti, M. P.; Rudakov, F. M.; Sølling, T. I.; Weber, P. M. Energy Flow and Fragmentation Dynamics of *N,N*-Dimethylisopropylamine. *J. Phys. Chem. A* **2006**, *110*, 4251–4255.
- (6) Minitti, M. P.; Weber, P. M. Time-Resolved Conformational Dynamics in Hydrocarbon Chains. *Phys. Rev. Lett.* **2007**, *98*, 253004.
- (7) Cardoza, J. D.; Weber, P. M. Resolved: Electronic States underneath Broad Absorptions. *J. Chem. Phys.* **2007**, *127*, 036101.
- (8) Cardoza, J. D.; Rudakov, F. M.; Weber, P. M. Electronic Spectroscopy and Ultrafast Energy Relaxation Pathways in the Lowest Rydberg States of Trimethylamine. *J. Phys. Chem. A* **2008**, *112*, 10736–10743.

- (9) Ashfold, M. N. R.; King, G. A.; Murdock, D.; Nix, M. G. D.; Oliver, T. A. A.; Sage, A. G.  $\pi\sigma^*$  Excited States in Molecular Photochemistry. *Phys. Chem. Chem. Phys.* **2010**, *12*, 1218–1238.
- (10) Boguslavskiy, A. E.; et al. Non-Born-Oppenheimer Wavepacket Dynamics in Polyatomic Molecules: Vibrations at Conical Intersections in DABCO. *Faraday Discuss.* **2011**, *150*, 419–438.
- (11) Liang, X.; Levy, M. G.; Deb, S.; Geiser, J. D.; Stratt, R. M.; Weber, P. M. Electron Diffraction with Bound Electrons: The Structure Sensitivity of Rydberg Fingerprint Spectroscopy. *J. Mol. Struct.* **2010**, *978*, 250–256.
- (12) Bush, J. C.; Minitti, M. P.; Weber, P. M. Dissociative Energy Flow, Vibrational Energy Redistribution, and Conformer Structural Dynamics in Bifunctional Amine Model Systems. *J. Phys. Chem. A* **2010**, *114*, 11078–11084.
- (13) Deb, S.; Bayes, B. A.; Minitti, M. P.; Weber, P. M. Structural Dynamics in Floppy Systems: Ultrafast Conformer Motions in Rydberg-Excited Triethylamine. *J. Phys. Chem. A* **2011**, *115*, 1804–1809.
- (14) Mignolet, B.; Gijbbersen, A.; Vrakking, M. J. J.; Levine, R. D.; Remacle, F. Stereocontrol of Attosecond Time-Scale Electron Dynamics in ABCU Using Ultrafast Laser Pulses: a Computational Study. *Phys. Chem. Chem. Phys.* **2011**, *13*, 8331–8344.
- (15) Deb, S.; Cheng, X.; Weber, P. M. Structural Dynamics and Charge Transfer in Electronically Excited  $N,N'$ -Dimethylpiperazine. *J. Phys. Chem. Lett.* **2013**, *4*, 2780–2784.
- (16) Cheng, X.; Zhang, Y.; Deb, S.; Minitti, M. P.; Gao, Y.; Jónsson, H.; Weber, P. M. Ultrafast Structural Dynamics in Rydberg Excited  $N,N,N',N'$ -Tetramethylethylenediamine: Conformation Dependent Electron Lone Pair Interaction and Charge Delocalization. *Chem. Sci.* **2014**, *5*, 4394–4403.
- (17) Gudmundsdóttir, H.; Zhang, Y.; Weber, P. M.; Jónsson, H. Self-Interaction Corrected Density Functional Calculations of Rydberg States of Molecular Clusters:  $N,N$ -Dimethylisopropylamine. *J. Chem. Phys.* **2014**, *141*, 234308.
- (18) Cheng, X.; Zhang, Y.; Gao, Y.; Jónsson, H.; Weber, P. M. Ultrafast Structural Pathway of Charge Transfer in  $N,N,N',N'$ -Tetramethylethylenediamine. *J. Phys. Chem. A* **2015**, *119*, 2813–2818.
- (19) Klein, L. B.; Thompson, J. O. F.; Crane, S. W.; Saalbach, L.; Sølling, T. I.; Paterson, M. J.; Townsend, D. Ultrafast Relaxation Dynamics of Electronically Excited Piperidine: Ionization Signatures of Rydberg/Valence Evolution. *Phys. Chem. Chem. Phys.* **2016**, *18*, 25070–25079.
- (20) Klein, L. B.; Morsing, T. J.; Livingstone, R. A.; Townsend, D.; Sølling, T. I. The Effects of Symmetry and Rigidity on Non-Adiabatic Dynamics in Tertiary Amines: a Time-Resolved Photoelectron Velocity-Map Imaging Study of the Cage-Amine ABCO. *Phys. Chem. Chem. Phys.* **2016**, *18*, 9715–9723.
- (21) Cheng, X.; Gao, Y.; Rudakov, F.; Weber, P. M. Charge Transfer and Ultrafast Nuclear Motions: The Complex Structural Dynamics of an Electronically Excited Triamine. *Chem. Sci.* **2016**, *7*, 619–627.
- (22) Cheng, X.; Zhang, Y.; Jónsson, E.; Jónsson, H.; Weber, P. M. Charge Localization in a Diamine Cation Provides a Test of Energy Functionals and Self-Interaction Correction. *Nat. Commun.* **2016**, *7*, 11013.
- (23) Thompson, J. O. F.; Klein, L. B.; Sølling, T. I.; Paterson, M. J.; Townsend, D. The Role of Novel Rydberg-Valence Behaviour in the Non-Adiabatic Dynamics of Tertiary Aliphatic Amines. *Chem. Sci.* **2016**, *7*, 1826–1839.
- (24) Zhang, Y.; Deb, S.; Jónsson, H.; Weber, P. M. Observation of Structural Wavepacket Motion: The Umbrella Mode in Rydberg-Excited  $N$ -Methyl Morpholine. *J. Phys. Chem. Lett.* **2017**, *8*, 3740–3744.
- (25) Zhang, Y.; Jónsson, H.; Weber, P. M. Coherence in nonradiative transitions: internal conversion in Rydberg-excited  $N$ -methyl and  $N$ -ethyl morpholine. *Phys. Chem. Chem. Phys.* **2017**, *19*, 26403–26411.
- (26) Blanchet, V.; Stolow, A. Nonadiabatic Dynamics in Polyatomic Systems Studied by Femtosecond Time-Resolved Photoelectron Spectroscopy. *J. Chem. Phys.* **1998**, *108*, 4371–4374.
- (27) Blanchet, V.; Zgierski, M. Z.; Seideman, T.; Stolow, A. Discerning Vibronic Molecular Dynamics Using Time-Resolved Photoelectron Spectroscopy. *Nature* **1999**, *401*, 52–54.
- (28) Lochbrunner, S.; Larsen, J. J.; Shaffer, J. P.; Schmitt, M.; Schultz, T.; Underwood, J. G.; Stolow, A. Methods and Applications of Femtosecond Time-Resolved Photoelectron Spectroscopy. *J. Electron Spectrosc. Relat. Phenom.* **2000**, *112*, 183–198.
- (29) Neumark, D. M. Time-Resolved Photoelectron Spectroscopy of Molecules and Clusters. *Annu. Rev. Phys. Chem.* **2001**, *52*, 255–277.
- (30) Stolow, A. Femtosecond Time-Resolved Photoelectron Spectroscopy of Polyatomic Molecules. *Annu. Rev. Phys. Chem.* **2003**, *54*, 89–119.
- (31) Stolow, A.; Bragg, A. E.; Neumark, D. M. Femtosecond Time-Resolved Photoelectron Spectroscopy. *Chem. Rev.* **2004**, *104*, 1719–1757.
- (32) Wu, G.; Hockett, P.; Stolow, A. Time-Resolved Photoelectron Spectroscopy: From Wavepackets to Observables. *Phys. Chem. Chem. Phys.* **2011**, *13*, 18447–18467.
- (33) Gosselin, J. L.; Weber, P. M. Rydberg Fingerprint Spectroscopy: A New Spectroscopic Tool with Local and Global Structural Sensitivity. *J. Phys. Chem. A* **2005**, *109*, 4899–4904.
- (34) Kuthirummal, N.; Weber, P. M. Rydberg States: Sensitive Probes of Molecular Structure. *Chem. Phys. Lett.* **2003**, *378*, 647–653.
- (35) Kuthirummal, N.; Weber, P. M. Structure Sensitive Photoionization via Rydberg Levels. *J. Mol. Struct.* **2006**, *787*, 163–166.
- (36) Gudmundsdóttir, H.; Zhang, Y.; Weber, P. M.; Jónsson, H. Self-Interaction Corrected Density Functional Calculations of Molecular Rydberg States. *J. Chem. Phys.* **2013**, *139*, 194102.
- (37) Perdew, J. P.; Zunger, A. Self-Interaction Correction to Density-Functional Approximations for Many-Electron Systems. *Phys. Rev. B: Condens. Matter Mater. Phys.* **1981**, *23*, 5048–5079.
- (38) Trofimov, A. B.; Schirmer, J. An Efficient Polarization Propagator Approach to Valence Electron Excitation Spectra. *J. Phys. B: At., Mol. Opt. Phys.* **1995**, *28*, 2299–2324.
- (39) Hättig, C. Structure Optimizations for Excited States with Correlated Second-Order Methods: CC2 and ADC(2). In *Adv. Quantum Chem.*; Jensen, H. J. Å., Ed.; Academic Press: New York, 2005; Vol. 50, pp 37–60.
- (40) Neville, S. P.; Averbukh, V.; Patchkovskii, S.; Ruberti, M.; Yun, R.; Chergui, M.; Stolow, A.; Schuurman, M. S. Beyond Structure: Ultrafast X-ray Absorption Spectroscopy as a Probe of Non-adiabatic Wavepacket Dynamics. *Faraday Discuss.* **2016**, *194*, 117–145.
- (41) Kendall, R. A.; Dunning, T. H., Jr.; Harrison, R. J. Electron Affinities of the First-Row Atoms Revisited. Systematic Basis Sets and Wave Functions. *J. Chem. Phys.* **1992**, *96*, 6796–6806.
- (42) Papajak, E.; Zheng, J.; Xu, X.; Leverentz, H. R.; Truhlar, D. G. Perspectives on Basis Sets Beautiful: Seasonal Plantings of Diffuse Basis Functions. *J. Chem. Theory Comput.* **2011**, *7*, 3027–3034.
- (43) Stanton, J. F.; Gauss, J. A Simple Scheme for the Direct Calculation of Ionization Potentials with Coupled-Cluster Theory that Exploits Established Excitation Energy Methods. *J. Chem. Phys.* **1999**, *111*, 8785–8788.
- (44) TURBOMOLE V6.3.1 2011, a development of University of Karlsruhe and Forschungszentrum Karlsruhe GmbH, 1989-2007, TURBOMOLE GmbH, since 2007; available from <http://www.turbomole.com>.
- (45) Haase, F.; Ahlrichs, R. Semi-direct MP2 Gradient Evaluation on Workstation Computers: The MPGRAD Program. *J. Comput. Chem.* **1993**, *14*, 907–912.
- (46) Weigend, F.; Häser, M. RI-MP2: First Derivatives and Global Consistency. *Theor. Chem. Acc.* **1997**, *97*, 331–340.
- (47) Hättig, C.; Weigend, F. CC2 Excitation Energy Calculations on Large Molecules Using the Resolution of the Identity Approximation. *J. Chem. Phys.* **2000**, *113*, 5154–5161.
- (48) Köhn, A.; Hättig, C. Analytic Gradients for Excited States in the Coupled-Cluster Model CC2 Employing the Resolution-of-the-Identity Approximation. *J. Chem. Phys.* **2003**, *119*, 5021–5036.

- (49) Weigend, F.; Köhn, A.; Hättig, C. Efficient Use of the Correlation Consistent Basis Sets in Resolution of the Identity MP2 Calculations. *J. Chem. Phys.* **2002**, *116*, 3175–3183.
- (50) Czako, G.; Kaledin, A. L.; Bowman, J. M. A Practical Method to Avoid Zero-Point Leak in Molecular Dynamics Calculations: Application to the Water Dimer. *J. Chem. Phys.* **2010**, *132*, 164103.
- (51) Martínez-Fernández, L.; Corral, I.; Granucci, G.; Persico, M. Competing Ultrafast Intersystem Crossing and Internal Conversion: A Time Resolved Picture for the Deactivation of 6-Thioguanine. *Chem. Sci.* **2014**, *5*, 1336–1347.
- (52) Hill, A. D.; Reilly, P. J. Puckering Coordinates of Monocyclic Rings by Triangular Decomposition. *J. Chem. Inf. Model.* **2007**, *47*, 1031–1035.
- (53) Arbelo-González, W.; Crespo-Otero, R.; Barbatti, M. Steady and Time-Resolved Photoelectron Spectra Based on Nuclear Ensembles. *J. Chem. Theory Comput.* **2016**, *12*, 5037–5049.
- (54) Barbatti, M.; Granucci, G.; Persico, M.; Ruckebauer, M.; Vazdar, M.; Eckert-Maksić, M.; Lischka, H. The On-the-fly Surface-hopping Program System Newton-X: Application to *Ab Initio* Simulation of the Nonadiabatic Photodynamics of Benchmark Systems. *J. Photochem. Photobiol., A* **2007**, *190*, 228–240.
- (55) Barbatti, M.; Granucci, G.; Ruckebauer, M.; Plasser, F.; Crespo-Otero, R.; Pittner, J.; Persico, M.; Lischka, H. *NEWTON-X: A Package for Newtonian Dynamics Close to the Crossing Seam*, 2013, [www.newtonx.org](http://www.newtonx.org).
- (56) Barbatti, M.; Ruckebauer, M.; Plasser, F.; Pittner, J.; Granucci, G.; Persico, M.; Lischka, H. Newton-X: A Surface-Hopping Program for Nonadiabatic Molecular Dynamics. *WIREs: Comp. Mol. Sci.* **2014**, *4*, 26–33.
- (57) IUPAC-IUB Joint Commission on Biochemical Nomenclature (JCBN).. Conformational Nomenclature for Five and Six-Membered Ring Forms of Monosaccharides and Their Derivatives. *Eur. J. Biochem.* **1980**, *111*, 295–298.
- (58) Plötner, J.; Dreuw, A. Molecular Mechanism of the Z/E-Photoisomerization of Hemithioindigo Hemistilbene. *J. Phys. Chem. A* **2009**, *113*, 11882–11887.
- (59) Plasser, F.; Crespo-Otero, R.; Pederzoli, M.; Pittner, J.; Lischka, H.; Barbatti, M. Surface Hopping Dynamics with Correlated Single-Reference Methods: 9H-Adenine as a Case Study. *J. Chem. Theory Comput.* **2014**, *10*, 1395–1405.
- (60) Barbatti, M. Photorelaxation Induced by Water-Chromophore Electron Transfer. *J. Am. Chem. Soc.* **2014**, *136*, 10246–10249.
- (61) Spata, V. A.; Matsika, S. Role of Excitonic Coupling and Charge-Transfer States in the Absorption and CD Spectra of Adenine-Based Oligonucleotides Investigated through QM/MM Simulations. *J. Phys. Chem. A* **2014**, *118*, 12021–12030.
- (62) Tuna, D.; Sobolewski, A. L.; Domcke, W. Mechanisms of Ultrafast Excited-State Deactivation in Adenosine. *J. Phys. Chem. A* **2014**, *118*, 122–127.
- (63) Prlj, A.; Curchod, B. F. E.; Corminboeuf, C. Excited State Dynamics of Thiophene and Bithiophene: New Insights into Theoretically Challenging Systems. *Phys. Chem. Chem. Phys.* **2015**, *17*, 14719–14730.
- (64) Du, L.; Lan, Z. An On-the-Fly Surface-Hopping Program JADE for Nonadiabatic Molecular Dynamics of Polyatomic Systems: Implementation and Applications. *J. Chem. Theory Comput.* **2015**, *11*, 1360–1374.
- (65) Crespo-Otero, R.; Kungwan, N.; Barbatti, M. Stepwise Double Excited-State Proton Transfer is Not Possible in 7-Azaindole Dimer. *Chem. Sci.* **2015**, *6*, 5762–5767.
- (66) Barbatti, M.; Lischka, H. Why Water Makes 2-Aminopurine Fluorescent? *Phys. Chem. Chem. Phys.* **2015**, *17*, 15452–15459.
- (67) Spata, V. A.; Matsika, S. Photophysical Deactivation Pathways in Adenine Oligonucleotides. *Phys. Chem. Chem. Phys.* **2015**, *17*, 31073–31083.
- (68) Marchetti, B.; Karsili, T. N. V. Theoretical Insights into the Photo-Protective Mechanisms of Natural Biological Sunscreens: Building Blocks of Eumelanin and Pheomelanin. *Phys. Chem. Chem. Phys.* **2016**, *18*, 3644–3658.
- (69) Crespo-Otero, R.; Barbatti, M. Recent Advances and Perspectives on Nonadiabatic Mixed Quantum-Classical Dynamics. *Chem. Rev.* **2018**, *118*, 7026–7068.
- (70) Lischka, H.; Barbatti, M.; Siddique, F.; Das, A.; Aquino, A. J. A. The Effect of Hydrogen Bonding on the Nonadiabatic Dynamics of a Thymine-Water Cluster. *Chem. Phys.* **2018**.

The Supporting Information is available free of charge  
on the ACS Publications website at  
DOI: 10.1021/acs.jpca.8b10241.



# Chapter 3

## Outlook

In this thesis, an MQC scheme implemented with ADC(2) provides now a new platform for treating excited-states for large organic molecules. The accuracy of ADC(2) is assessed by comparison with the results of EOM-CCSD-based calculations for binding energies of electrons from Rydberg orbitals. This investigation focuses on the evaluation of the performance of several different issues that are particularly important for the modeling of photo-processes using ADC(2). These aspects include (1). the accuracy of calculated experimental observables (2). the description of key reaction mode and (3). the description of Rydberg's electronic excited states.

This study will have an impact in the future exploration of using ADC(2) as an accurate descriptor for nuclear dynamics in the Rydberg-electronic states of large molecules.

The MQC scheme has also been implemented and then applied to the study of the excited-state dynamics of photochromic systems. The method is based on the fewest-switches trajectory surface hopping method and uses TDDFT as an underlying electronic structure method. This developed TDDFT-MQC scheme is tested by studying the photo-dynamical isomerization process of SNP. The TDDFT-MQC method agrees in the predicted reaction mechanism as well as concerning the predicted excited-state lifetimes.

This work will provide better insights when it will be applied to condensed phase problems involving molecular crystal photo-chemistry. A hybrid QM/MM approach where the photo excited molecule could be now treated within MQC and the rest of the crystal environment is added via MM methodology.

It remains the hope that improvements in the development of xc-functionals and kernels become available for a more accurate modeling of electronic states of large polyatomic systems. This requires that nuclear gradients from the improved xc-functionals can be obtained "on-the-fly". The MQC method is independent of the approximation used for the xc-functional and can directly profit from any improvement of the xc-functionals that leads to more accurate TDDFT potential energy surfaces.



# Bibliography

- [1] Halina Abramczyk. *Introduction to laser spectroscopy*. Elsevier, 2005.
- [2] RR Alfano and SL Shapiro. Emission in the region 4000 to 7000 Å via four-photon coupling in glass. *Physical Review Letters*, 24(11):584, 1970.
- [3] Yao Zhang, Sanghamitra Deb, Hannes Jansson, and Peter M Weber. Observation of structural wavepacket motion: the umbrella mode in rydberg-excited n-methyl morpholine. *The journal of physical chemistry letters*, 8(16):3740–3744, 2017.
- [4] Narayanan Kuthirummal and Peter M Weber. Rydberg states: sensitive probes of molecular structure. *Chemical physics letters*, 378(5-6):647–653, 2003.
- [5] Domcke Wolfgang, Koppel Horst, et al. *Conical intersections: electronic structure, dynamics & spectroscopy*, volume 15. World Scientific, 2004.
- [6] Edward Teller. The crossing of potential surfaces. *Journal of Physical Chemistry*, 41(1):109–116, 1937.
- [7] W Kauzmann. Quantum chemistry, chaps. 15 and 16, 1957.
- [8] Th Förster. Diabatic and adiabatic processes in photochemistry. *Pure and Applied Chemistry*, 24(3):443–450, 1970.
- [9] G Herzberg and HC Longuet-Higgins. Intersection of potential energy surfaces in polyatomic molecules. *Discussions of the Faraday Society*, 35:77–82, 1963.
- [10] Howard E Zimmerman. Molecular orbital correlation diagrams, mobius systems, and factors controlling ground-and excited-state reactions. ii. *Journal of the American Chemical Society*, 88(7):1566–1567, 1966.
- [11] Josef Michl. Energy barriers in photochemical reactions. case for the relevance of woodward-hoffmann-type correlations. *Journal of the American Chemical Society*, 93(2):523–524, 1971.
- [12] Josef Michl. Physical basis of qualitative mo arguments in organic photochemistry. In *Photochemistry*, pages 1–59. Springer, 1974.
- [13] Fernando Bernardi, Massimo Olivucci, and Michael A Robb. Potential energy surface crossings in organic photochemistry. *Chemical Society Reviews*, 25(5):321–328, 1996.
- [14] M Ben-Nun and Todd J Martinez. Ab initio molecular dynamics study of cis–trans photoisomerization in ethylene. *Chemical physics letters*, 298(1-3):57–65, 1998.
- [15] John C Tully. Mixed quantum–classical dynamics. *Faraday Discussions*, 110:407–419, 1998.

- [16] Marco Garavelli, Fernando Bernardi, Massimo Olivucci, Michael J Bearpark, Stephane Klein, and Michael A Robb. Product distribution in the photolysis of s-cis butadiene: a dynamics simulation. *The Journal of Physical Chemistry A*, 105(51):11496–11504, 2001.
- [17] Raymond Kapral and Giovanni Ciccotti. Mixed quantum-classical dynamics. *The Journal of chemical physics*, 110(18):8919–8929, 1999.
- [18] Steve Nielsen, Raymond Kapral, and Giovanni Ciccotti. Mixed quantum-classical surface hopping dynamics. *The Journal of Chemical Physics*, 112(15):6543–6553, 2000.
- [19] Steve Nielsen, Raymond Kapral, and Giovanni Ciccotti. Statistical mechanics of quantum-classical systems. *The Journal of Chemical Physics*, 115(13):5805–5815, 2001.
- [20] John C Burant and John C Tully. Nonadiabatic dynamics via the classical limit schrödinger equation. *The Journal of Chemical Physics*, 112(14):6097–6103, 2000.
- [21] Oleg V Prezhdo and Craig Brooksby. Quantum backreaction through the bohmian particle. *Physical review letters*, 86(15):3215, 2001.
- [22] Thom Vreven, Fernando Bernardi, Marco Garavelli, Massimo Olivucci, Michael A Robb, and H Bernhard Schlegel. Ab initio photoisomerization dynamics of a simple retinal chromophore model. *Journal of the American Chemical Society*, 119(51):12687–12688, 1997.
- [23] Nikos L Doltsinis and Dominik Marx. Nonadiabatic car-parrinello molecular dynamics. *Physical review letters*, 88(16):166402, 2002.
- [24] Alessandro Ferretti, Giovanni Granucci, Alessandro Lami, Maurizio Persico, and Giovanni Villani. Quantum mechanical and semiclassical dynamics at a conical intersection. *The Journal of chemical physics*, 104(14):5517–5527, 1996.
- [25] Jian-Yun Fang and Sharon Hammes-Schiffer. Improvement of the internal consistency in trajectory surface hopping. *The Journal of Physical Chemistry A*, 103(47):9399–9407, 1999.
- [26] Maria S Topaler, Thomas C Allison, David W Schwenke, and Donald G Truhlar. What is the best semiclassical method for photochemical dynamics of systems with conical intersections? *The Journal of chemical physics*, 109(9):3321–3345, 1998.
- [27] Giovanni Granucci, Maurizio Persico, and Alessandro Toniolo. Direct semiclassical simulation of photochemical processes with semiempirical wave functions. *The Journal of Chemical Physics*, 114(24):10608–10615, 2001.
- [28] Uwe Müller and Gerhard Stock. Consistent treatment of quantum-mechanical and classical degrees of freedom in mixed quantum-classical simulations. *The Journal of chemical physics*, 108(18):7516–7526, 1998.
- [29] Gerhard Stock and Uwe Müller. Flow of zero-point energy and exploration of phase space in classical simulations of quantum relaxation dynamics. *The Journal of chemical physics*, 111(1):65–76, 1999.
- [30] John C Tully. Molecular dynamics with electronic transitions. *The Journal of Chemical Physics*, 93(2):1061–1071, 1990.

- [31] Sharon Hammes-Schiffer and John C Tully. Proton transfer in solution: Molecular dynamics with quantum transitions. *The Journal of chemical physics*, 101(6):4657–4667, 1994.
- [32] DF Coker. Computer simulation methods for nonadiabatic dynamics in condensed systems. In *Computer Simulation in Chemical Physics*, pages 315–377. Springer, 1993.
- [33] Attila Szabo and Neil S Ostlund. *Modern quantum chemistry: introduction to advanced electronic structure theory*. Courier Corporation, 2012.
- [34] Trygve Helgaker, Poul Jorgensen, and Jeppe Olsen. *Molecular electronic-structure theory*. John Wiley & Sons, 2014.
- [35] Ove Christiansen. Coupled cluster theory with emphasis on selected new developments. *Theoretical Chemistry Accounts*, 116(1-3):106–123, 2006.
- [36] Ove Christiansen, Henrik Koch, and Poul Jørgensen. The second-order approximate coupled cluster singles and doubles model cc2. *Chemical Physics Letters*, 243(5-6):409–418, 1995.
- [37] RG Parr and W Yang. *Density-functional theory of atoms and molecules*. clarendon, 1989.
- [38] EKV Gross and RM Dreizler. *Density functional theory: an approach to the quantum many-body problem*, 1990.
- [39] Wolfram Koch and Max C Holthausen. *A chemist’s guide to density functional theory*. John Wiley & Sons, 2015.
- [40] Carlos Fiolhais, Fernando Nogueira, and Miguel AL Marques. *A primer in density functional theory*, volume 620. Springer Science & Business Media, 2003.
- [41] Miguel AL Marques and Eberhard KU Gross. Time-dependent density functional theory. *Annu. Rev. Phys. Chem.*, 55:427–455, 2004.
- [42] Miguel AL Marques, Carsten A Ullrich, Fernando Nogueira, Kieron Burke, Angel Rubio, and Eberhard KU Gross. *Time-dependent density functional theory*, volume 706. Springer Science & Business Media, 2006.
- [43] Andreas Dreuw and Martin Head-Gordon. Single-reference ab initio methods for the calculation of excited states of large molecules. *Chemical reviews*, 105(11):4009–4037, 2005.
- [44] Erich Runge and Eberhard KU Gross. Density-functional theory for time-dependent systems. *Physical Review Letters*, 52(12):997, 1984.
- [45] Robert van Leeuwen. Mapping from densities to potentials in time-dependent density-functional theory. *Physical review letters*, 82(19):3863, 1999.
- [46] Mark E Casida. Time-dependent density functional response theory for molecules. In *Recent Advances In Density Functional Methods: (Part I)*, pages 155–192. World Scientific, 1995.
- [47] M Cassida. Recent advances in density functional methods: time dependent density functional response theory for molecules. *DP Chong, Singapore*, 1995.

- [48] Mark E Casida and Miquel Huix-Rotllant. Progress in time-dependent density-functional theory. *Annual review of physical chemistry*, 63:287–323, 2012.
- [49] Philip J Wilson, Thomas J Bradley, and David J Tozer. Hybrid exchange-correlation functional determined from thermochemical data and ab initio potentials. *The Journal of Chemical Physics*, 115(20):9233–9242, 2001.
- [50] Zheng-Li Cai, Karina Sendt, and Jeffrey R Reimers. Failure of density-functional theory and time-dependent density-functional theory for large extended  $\pi$  systems. *The Journal of chemical physics*, 117(12):5543–5549, 2002.
- [51] David J Tozer and Nicholas C Handy. Improving virtual kohn–sham orbitals and eigenvalues: Application to excitation energies and static polarizabilities. *The Journal of chemical physics*, 109(23):10180–10189, 1998.
- [52] Rüdiger Bauernschmitt and Reinhart Ahlrichs. Treatment of electronic excitations within the adiabatic approximation of time dependent density functional theory. *Chemical Physics Letters*, 256(4-5):454–464, 1996.
- [53] David J Tozer, Roger D Amos, Nicholas C Handy, Bjorn O Roos, and Luis Serrano-Andrés. Does density functional theory contribute to the understanding of excited states of unsaturated organic compounds? *Molecular physics*, 97(7):859–868, 1999.
- [54] Andreas Dreuw, Jennifer L Weisman, and Martin Head-Gordon. Long-range charge-transfer excited states in time-dependent density functional theory require non-local exchange. *The Journal of chemical physics*, 119(6):2943–2946, 2003.
- [55] Yoshihiro Tawada, Takao Tsuneda, Susumu Yanagisawa, Takeshi Yanai, and Kimihiko Hirao. A long-range-corrected time-dependent density functional theory. *The Journal of chemical physics*, 120(18):8425–8433, 2004.
- [56] Rika Kobayashi and Roger D Amos. The application of cam-b3lyp to the charge-transfer band problem of the zincbacteriochlorin–bacteriochlorin complex. *Chemical physics letters*, 420(1-3):106–109, 2006.
- [57] John F Stanton and Rodney J Bartlett. The equation of motion coupled-cluster method. a systematic biorthogonal approach to molecular excitation energies, transition probabilities, and excited state properties. *The Journal of chemical physics*, 98(9):7029–7039, 1993.
- [58] Dniel Knnr, Attila Tajti, and Pter G Szalay. Accuracy of coupled cluster excitation energies in diffuse basis sets. *Journal of chemical theory and computation*, 13(1):202–209, 2016.
- [59] AB Trofimov, G Stelter, and J Schirmer. Electron excitation energies using a consistent third-order propagator approach: Comparison with full configuration interaction and coupled cluster results. *The Journal of chemical physics*, 117(14):6402–6410, 2002.
- [60] AB Trofimov, G Stelter, and J Schirmer. A consistent third-order propagator method for electronic excitation. *The Journal of Chemical Physics*, 111(22):9982–9999, 1999.

- [61] Jochen Schirmer. Beyond the random-phase approximation: A new approximation scheme for the polarization propagator. *Physical Review A*, 26(5):2395, 1982.
- [62] AB Trofimov and J Schirmer. An efficient polarization propagator approach to valence electron excitation spectra. *Journal of Physics B: Atomic, Molecular and Optical Physics*, 28(12):2299, 1995.
- [63] AB Trofimov, IL Krivdina, J Weller, and J Schirmer. Algebraic-diagrammatic construction propagator approach to molecular response properties. *Chemical physics*, 329(1-3):1–10, 2006.
- [64] Christof Hättig. Structure optimizations for excited states with correlated second-order methods: Cc2 and adc (2). *Advances in quantum chemistry*, 50:37–60, 2005.
- [65] Yihan Shao, Laszlo Fusti Molnar, Yousung Jung, Jörg Kussmann, Christian Ochsenfeld, Shawn T Brown, Andrew TB Gilbert, Lyudmila V Slipchenko, Sergey V Levchenko, Darragh P O'Neill, et al. Advances in methods and algorithms in a modern quantum chemistry program package. *Physical Chemistry Chemical Physics*, 8(27):3172–3191, 2006.
- [66] Anna I Krylov and Peter MW Gill. Q-chem: an engine for innovation. *Wiley Interdisciplinary Reviews: Computational Molecular Science*, 3(3):317–326, 2013.
- [67] Justin M Turney, Andrew C Simmonett, Robert M Parrish, Edward G Hohenstein, Francesco A Evangelista, Justin T Fermann, Benjamin J Mintz, Lori A Burns, Jeremiah J Wilke, Micah L Abrams, et al. Psi4: an open-source ab initio electronic structure program. *Wiley Interdisciplinary Reviews: Computational Molecular Science*, 2(4):556–565, 2012.
- [68] Alexander L Fetter and John Dirk Walecka. *Quantum theory of many-particle systems*. Courier Corporation, 2012.
- [69] Andreas Dreuw and Michael Wormit. The algebraic diagrammatic construction scheme for the polarization propagator for the calculation of excited states. *Wiley Interdisciplinary Reviews: Computational Molecular Science*, 5(1):82–95, 2015.
- [70] Ove Christiansen, Poul Jørgensen, and Christof Hättig. Response functions from fourier component variational perturbation theory applied to a time-averaged quasienergy. *International journal of quantum chemistry*, 68(1):1–52, 1998.
- [71] J Schirmer and F Mertins. Size consistency of an algebraic propagator approach. *International journal of quantum chemistry*, 58(4):329–339, 1996.
- [72] Mario R Silva-Junior, Marko Schreiber, Stephan PA Sauer, and Walter Thiel. Benchmarks for electronically excited states: Time-dependent density functional theory and density functional theory based multireference configuration interaction. *The Journal of chemical physics*, 129(10):104103, 2008.
- [73] Marko Schreiber, Mario R Silva-Junior, Stephan PA Sauer, and Walter Thiel. Benchmarks for electronically excited states: Caspt2, cc2, ccsd, and cc3. *The Journal of chemical physics*, 128(13):134110, 2008.

- [74] Jan Hendrik Starcke, Michael Wormit, Jochen Schirmer, and Andreas Dreuw. How much double excitation character do the lowest excited states of linear polyenes have? *Chemical physics*, 329(1-3):39–49, 2006.
- [75] M.G.U.J Petersilka, U.J Gossmann, and E.K.U Gross. Excitation energies from time-dependent density-functional theory. *Physical review letters*, 76(8):1212, 1996.
- [76] Y Kalisky, TE Orłowski, and DJ Williams. Dynamics of the spiropyran-merocyanine conversion in solution. *The Journal of Physical Chemistry*, 87(26):5333–5338, 1983.
- [77] Matteo Rini, Ann-Kathrin Holm, Erik TJ Nibbering, and Henk Fidler. Ultrafast uv-mid-ir investigation of the ring opening reaction of a photochromic spiropyran. *Journal of the American Chemical Society*, 125(10):3028–3034, 2003.
- [78] Brian Stankus, Haiwang Yong, Nikola Zotev, Jennifer M Ruddock, Darren Bellshaw, Thomas J Lane, Mengning Liang, Sébastien Boutet, Sergio Carbajo, Joseph S Robinson, et al. Ultrafast x-ray scattering reveals vibrational coherence following rydberg excitation. *Nature chemistry*, page 1, 2019.